EUSKAL HERRIKO UNIBERSITEA - UNIVERSIDAD DEL PAIS VASCO

MATERIALEN FÍSIKA SAILA - DEPARTAMENTO DE FÍSICA DE MATERIALES

Enhancing resolution, efficiency, and understanding in IR and THz near-field microscopy

PhD thesis

in Physics of Nanostructures and Advanced Materials

submitted by

Stefan Mastel

2018

Enhancing resolution, efficiency, and understanding in IR and THz near-field microscopy

This PhD thesis has been carried out by Stefan Mastel

at

CIC nanoGUNE, San Sebastián, Spain

under the supervision of

Prof. Dr. Rainer Hillenbrand

Contents

1 Resumen

La microscopia y espectroscopia clásicas son técnicas de caracterización fundamentales en ciencia y tecnología en áreas diversas como la biología, la química, la electrónica y la ciencia de materiales [1–4]. En concreto, los métodos espectroscópicos a frecuencias correspondientes a la radiación infrarroja (IR, longitudes de onda $\lambda \approx 3 - 30\ \mu m$) y de terahercios (THz, $\lambda \approx 30 - 300\ \mu m$) se utilizan para el análisis de la absorción en moléculas, de vibraciones de redes cristalinas o de fenómenos de conducción, con las que puede extraerse información relativa a composición química, y propiedades estructurales o electrónicas [1, 5–8]. Sin embargo, en los instrumentos ópticos convencionales debido a la difracción de la luz, la resolución espacial está limitada a longitudes similares a la longitud de onda incidente [2, 9–11]. Por tanto, para la radiación IR la resolución se limita a unas decenas de micras y para la región del THz a unos cientos de micras. Este límite en la resolución impide la investigación detallada de nuevos materiales, compuestos y dispositivos cuya estructura y organización está en el rango de los nanómetros [12–14]. Por este motivo, existe una gran demanda de nuevas herramientas espectroscópicas en el rango IR y de THz con resolución nanométrica tanto en investigación, industria e incluso en el control de calidad. [15–21].

Una técnica de microscopia óptica bien establecida que permite superar el límite de difracción es el microscopio óptico de barrido de campo cercano de tipo dispersivo, s-SNOM (del inglés scattering type scanning optical near field microscopy) [22–24], cuya resolución nanométrica es independiente de la longitud de onda tanto en el rango del visible [11, 22, 25–28], del IR [27, 29–32] como en la región del THz [33–38]. En el s-SNOM una onda continua de un haz de láser es focalizado en una punta de metálica de un microscopio de fuerza atómica (AFM). La punta o tip actúa como una antena y concentra la iluminación en el extremo de la punta en un foco de tamaño similar al diámetro del extremo de la punta, normalmente alrededor de los 20nm [39, 40]. Por otro lado, cuando el tip se coloca muy cerca o en contacto con la muestra, se

produce una fuerte interacción óptica de campo cercano que modifica la luz dispersada, gracias a lo cual, se pueden estudiar las propiedades dieléctricas locales con resolución nanométrica [41, 42]. Al escanear la muestra por debajo de la punta y detectar la radiación dispersa por la punta en función de la posición de la muestra, se pueden grabar imágenes ópticas resueltas a nanoescala. Alternativamente, un láser de banda ancha puede utilizarse como fuente de luz iluminadora para realizar espectroscopia infrarroja por transformada de Fourier (nano-FTIR) con resolución a nanoescala para registrar espectros IR en una posición fija de la muestra con una resolución de aproximadamente 20 nm [41, 42]. Los ejemplos de imágenes de s-SNOM y la espectroscopía nano-FTIR incluyen la identificación infrarroja a nanoescala de la materia orgánica [31, 42–50], la visualización en el espacio real de las resonancias del plasmón en nanoestructuras metálicas [51–58], la propagación de la polariton del plasmón y el fonón en materiales 2D [59–65], o el mapeo de propriedades electronicos en semiconductores [37, 66–72].

Aunque la espectroscopia s-SNOM y nano-FTIR son técnicas bien establecidas y fiables para la caracterización nanométrica de muestras y dispositivos en el IR y THz, las posibles mejoras con respecto a la resolución espacial, la sensibilidad, así como la interpretación de los espectros de campo cercano medidos y los contrastes de materiales son todavía un terreno en gran medida inexplorado. Todas estas propiedades dependen en gran medida de la interacción punta-muestra del campo cercano, que se determina por el material y la geometría tanto de la punta como de la muestra misma. Por lo tanto, una investigación exhaustiva de la influencia de la punta y la muestra en la resolución, sensibilidad y contraste espectral es clave para mejorar estas propiedades, que se inició notablemente con la aplicación de sondas de antena resonante en el rango espectral de infrarrojos [73]. En esta tesis, varios aspectos de s-SNOM y nano-FTIR -desde mejoras técnicas como la resolución y la eficiencia hasta una comprensión e interpretación fundamental de los datos medidos- han mejorado significativamente. Para lograr este objetivo, se diseñaron nuevas sondas de campo cercano para s-SNOM, en contraste con las ménsulas AFM comerciales típicas, y se utilizaron muestras de prueba bien definidas para estudiar y mejorar significativamente la resolución, la eficiencia y el contraste espectral.

Esta tesis presenta la siguiente estructura:

En el capítulo 3 introducimos las tecnicas espectroscópicas de s-SNOM (mi-

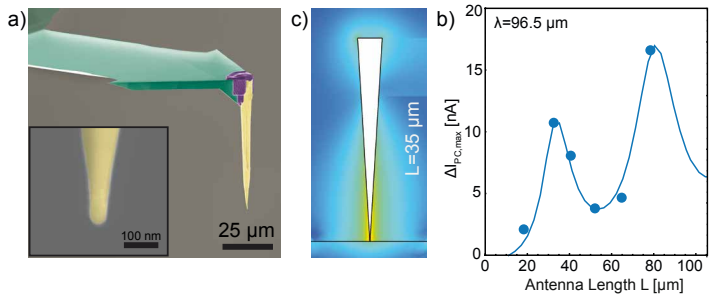

Figure 1.1: **Puntas de antena de resonancia THz en voladizo.** a) Imagen SEM de color falso de una punta de antena THz, fabricada con FIB que muestra Si voladizo (verde), Pt depositado FIB (púrpura) y la punta de antena Pt/Ir (amarillo). b) Cálculo numérico de la distribución eléctrica de campo cercano (logaritmo de la mejora del campo eléctrico) de una punta larga de L = 35 μm, que muestra la primera resonancia fundamental de la antena. c) Medida de la mejora de campo en el vértice de la punta para diferentes longitudes de antena (puntos azules) en comparación con la simulación numérica de la mejora de la intensidad de campo cercano en la punta de la punta (línea azul continua). Los ejes verticales de la simulación numérica se ajustaron manualmente de modo que se obtuviera la mejor concordancia con los puntos de datos experimentales.

croscopía óptica de barrido de campo cercano de tipo dispersivo) y nano-FTIR (nano-espectroscopía de infrarrojos por transformada de fourier), así como los modelos teóricos que describen los contrastes ópticos medidos entre materiales.

En el capítulo 4 mostramos que personalizando las sondas de campo cercano de s-SNOM para el rango de los terahercios se puede conseguir un aumento significativo de la señal con respecto a las sondas estándar y comerciales [74]. Este mejor rendimiento de las sondas de campo cercano es conseguido mecanizando las puntas utilizando un haz de electrones focalizado (FIB) para que su longitud sea del orden de la longitud de onda en el rango de los terahercios (ver Fig. 1.1a), mucho mayor que la longitud de las sondas comerciales (alrededor de 10 μm). La longitud de las puntas es ajustada para que soporte resonancias en los terahercios, lo que mostramos en el cálculo del campo eléctrico para una punta de longitud L = 35 μm mostrado en la Fig. 1.1b. Las resonancias excitadas en la punta aumentan el campo eléctrico en su ápice hasta un

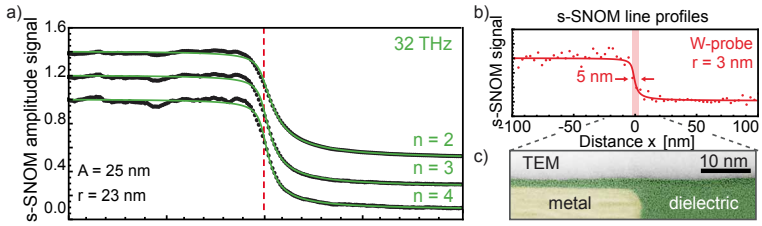

Figure 1.2: **Mediciones de s-SNOM en la muestra de prueba de resolución.** Perfiles de línea de señal de amplitud de IR s-SNOM medidos (promedio de 20 perfiles de línea, normalizados a la señal de amplitud en el metal para armónicos n = 2 a 4 (puntos negros), y sus respectivos ajustes utilizando la integral de un Lorentzian asimétrico (líneas verdes). Amplitud de toma A = 25 nm, radio de punta r = 23 nm. Las curvas están desplazadas verticalmente para una mejor visibilidad. b) El perfil de la línea de amplitud de IR s-SNOM se registró con la punta de W, ultra-aguda (r = 3 nm) fabricada con FIB y su ajuste respectivo, lo que resulta en una resolución de 5 nm. c) Imagen de microscopía electrónica de transmisión de barrido (STEM) de una sección transversal de la muestra de prueba de resolución, que consiste en el borde de una estructura de escudo magnético en una cabeza de lectura / escritura de un disco duro.

factor 9 (see Fig. 1.1c), lo que es confirmado detectando directamente la intensidad del campo cercano utilizando un sensor de campo cercano basado en grafeno, y corroborado por simulaciones numéricas. Estas sondas de campo cercano para THz son prometedoras para futuras aplicaciones en microscopía de campo cercano en los THz, y particularmente, para experimentos de espectroscopía s-SNOM en los THz en el dominio temporal (THz-TDS), donde las señales habitualmente son débiles.

En el capítulo 5, proporcionamos una comprensión cuantitativamente precisa de la formación del contraste de imagen en los bordes de material, por consiguiente, de la resolución espacial en s-SNOM; un terreno sorprendentemente poco explorado [75]. Aquí presentamos la cabeza de lectura/escritura de un disco duro comercial (HDD) como una muestra de testeo muy adecuada para estudios fundamentales, debido a sus agudos y bien definidos bordes de material perpendiculares a su superficie ultra-lisa, tal y como se puede ver en la imagen de microscopía de electrones de transmisión y barrido (STEM)

de la 1.2c. Obtenemos conocimientos sin precedentes e inesperados sobre el proceso de formación de imágenes s-SNOM, libre de contrastes inducidos por la topografía que muchas veces enmascaran y modifican artificialmente el contraste puro de campo cercano. A lo largo de bordes de materiales metálicos y dieléctricos observamos perfiles de línea no simétricos de punta (non-point-symmetric) tanto para la iluminación infrarroja (como se muestra en la Fig. 1.2a) como para la iluminación de THz. Estos perfiles se corroboran completamente por simulaciones numéricas. Explicamos nuestros hallazgos mediante un confinamiento y apantallamiento del campo cercano en el ápice de la punta que son dependientes de la muestra. Esto será de crucial importancia para una precisa comprensión y una interpretación correcta de imágenes s-SNOM de alta resolución en nanomateriales compuestos. Como muestra la Fig. 1.2b también demostramos que con puntas ultra-afiladas de tungsteno la anchura aparente de bordes agudos de material se puede reducir a 5 nm.

En el capítulo 6, estudiamos sistemáticamente la dependencia de espectros nano-FTIR en el espesor de capas poliméricas finas, y proporcionamos pautas para la comparación directa con espectros FTIR de campo lejano estándares [48]. En particular, el comportamiento espectral de la fase (comparar Fig. 1.3a) y la absorción de campo cercano (comparar Fig. 1.3b) ha sido estudiado. Ambas cifras están relacionadas con la presencia de una resonancia molecular. Se ha demostrado que los espectros de la fase del campo cercano dependen poco del espesor de la capa y pueden ser utilizados para una comparación aproximada con espectros de FTIR de incidencia rasante (GI-FTIR, ver la curva roja, Fig. 1.3c). Esto se puede ver comparando la posición del pico de espectros de fase de campo cercano de la Fig. 1.3a con los espectros GI-FTIR en 1.3c. Al contrario, los espectros de absorción de campo cercano (Fig. 1.3b) se pueden comparar con más precisión con espectros de campo lejano para capas ultra-finas se parecen mucho a espectros GI-FTIR, mientras que para espesores gruesos se observa un gran parecido con espectros FTIR estándares de transmisión (curva negra, Fig. 1.3c) is found. Nuestros resultados están basados en datos experimentales obtenidos mediante nano-espectroscopía FTIR (nano-FTIR) y están respaldados por un análisis teórico amplio para proporcionar una comprensión exhaustiva de la correlación entre espectros de campo cercano y campo lejano.

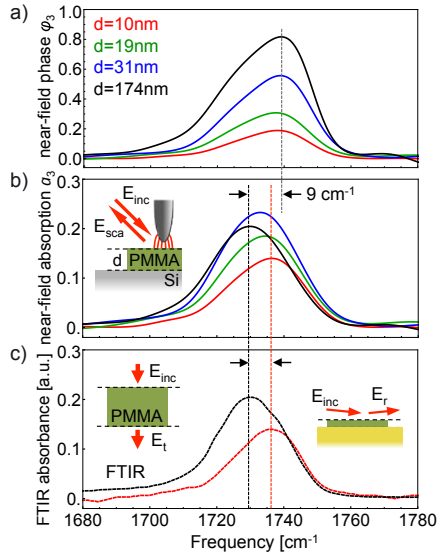

Figure 1.3: **Espectros experimentales de PMMA.** a) Espectros de nano-FTIR de fase y c) de absorción de películas de PMMA (promedios de 40 interferogramas, 53 min tiempo de adquisición por espectro, 7 cm^{-1} resolución). (d) FTIR espectro de PMMA de 1 μm de espesor encinma de CaF_2 y GI-FTIR espectro de PMMA de 10 nm de espesor encima de Au. Las líneas verticales negras y rojas marcan las posiciones máximas..

2 Summary

Classical microscopy and spectroscopy are key characterization techniques in science and technology, including biology, chemistry, electronics, and material sciences [1–4]. Particularly at infrared (IR, wavelength $\lambda \approx 3 - 30\ \mu m$) and Terahertz (THz, $\lambda \approx 30 - 300\ \mu m$) frequencies, spectroscopy methods can be applied to analyze molecular absorption, lattice crystal vibrations, and electric conduction phenomena, from which information about chemical, structural, and electronic material properties can be obtained [1, 5–8]. The spatial resolution in microscopy and spectroscopy, however, is limited by diffraction to length scales in the order of the wavelength [2, 9–11], which is in the range of few to hundreds of micrometers for IR and THz radiation. The resolution limit thus prevents detailed investigation of modern materials, compounds, and devices, where structure, domain, and devices sizes are often on the nanometer scale [12–14]. For that reason, novel IR and THz spectroscopy tools and methods providing nanoscale spatial resolution are highly demanded in research, industrial development, and even quality control [15–21].

A well-established optical microscopy technique to circumvent the diffraction limit is scattering-type Scanning Near-Field Optical Microscopy (s-SNOM) [22–24], reaching wavelength-independent, nanoscale resolution in the visible [11, 22, 25–28], the IR [27, 29–32] and the THz spectral region [33–38]. In s-SNOM, a focused continuous wave (CW) laser beam illuminates the metal tip of an atomic force microscope (AFM). The tip acts as an antenna and concentrates the illumination at its apex to a spot on length scales of the apex radius, typically around 20 nm [39, 40]. In close proximity to a sample, this nano-focus interacts with the sample, which modifies the tip-scattered field, depending on the local optical properties of the sample. As this modification of the tip-scattering is localized to the area right below the tip, optical information with nanoscale spatial resolution can be recorded by detecting the tip-scattered field in the far-field region. By raster-scanning the sample below the tip and detecting the tip-scattered radiation as a function of sample

position, nanoscale resolved optical images can be recorded. Alternatively, a broadband laser can be employed as illuminating light source to perform nanoscale-resolved Fourier Transform Infrared (nano-FTIR) spectroscopy and record IR spectra at a fixed sample position with a resolution of about 20 nm [41, 42]. Examples of s-SNOM imaging and nano-FTIR spectroscopy include the infrared nanoscale identification of organic matter [31, 42–50], the real-space visualization of plasmon resonances in metal nano-structures [51–58], the plasmon and phonon polariton propagation in 2D-materials [59–65], or the mapping of electronic properties in semiconductors [37, 66–72].

Even though s-SNOM and nano-FTIR spectroscopy are well-established and reliable techniques for the optical nanoscale IR and THz characterization of samples and devices, the possible improvements regarding spatial resolution and sensitivity, as well as the understanding of spectral and material contrasts, are still largely unexplored terrain. All of these parameters - resolution, sensitivity, material and spectral contrast - highly depend on the tip-sample near-field interaction, which is determined by material and geometry of both tip and sample itself. Hence, a thorough understanding of the influence of tip and sample on resolution, sensitivity, and spectral and material contrasts is key to develop technical advancements in s-SNOM. In this thesis, well-defined s-SNOM test samples are used to investigate the image formation across material boundaries, as well as the spectral contrast in nano-FTIR spectroscopy. Further, by employing novel, custom-made s-SNOM near-field probes, the resolution and THz sensitivity are significantly improved, which is shown by performing s-SNOM experiments on well-defined test samples and utilizing a novel, graphene-based near-field detector.

This thesis is structured as follows:

Chapter 3 presents a brief introduction to s-SNOM and nano-FTIR spectroscopy techniques, as well as theoretical models to describe experimentally observed material contrasts.

Chapter 4 shows that through a custom-design of THz near-field probes for s-SNOM, a significant signal improvement can be achieved compared to previous experiments employing standard, commercial tips [74]. The enhanced performance of the near-field probes is accomplished by using focused ion beam (FIB) machining to customize the length of the tips to length scales of the Terahertz wavelength (around 100 μm), such that these tips are much

longer than typically employed commercial tips (around 10 μm). The length adjustment of the tips enables the excitation of THz antenna resonances in the tips, which enhances the near-field at the tip apex by up to a factor of 9. This near-field enhancement is confirmed by directly detecting the near-field intensity at the tip apex employing a graphene-based near-field detector, and corroborated by numerical simulations. The presented THz near-field probes promise interesting THz s-SNOM application with enhanced sensitivity, which could be of particular interest for s-SNOM THz time domain spectroscopy (THz-TDS) experiments, where the signals typically are weak.

In Chapter 5, the s-SNOM image contrast formation at material boundaries is studied, as well as the spatial resolution, which is a surprisingly unexplored terrain [75]. To that end, we introduce the read/write head of a commercial hard disk drive (HDD) as a most suitable test sample, given its well-defined sharp material boundaries perpendicular to its ultra-smooth surface. We obtain unprecedented and unexpected insights into the s-SNOM image formation process, free of topography-induced contrasts that often mask and artificially modify the pure near-field optical contrast. Across the metal-dielectric boundary, we observe non-point-symmetric line profiles for both IR and THz illumination, which are fully corroborated by numerical simulations. We explain our findings by a sample-dependent confinement and screening of the near fields at the tip apex, which will be of crucial importance for an accurate understanding and proper interpretation of high-resolution s-SNOM images of nano-composite materials. We further demonstrate that with ultra-sharp tungsten tips the apparent width (resolution) of sharp material boundaries can be reduced to about 5 nm.

In Chapter 6, we systematically study the thickness-dependence of nano-FTIR spectra of thin polymer films, and provide guidelines for their comparison to standard far-field FTIR spectra [48]. Particularly, the spectral behavior of near-field phase and near-field absorption is studied, both quantities signifying the presence of a molecular resonance. It is demonstrated that the near-field phase spectra only weakly depend on the film thickness and can be used for an approximate comparison with grazing incidence FTIR (GI-FTIR) spectra. In contrast, the near-field absorption spectra can be compared more precisely with far-field spectra: for ultra-thin films they match well GI-FTIR spectra, while for thick films a good agreement with standard transmission

FTIR spectra is found. Our results are based on experimental data obtained by nanoscale FTIR (nano-FTIR) spectroscopy and supported by a comprehensive theoretical analysis to provide a thorough understanding of the correlation between near- and far-field FTIR spectra.

3 Scattering-type near-field optical microscopy (s-SNOM)

Scattering-type Scanning Near-field Optical Microscopy (s-SNOM) achieves nanoscale spatial resolution at visible to THz frequencies by scanning a sharp tip over a sample surface and detecting the tip-scattered light as a function of tip position [11, 24]. Among many applications, it enables infrared nanoscale identification of organic matter [42, 44–48], the real-space visualization of plasmon resonances in metal nano-structures [51–57], the plasmon and phonon polariton propagation in 2D-materials [59–65], or the mapping of electronics properties in semiconductors [37, 69–72]. This chapter introduces the basic concepts of s-SNOM, its different operation modes such as imaging and spectroscopy, as well as theoretical models.

3.1 Resolution limit in classical microscopy

Since the establishment of conventional light microscopy in the 17th century, it has shown a vast variety of applications in science and technology. It is based on mirrors and lenses for guiding and focusing of propagating electromagnetic waves to form an image of the object under investigation [2]. However, due to its wave nature, light is diffracted when passing through apertures and lenses, which inherently limits the spatial resolution of the technique.

The resolution limit of an optical microscope was already formulated by Lord Rayleigh [10] and E. Abbe [9], and is given by

$$x_{min} = 0.61\frac{\lambda}{n\ \sin\ \xi} = 0.61\frac{\lambda}{N_A}, \tag{3.1}$$

where x_{min} is the minimum distance at which two point like objects can be resolved, λ is the imaging wavelength, n the index of refraction of the medium between lens and object, and ξ the half-angle of the light cone detected by

the objective. $N_A = n \sin \xi$ is called the numerical aperture of the objective. According to the formulation of the resolution criterion in eq. (3.1), the resolution is increased for decreasing values of x_{min}. As a consequence, the highest achievable resolution (i.e. the smallest x_{min}) in air ($n = 1 \Rightarrow N_A \leq 1$) of an optical light microscope is approximately $\lambda/2$. The resolution can be increased by increasing the numerical aperture N_A, which can be achieved by filling the space between microscope objective and sample with an immersion liquid, e.g., water (n=1.33), glycerin (n=1.47), or oil (n=1.51). As the refractive index of such an immersion liquid is larger than 1, the N_A is increased compared to air, and hence the spatial resolution. However, even with the aid of an immersion liquid, the resolution is limited to length scales on the order of 200 nm in the visible spectral range ($\lambda \approx 400 - 700\ nm$), but significantly worsens for longer wavelength in the mid-infrared ($\lambda \approx 3 - 30\ \mu$m) or the terahertz (THz or far-infrared, $\lambda \approx 30 - 300\ \mu$m) spectral range.

Besides the numerical aperture N_A, the wavelength λ is a fundamentally limiting factor of the resolution. The resolution can be increased by using light of a shorter wavelength λ (see eq. (3.1)), e.g., ultra-violet (UV) radiation ($\lambda = 10 - 400$ nm) or x-rays ($\lambda = 0.01 - 10$ nm). However, the high energy photons at such short wavelengths can damage in particular organic and biological materials. Besides using short wavelengths, other approaches exist to further increase the spatial resolution, such as STORM [76, 77] (Stochastical Optical Reconstruction Microscopy) and PALM [78] (Photo Activated Localization Microscopy), which employ statistical methods on fluorescent samples. Typically, a resolution of only a few nanometers can be achieved [79]. About the same resolution [80] can be achieved by STED (Stimulated Emission Depletion) [81] microscopy. STED selectively depletes fluorescent states of labelled molecules with a laser beam engineered such that a center spot of the illuminated area remains fluorescent active [82]. Therefore, fluorescent molecules in the center region can be detected. By choosing the beam profile such that the center spot is much smaller than the wavelength, sub-diffraction resolution is possible.

A non-optical technique to increase the resolution compared to classical light microscopy is electron microscopy, which exploits the much shorter wavelength of electrons compared to electromagnetic waves in the visible spectral range. Examples are Scanning Electron Microscopy (SEM) and Transmission Electron Microscopy (TEM), where an electron beam scans the sample surface to create

an image with spatial resolution down to *Ångstroms* length scales [83, 84].

Another highly versatile microscopy technique that can achieve nanoscale resolution is Scanning Probe Microscopy (SPM), which is introduced in detail in the following Section 3.2.

3.2 Scanning probe microscopy

Scanning Probe Microscopy (SPM) is an imaging technique that can achieve nanoscale resolution by scanning a sharp probe across a sample and recording physical properties (such as topography, electrical conductivity, scattered light, etc.) as a function of tip position. As first experimental realization of an SPM, *Binning et. al* introduced the Scanning Tunneling Microscope (STM) [85], where a sharp conducting tip is raster scanned across a conducting sample [16]. A bias voltage is applied between probe and sample, and the tunnelling current is measured. The tunnelling current is a sensitive measure for the distance between tip and sample, as it decays exponentially with increasing tip-sample separation. Therefore, the tunnelling current can be employed as feedback signal in a feedback system for tip-sample distance control. In such a feedback system, the feedback signal (here tunnelling current) has a defined setpoint, and is monitored while scanning the sample. If the feedback signal changes because the tip-sample distance changes even marginally, e.g., due to the topography of the sample, the feedback system adjusts the vertical position of the sample to maintain a constant tip-sample separation. By recording the distance over which the sample has to vertically travel to maintain a constant setpoint while laterally scanning the sample, an image with a spatial resolution down to the Ångstrom level can be recorded. The precise horizontal and vertical movement of the sample for tip-sample distance control is achieved by employing piezoelectric actuators.

Nowadays, one of the most common and most important SPM techniques is Atomic Force Microscopy (AFM) [86, 87]. Figure 3.1 shows an illustration of a typical AFM setup. A sharp tip with typical apex radius between 1 and 50 nm is scanned over a sample surface with sub-nanometer precision using piezoelectric actuators, while the mechanical forces between tip and sample are measured. To detect these forces, the tip is typically mounted at the end of a flexible cantilever, which is bent when the interaction forces change, i.e., due

to topography on the sample. The bending can be monitored by reflecting a laser beam at the back-side of the cantilever to a position sensitive diode (e.g., a two or four segment photodiode, see Fig. 3.1). The position of the reflected laser beam on the diode is used as a feedback signal by a feedback system while laterally scanning the sample below the tip (defined as xy-plane). If we define the z-direction to be perpendicular to the sample surface (vertical) on the sample surface (see definition in Fig. 3.1), the feedback system adjusts the z-position of the sample to maintain a constant tip-sample separation, depending on the deviation of the position of the laser beam on the photodiode in one or the other direction. The distance, which the sample has to move to maintain a constant tip-sample separation, yields the topography of the sample surface. This method is known as *contact mode* AFM [18, 86, 87].

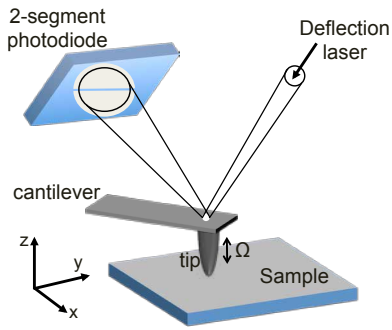

Figure 3.1: Illustration of a typical AFM setup. Figure taken from [88]

Another widely used operation principle is *non-contact mode* AFM [87]. The cantilever oscillates at its mechanical resonance frequency Ω (typically between 10-300 kHz) in close proximity to the sample with oscillation amplitudes A between a few nm and a few tens of nm. A piezoelectric actuator drives the cantilever oscillation, which is monitored by reflecting a laser from the back-side of the cantilever onto a position sensitive diode. Since the oscillation amplitude A is sensitive to interaction forces between tip and sample, it is varied when these forces change, e.g., due to sample topography. Therefore, the oscillation amplitude A can be used as feedback parameter, i.e., it is maintained constant while raster scanning the sample below the tip. This is achieved

by regulating the z-position of the sample through a feedback system using piezoelectric actuators. By recording the distance the sample has to move to maintain a constant tapping amplitude A as a function of lateral tip position, a topography image of the sample with nanoscale resolution is generated.

An AFM, operated in non-contact mode, is typically used as basis for a scattering-type Scanning Near-field Optical Microscopy (s-SNOM). In s-SNOM, optical near fields, i.e., non-propagating electromagnetic waves confined to material boundaries, probe a sample's local optical properties on the nanoscale. Nanoscale resolution can be achieved because optical near fields contain spatial frequencies that are much higher than the spatial frequencies of propagating waves. s-SNOM is the central part of this thesis, and is introduced in the following chapter 3.3.

3.3 Principles of s-SNOM

The electric field in close proximity ($\ll \lambda$) to an illuminated object contains non-radiating electromagnetic fields bound to the objects surface, so-called *near-fields* or *evanescent fields* [11]. The near fields contain much higher spatial frequencies as propagating electromagnetic waves, and can contain information about smallest structural details of the sample. The amplitudes of the near fields and hence the fraction of the high spatial frequencies decay rapidly with increasing distance from the object, and can therefore not be detected with far-field imaging systems. Only spatial frequencies larger than $2/\lambda$ propagate with wavelength λ in the far-field. To record information about the near fields anyway, these fields can be disturbed in very close proximity to the sample's surface by employing for example sharp, nano-metric tips (near-field probes) to transform the evanescent wave into a propagating wave. The detected light in the far-field provides then information about the local optical properties about the near fields at the location of the near-field probe. Instead of using such a near-field probe as nanoscale light collector, it can also be employed as a nanoscale light source, that locally illuminates the sample in the near-field. Then, the far-field scattered light contains local optical information about the sample on the nanoscale, which is the working principle of s-SNOM and is introduced in the following chapter 3.3.

The first scanning near-field optical microscope (SNOM) was proposed by

E. Synge in 1928 [89, 90], although not named as such. Synge proposed to illuminate an opaque screen with an aperture much smaller than the wavelength of the light, in close proximity to a sample surface [91]. On the other side of the aperture, the light decays exponentially in form of an evanescent field and illuminates the sample locally. The interaction with a sample surface in very close proximity transorms the evanescent wave into a propagating wave, which can be detected in the far-field. By scanning the aperture over the sample and by collecting the transmitted light as a function of the sample position, an image with sub-wavelength resolution is recorded. As the recorded transmitted radiation must originate from the aperture, the resolution now depends on the diameter of the aperture rather than the wavelength of the light. Only after the invention of the STM in 1982, the first SNOMs were realised in parallel by D. Pohl [92] and A. Lewis [93] in 1984. Modern aperture SNOM uses a tapered metal-coated optical fiber with a small aperture at its apex as near-field probe (Figure 3.2(a)) [92–94]. Such metal-coated optical fibers are tapered cut-off waveguides, meaning that the propagating electromagnetic wave becomes an evanescent wave that decays exponentially in propagation direction once the diameter of the fiber is smaller than $\lambda/2$. The smaller the opening angle of the fiber, the larger is the distance of the cut-off position to the aperture, resulting in a dramatically reduced transmission. Typically employed aperture probes with an opening angle of 10 to 20° have a transmission of around 10^{-3} to 10^{-6} in the visible spectral range and aperture diameters of around 50 to 100 nm [95]. A further reduction of the aperture diameter would reduce the transmission below the detection threshold, such that the practically achieved resolution is about 50 nm. This implies that in the infrared spectral region, where the wavelength is much longer (several μm), the transmission decreases by orders of magnitudes [96], which makes aperture probes with nanoscale diameter practically not applicable.

Apertureless or *scattering-type Scanning Near-field optical Microscopy* (s-SNOM) [22, 24] overcomes the cut-off limit of aperture probes and enables nanoscale-resolved imaging in the whole visible to the IR and THz spectral range. Instead of employing an aperture as near-field probe, s-SNOM utilizes a metal AFM tip that is illuminated with a focused laser beam (see Fig.3.2(b)), which induces a local electric near-field hot-spot at the tips apex. The near-field interaction between hot-spot and sample modifies the tip-scattered field,

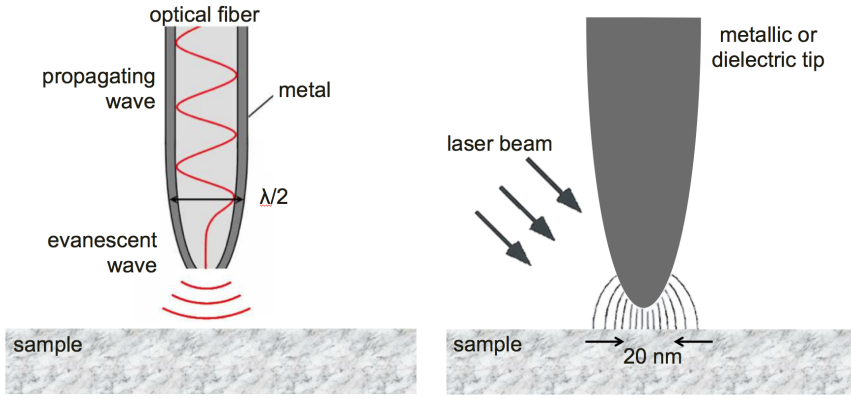

Figure 3.2: a) Metal coated optical fiber as aperture probe in near-field microscopy. b) Metallic or dielectric conventional Atomic Force Microscopy probe as used in scattering-type SNOM. Figure adapted from [95].

which is collected in s-SNOM experiments. s-SNOM is the central part of this thesis and is introduced in detail in the following sections.

Before introducing s-SNOM in detail, two more microscopy and spectroscopy techniques that achieve sub-wavelength, nanoscale resolution in the IR spectral range are briefly mentioned, namely AFM-IR [97–99] based on the photothermal induced resonance (PTIR) effect and photo-induced force microscopy (PiFM) [99–102]. In recent years, both techniques received increased attention as nanoscale IR characterization tools, providing similar information as IR s-SNOM under certain conditions, and are therefore worth to be noted.

In AFM-IR, a pulsed IR laser beam is focused on the sample below an AFM tip. If the IR wavelength corresponds to an absorption band of the sample, the AFM tip can be used to detect the thermal expansion of the sample due to absorption. The rapid thermal expansion of the sample upon illumination with an IR laser pulse causes a force impulse on the tip, inducing an oscillation of the AFM cantilever. The ring-down amplitude of the cantilever vibration is proportional to the absorbed IR radiation, which is measured with a laser that is reflected at the backside of the cantilever. By measuring the response of the AFM tip as a function of wavelength, an IR spectrum of a sample can

be recorded, with a typical resolution of around 100 nm [99, 103–106], or in special cases even 20 nm [107]. Alternatively, the laser can be tuned to a single IR frequency and the sample is scanned below the tip to record an absorption map of the sample. Compared to s-SNOM, the applications of AFM-IR are limited to mostly organic samples that expand significantly upon absorption of IR radiation, whereas in s-SNOM, experiments can be performed regardless of the material (organic or non-organic) and the spectral range. Further, AFM-IR measures the sample's absorption only, whereas s-SNOM provides information about both the sample's reflection and absorption, as will be shown in the following sections and in particular in the result chapter 6.

In PiFM [99–102], a metal-coated AFM tip is illuminated with pulsed, monochromatic laser radiation, inducing a dipole in the tip, which in turn induces a mirror dipole in the sample. PiFM detects mechanically the gradient force that arise from an electric field gradient in the tip-sample junction, which arises from the dipole-dipole interaction between tip dipole and the induced mirror dipole in the sample. If the laser wavelength matches an excitation energy of the sample (such as molecular absorption, but also phonons or plasmons), the attractive force between tip and sample dipole is strongest, which can be measured mechanically by deflecting a laser from the backside of the cantilever [101]. Note that the mechanical read-out mechanism requires to synchronize the laser repetition rate with the cantilever oscillation frequency. By measuring the photo-induced force as a function of wavelength, a spectrum of the sample can be measured with a spatial resolution down to 20 nm [100]. In a different operation mode, a nanoscale optical PiFM image can be recorded by measuring the photo-induced force as a function of sample position while scanning the sample below the tip. Note that PiFM is not only limited to the infrared spectral range, but can be operated at wavelength down to the UV, if appropriate (kHz) pulsed laser sources are available.

This thesis focuses on s-SNOM, which is based on recording information of the near-field interaction between a metallic AFM tip and a sample. These information can be recorded by detecting the electromagnetic field that is scattered by the tip into the far-field, as the tip-scattering is modified by the tip-sample near-field interaction. The modified tip-scattered field originates from the location right below the tip, resulting in a resolution that depends on the size of the tip, which is typically below 20 nm, and can be as low as 5 nm

(see chapter 5). By scanning the sample while detecting the tip scattered field, a nanoscale resolved s-SNOM image can be recorded. As will be shown in the following chapters, s-SNOM typically detects the tip-scattered field interferometrically, which enables to collect simultaneously information about both the reflectivity and absorbance of the sample. Such a correlative measurement is not possible with PiFM (only dipole-dipole force gradient) or AFM-IR (only absorbance). Further, compared to these two techniques, s-SNOM does not rely on particular laser systems, which enables the operation using gas lasers, for example, in the THz or visible spectral range, where PiFM and AFM-IR are restricted to (kHz) pulsed laser sources due to their mechanical read-out mechanism [99] (such that mostly Quantum Cascade Lasers (QCL) in the mid-IR are used). As a third point, s-SNOM can be employed independently of the sample's material (organic or inorganic). This also applies to PiFM applications, where however the image contrast mechanisms are still debated at the time this thesis was written [99]. Nevertheless, AFM-IR is limited to samples that significantly expand upon absorption of radiation (and subsequent heating), which basically limits the applications to mostly organic materials, e.g., polymers or biological matter. The more detailed working principle of s-SNOM and its technical implementation are described in the following chapters.

3.3.1 Tip illumination and nano-focusing

In s-SNOM, a typically 10 - 20 μm long, commercial metal-coated silicon AFM tip, mounted at the end of a cantilever, is illuminated with a focused laser beam (Figure 3.3). The tip acts as an antenna and concentrates the incoming radiation E_{in} to a near-field hotspot at its tip apex on length scales of the apex radius (typically 10 - 30 nm) [11, 108, 109] (Fig. 3.3a). The very high electric fields at the tip apex are generated by charge accumulation due to the lightning rod effect [11] combined with the excitation of surface plasmon polaritons [11, 110, 111]. Fig. 3.3a shows the simulated electric field distribution around a metal (Pt/Ir) tip (apex radius r = 25 nm, length L = 78 μm) that is illuminated by THz radiation (3.11 THz, $\lambda = 96.5$ μm) with polarization parallel to the tip axis (p-polarization). The simulation shows that the electric field is strongly confined in a nano-focus at the tip apex on length scales of a few ten nm, which is much smaller than the illuminating wavelength $\lambda = 96.5$ μm.

When brought into close proximity to a sample, the near fields at the tip

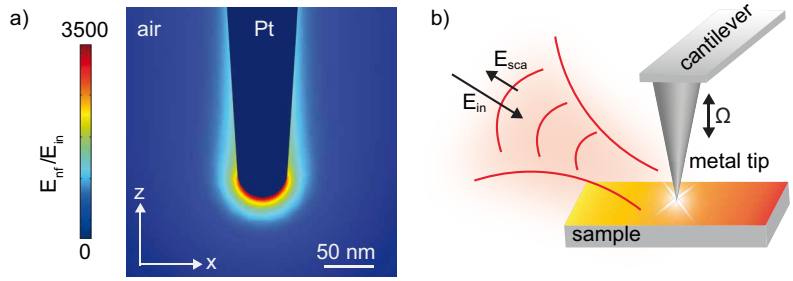

Figure 3.3: **Nano-focus at tip apex and working principle of s-SNOM.** a) Simulated electric field distribution at a Pt/Ir metal tip (radius r = 25 nm, length L = 78 μm) illuminated with electromagnetic radiation of wavelength $\lambda = 96.5$ μm (see Chapter 4.3.2 and 4.3.3 for details) [74]. The color scale denotes the electric field enhancement, i.e., the ratio between local field E_{loc} and incoming field E_{in}. b) Working principle of s-SNOM. A sharp metal AFM tip at the end of a cantilever oscillates at the mechanical resonance frequency Ω of the cantilever. The tip is illuminated with a focused laser beam E_{in}. The tip-scattered radiation E_{sca} is collected as a function of tip position.

apex interact with the sample. This near-field interaction depends on the local optical properties of the sample, and modifies the tip-scattered field E_{sca} (illustration Fig. 3.3b)[24, 39, 112]. By detecting the tip-scattered field, optical information of the sample from the location right below the tip can be collected, resulting in a spatial resolution on length scales of the tip apex (typically around 20 nm). The tip-scattering arising from the tip-sample near-field interaction is the useful signal collected in s-SNOM, and will be referred to as *near-field signal* throughout this thesis.

In s-SNOM, the tip-scattered field E_{sca} is detected in the far-field region, and can be related to the incoming electric field E_{in} by the complex-valued

scattering coefficient $\sigma_{sca} = s_{sca}e^{i\varphi_{sca}}$:

$$E_{sca} = \sigma_{sca}E_{in} = s_{sca}e^{i\varphi_{sca}}E_{in} \tag{3.2}$$

with scattering amplitude s_{sca} and scattering phase φ_{sca}. Note that a more detailed discussion of the scattering coefficient σ will be given in section 3.5, which describes approaches to model the s-SNOM signal. By raster scanning the tip relative to the sample while detecting the scattered field E_{sca} as a function of tip position, a near-field image is recorded. It is generally accepted that essentially the tip's apex radius determines the achievable resolution, which is typically in the range of a few tens of nanometers [11, 25, 28, 113, 114]. Note that for practical reasons the sample is scanned (rather than the tip) to ensure the fixed position of the tip in the focus of the laser beam. This principle was successfully applied in the visible [11, 22, 25–28], the mid-infrared [27, 29–32] and terahertz spectral region [33–37, 72, 115], with wavelength-independent resolution on the nanometer scale.

3.3.2 Background suppression

In addition to the useful near-field signal that arises from the tip-sample near-field interaction, the tip-scattered field is typically dominated by a large background scattering. This background scattering originates from scattering of the incoming field E_{in} at, e.g., the sample surface, the tip shaft, or the cantilever, which are also illuminated by E_{in} as the size of the focus is much larger (several micrometers) than the tip apex (several tens of nanometers). To extract the useful near-field signal, experimental techniques have to be implemented to suppress the background scattering.

The background scattered field can be described by $E_{bg} = \sigma_{bg}E_{in}$, with complex background scattering coefficient σ_{bg}. Hence, the total scattered field is given by $E_{sca} = E_{nf} + E_{bg}$, where the useful near-field signal can be written as

$$E_{nf} = \sigma_{nf}E_{in} \tag{3.3}$$

with near-field scattering coefficient $\sigma_{nf} = s_{nf}e^{i\varphi_{nf}}$. Therefore, the detected intensity at the detector is given by

$$I_{det} \propto I_{sca} = |E_{sca}|^2 = |E_{nf} + E_{bg}|^2 = (E_{nf} + E_{bg})\,(E_{nf} + E_{bg})^*\,. \tag{3.4}$$

To extract the near-field contribution E_{nf}, i.e., to suppress the background, the tip-sample distance A is modulated harmonically with frequency Ω (compare Chapter 3.2), which is achieved by oscillating the tip's cantilever to operate the AFM in non-contact mode. As a consequence, the scattered field E_{sca} is modulated and can subsequently be expressed by the Fourier series

$$\frac{E_{sca}}{E_{in}} = \sigma_{sca} = \sigma_{nf} + \sigma_{bg} = \sum_{n=-\infty}^{\infty} \left[\sigma_{nf,n} + \sigma_{bg,n}\right] e^{in\Omega t} \tag{3.5}$$

where $\sigma_{nf,n}$ and $\sigma_{bg,n}$ denote the n-th order complex-valued Fourier coefficients of σ_{nf} and σ_{bg}.

By harmonically modulating the tip-sample distance with amplitude A, the near-field scattering σ_{nf} can be extracted because the near-field and background contributions of the total scattered field E_{sca} are modulated differently. On the one hand, the near-field scattering arises from the tip-sample near-field interaction, which depends strongly non-linear on tip-sample separation h [11], and is discussed in detail in Chapter 4 and 5. Consequently, the Fourier coefficients $\sigma_{nf,n}$ of the near-field scattering in equation (3.5) are strong for higher orders $n \geq 2$ [39, 116]. On the other hand, the background scattering σ_{bg} varies due to spatial variations of the incident field E_{in} on length scales of the wavelength λ (several μm), while the tip oscillation amplitude A is much smaller in the order of the tip radius R_t (few ten nm) [116]. For that reason, σ_{bg} can be considered to be constant, or to change only linearly with tip-sample separation h only. Therefore, the Fourier coefficients $\sigma_{bg,n}$ of the background scattering in eq. (3.5) are strong for lower order $n < 2$, but approximately equal to zero for higher orders $n \geq 2$ [39, 116]. Hence, by detecting sufficiently high harmonics, $n \geq 2$, the contribution of the background scattering becomes negligible compared to the near-field scattering, $\sigma_{bg,n} \ll \sigma_{nf,n}$ [117], such that $\sigma_{nf,n} = \sigma_{sca,n}$.

However, as the detector measures intensities rather than fields (see eq. (3.4)), simply demodulating the detector signal at higher harmonics of Ω, e.g., with a lock-in amplifier, is not sufficient to extract the pure near-field scattering σ_{nf}. This can be seen by inserting (3.5) into equation (3.4) and neglecting components of the background field $\sigma_{bg,n}$ for $n \geq 1$, such that the

detected scattered field intensity reads

$$I_{det,n} \propto \sigma_{bg,0}\sigma^*_{nf,n} + \sigma^*_{bg,0}\sigma_{nf,n}. \tag{3.6}$$

Equation 3.6 shows that the higher order, background-free near-field scattering coefficient $\sigma_{nf,n}$ is multiplied with the low-harmonic component of the background scattering coefficient $\sigma_{bg,0}$, to which we will refer to as *multiplicative* background. As a consequence, the detection of higher harmonics $n \geq 2$, as it was suggested in the previous paragraph, is not sufficient to measure background-free near-field scattering coefficient σ_n. The remaining background contribution can be fully eliminated with interferometric detection schemes, which will be introduced in the following sections. Furthermore, an interferometric detection scheme allows for a compolex-valued measurement of $\sigma_{nf,n}$, i.e., the amplitude $s_{nf,n}$ and phase $\varphi_{nf,n}$ of the compolex-valued scattering coefficient $\sigma_{nf,n}$, in the following referred to as near-field amplitude and near-field phase signals.

3.3.3 Pseudo-heterodyne interferometric detection

A superior background suppression, as well as the detection of the complex-valued (meaning amplitude- and phase-resolved) near-field scattering coefficient $\sigma_{nf,n}$ can be achieved by interferometric detection of the tip-scattered field E_{sca}. One of the most commonly implemented interferometric detection schemes in s-SNOM is pseudo-heterodyne (ps-het) interferometry [116], which is illustrated in Figure 3.6. It is based on a Michelson interferometer, where a continuous wave (CW) laser emits coherent radiation (beam 1) that is split into two beams by a beamsplitter (BS). The transmitted part (beam 2) is focused with a parabolic mirror onto the tip apex of the s-SNOM. The same parabolic mirror collects and collimates the tip-scattered field E_{sca}. At the beamsplitter it is reflected and guided to the detector (beam 4), where it interferes with the reference beam (beam 3) that was reflected at the reference mirror (RM). The intensity recorded by the detector is then given by:

$$I_{det} \propto |E_{bg} + E_{nf} + E_{ref}|^2 = (E_{bg} + E_{nf} + E_{ref})\,(E_{bg} + E_{nf} + E_{ref})^*\,. \tag{3.7}$$

In ps-het interferometry there exist two modulation mechanisms of the de-

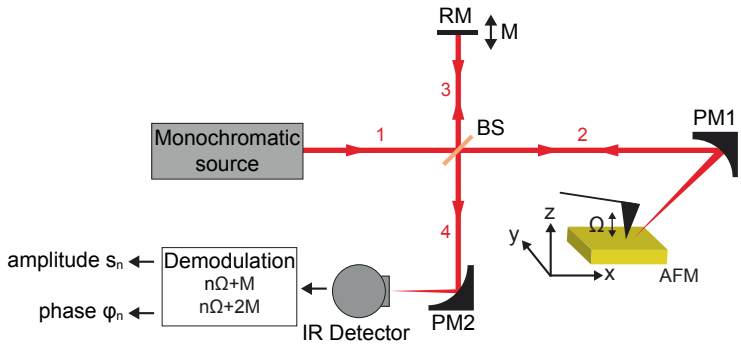

Figure 3.4: **Experimental setup for ps-het s-SNOM imaging.** A laser source generates monochromatic radiation (1), which is divided by a beamsplitter (BS) into a probe beam (2) and a reference beam (3). The tip oscillates in z-direction with frequency Ω and the reference mirror with frequency M. The detector beam path (4) guides both tip-scattering and reference beam to the IR detector, where the interference between both beams is detected. The detector signal is demodulated at frequencies $n\Omega + M$ and $n\Omega + 2M$ to obtain near-field amplitude s_n and phase φ_n.

tected signal I_{det}. On the one hand, the tip-scattered field $E_{sca} = E_{nf} + E_{bg}$ is modulated by the tip vibration with cantilever oscillation frequency Ω (typically few hundred kHz) and its higher harmonics $n\Omega$ due to the tip-sample near-field interaction, as described in the previous Chapter 3.3.2. These fundamental harmonics $n\Omega$ are shown in Fig. 3.5 as black bars in the intensity spectrum I_{det} measured by the detector. The second modulation mechanism arises from a periodic modulation of the length of the reference beam path (beam 3, Fig. 3.6) by vibrating the reference mirror RM at frequency $M \ll \Omega$ (typically few hundred Hz). This modulation yields the time-dependent reference field

$$E_{ref} = E_{in} e^{i(\gamma \sin(Mt) + \psi_{ref})}, \tag{3.8}$$

where γ is the phase modulation amplitude and ψ_{ref} is the phase offset that accounts for the average optical path difference between the signal and reference beam. Due to the interference between the tip-scattered light with the phase-modulated reference beam, sidebands at frequencies $f_{n,m} = n\Omega \pm mM$ (m integer ≥ 1) next to the fundamental harmonics $n\Omega$ appear in the detected

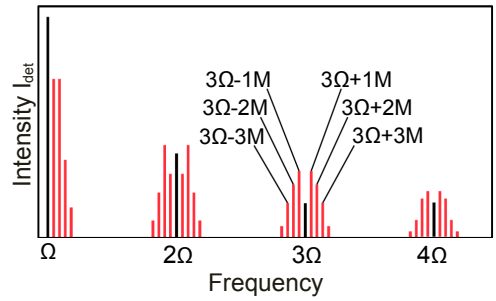

Figure 3.5: Schematic representation of the measured detector signal I_{det} with pseudo-heterodyne interferometric detection. Adapted from [116].

intensity spectrum I_{det} (red bars, Fig. 3.5) [116]. Using the first (m=1) and second sidebands (m=2), the background-free near-field amplitude $s_{nf,n}$ and phase $\varphi_{nf,n}$ of the complex-valued near-field scattering coefficient $\sigma_{nf,n}$ can be calculated according to [116]

$$s_{nf,n} = 2.16k\sqrt{I_{n,1}^2 + I_{n,2}^2} \tag{3.9}$$

and

$$\varphi_{nf,n} = \arctan\left(\frac{I_{n,2}}{I_{n,1}}\right) + \psi_{ref}, \tag{3.10}$$

provided that n is sufficiently large. $k \propto e^{i\,\psi_{ref}}$ is a complex-valued constant related to the interferometer alignment. Note that it is not necessary to determine k, as typically relative material contrasts are measured s-SNOM, i.e., the measured near-field amplitude $s_{nf,n}$ and phase $\varphi_{nf,n}$ signals measured on a specific sample material are normalized to the amplitude $s_{nf,n}^{ref}$ and phase $\varphi_{nf,n}^{ref}$ signals of a reference material. This normalization procedure yields the normalized complex-valued scattering coefficient $\eta_n = \sigma_{nf,n}/\sigma_{nf,n}^{ref} = s_{nf,n}/s_{nf,n}^{ref} \exp\left(i\left(\varphi_{nf,n} - \varphi_{nf,n}^{ref}\right)\right)$. Hence, the factor $2.16k$ and the reference phase offset ψ_{ref} cancel out.

3.3.4 Synthetic optical holography

Synthetic Optical Holography (SOH) [118] is another interferometric detection scheme for amplitude- and phase-resolved s-SNOM imaging and was used in Chapter 5 and 6 of this thesis. The description of the technique in this section

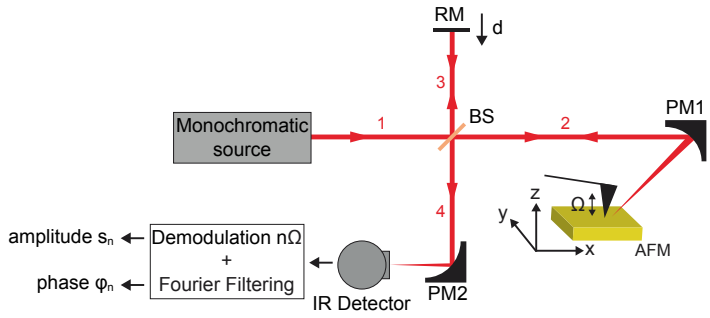

Figure 3.6: **Experimental setup for SOH s-SNOM imaging.** A laser source generates monochromatic, CW radiation (1), which is separated by a beamsplitter (BS) into probe beam (2) and the reference beam (3). Parabolic Mirror PM1 focuses the radiation on the tip, which oscillates vertically with frequency Ω, and collects the tip scattered field, which is guided to the IR detector (4). While the sample is scanned below the tip, the reference mirror (RM) is translated over a distance d. The detected synthetic hologram is demodulated at $n\Omega$ to calculate near-field amplitude $s_{nf,n}$ and phase $\varphi_{nf,n}$ by Fourier Filtering as described in Chapter 3.3.4.

is adapted from reference *Schnell et. al* [118]. In the following the SOH imaging process is explained, and is illustrated exemplarily in Fig. 3.7 with the measurement of a linear dipole antenna antenna (Fig. 3.7a), which exhibits a well-defined antenna resonance at $\lambda = 11$ μm.

In far-field optics, optical holography [119, 120] is an imaging technique where the scattered light from an illuminated object is superimposed with a reference wave. The resulting interference pattern is called a hologram, and encodes the complex optical field scattered from the object. The detection of the complex optical field makes it appealing for the implementation in s-SNOM to detect the complex-valued tip-scattered radiation. However, typically such far-field holography techniques use cameras, i.e., two dimensional arrays of point detectors, to record the hologram, while in s-SNOM only one single point detector is implemented to detect the tip-scattered radiation. Therefore, the holographic detection scheme used in s-SNOM is based on a Michelson interferometer to generate a *virtual* reference wave, which is explained in the following paragraphs.

SOH is based on a Michelson interferometer (see Fig. 3.6). In contrast

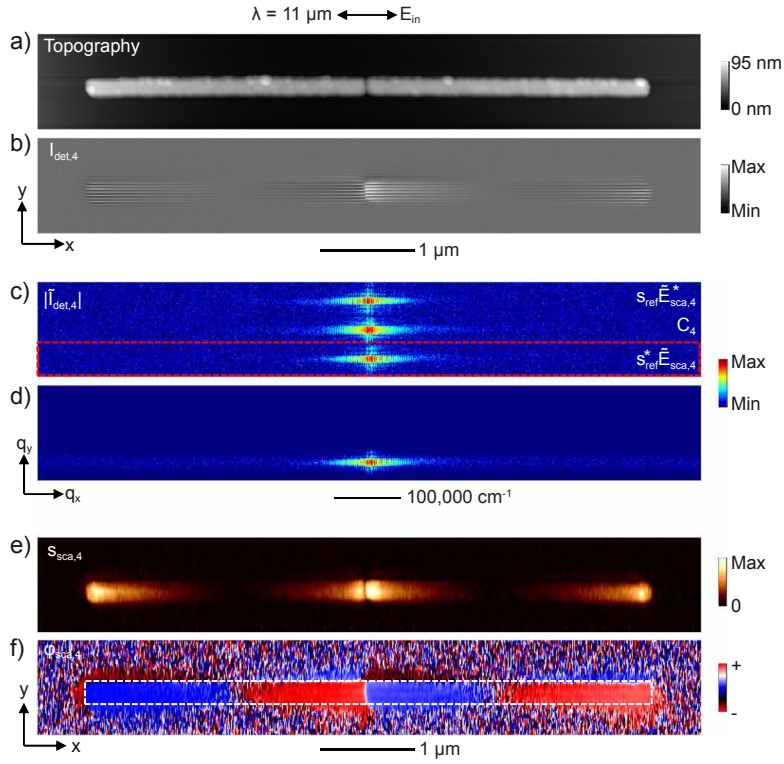

Figure 3.7: **Experimental demonstration of SOH near-field imaging of an IR antenna.** a) AFM topography of the antenna, showing two longitudinally aligned Au rods of 2.9 μm length and 50 nm height, separated by a 50-nm gap and supported on a CaF_2 substrate. b) Hologram $I_{det,4}(\mathbf{r})$, yielding 700 x 100 pixels. Topography and hologram have been acquired simultaneously in 14 min. c) Magnitude of Fourier transform $|\tilde{I}_{det,4}(\mathbf{q})|$ of $I_4(\mathbf{r})$, showing three peaks corresponding to the conjugate term $s_{ref}\tilde{E}^*_{sca,4}$, autocorrelation term C_4 and the direct term $s^*_{ref}\tilde{E}_{sca,4}$ (top to bottom). d) Filtered FT by applying a Hamming window according to the red dashed box in c). e,f) Reconstructed amplitude and phase images, $s_{sca,4}(\mathbf{r})$ and $\varphi_{sca,4}(\mathbf{r})$, obtained by re-centering of g and subsequent inverse FT. Figure taken from reference [118].

to ps-het interferometry, where the phase φ_{ref} of the reference field E_{ref} is harmonically modulated at each pixel with frequency M, SOH varies the reference phase $\varphi_{ref}(\mathbf{r})$ linearly across the image as a function of tip position

$\mathbf{r} = (x, y)$. This is accomplished by slowly changing the reference mirror position $d(\mathbf{r})$ with constant velocity v_{ref} while rapidly scanning the sample below the tip. Thus, the reference phase can be expressed as a function of time according to $\varphi_{ref}(t) = \omega' t + \varphi_0$, with reference phase φ_0 at time $t = 0$ and angular frequency $\omega' = 2\pi \cdot 2v_{ref}/\lambda$. At the same time, the sample is raster-scanned below the tip along the x and y directions of a cartesian coordinate system, with velocities v_x and v_y, respectively. The sample moves rapidly in x-direction and after traveling the full scan length X it returns to the original position at the same speed, and moves in y-direction by one step Δy. Hence, the effective scan speed in y-direction is $v_y = v_x \Delta y/(2X)$. Thus, we can introduce the virtual wave vector $\mathbf{k}_{||} = (k_x, k_y)$ - in analogy to the reference wave vector in classical far-field holography - which is given by $k_x = \omega'/v_x$ and $k_y = \omega'/v_y = 2Xk_x/\Delta y = 2X\omega'/(v_x \Delta x)$, and can write the reference phase as a function of tip position

$$\varphi_{ref}(\mathbf{r}) = \mathbf{k}_{||} \cdot \mathbf{r} + \varphi_0. \tag{3.11}$$

To acquire a synthetic s-SNOM hologram, the tip-scattered field $E_{sca}(\mathbf{r}) \propto \sigma_{sca} = s_{sca}(\mathbf{r}) e^{i\varphi_{sca}(\mathbf{r})}$ is superimposed at the detector with the reference field $E_{ref}(\mathbf{r}) = s_{ref}(\mathbf{r}) e^{i\varphi_{ref}(\mathbf{r})}$ and the n^{th} order demodulated detector signal $I_{det,n}(\mathbf{r})$ is recorded. Hence, by inserting eq. 3.5 into eq. 3.7, $I_{det,n}(\mathbf{r})$ can be written as [118]

$$I_{det,n} = \sum_{l=-\infty}^{\infty} E_{sca,l+n}(\mathbf{r}) E^*_{sca,l}(\mathbf{r}) + E^*_{sca,n}(\mathbf{r}) E_{ref}(\mathbf{r}) + E^*_{ref}(\mathbf{r}) E_{sca,n}(\mathbf{r}). \tag{3.12}$$

Exemplarily, Fig. 3.7b shows the 4^{th} order synthetic optical hologram $I_{det,4}$ of the infrared linear dipole antenna. It exhibits the typical fringe pattern of a hologram in the image plane, which is generated by the interference of the tip-scattering E_{sca} with the reference wave E_{ref} with virtual wave vector $\mathbf{k}_{||}$.

The amplitude $s_{sca,n}$ and phase $\varphi_{sca,n}$ of the demodulated scattered signal $E_{sca,n}(\mathbf{r})$ can be reconstructed by Fourier Transform filtering of the n-th order hologram $I_{det,n}$ with respect to position $\mathbf{r}$. The Fourier Transformation (FT) of the near-field hologram $I_{det,n}(\mathbf{r})$ is shown in Fig. 3.7c and reads

$$\tilde{I}_{det,n}(\mathbf{q}) = C_n(\mathbf{q}) + s_{ref} \tilde{E}^*_{sca,n}(\mathbf{k}_{||} - \mathbf{q}) + s^*_{ref} \tilde{E}_{sca,n}(\mathbf{k}_{||} + \mathbf{q}). \tag{3.13}$$

C_n is the FT of the demodulated term $\sum_{m=-\infty}^{\infty} E_{sca,l+n}(\mathbf{r})E^*_{sca,l}(\mathbf{r})$ in eq. (3.12). $s^*_{ref}\tilde{E}_{sca,n}$ and $s_{ref}\tilde{E}^*_{sca,n}$ are the direct term and its conjugate, which are centered around $\mathbf{k}_{||}$ and $-\mathbf{k}_{||}$, respectively. This is illustrated in Fig. 3.7e and f for n=4, where we can clearly identify the autocorrelation term C_4 in the center of the FT, as well as the terms $s^*_{ref}\tilde{E}_{sca,n}$ and $s_{ref}\tilde{E}^*_{sca,n}$, which are separated into the upper and lower half space of the FT, respectively.

By filtering in Fourier space we can isolate the direct term $s^*_{ref}\tilde{E}_{sca,n}$, as indicated by the red dashed box in Fig. 3.7c and obtain the filtered FT (Fig. 3.7d). By shifting the result to the center of the Fourier plane and by inverse FT we obtain for $n \geq 2$ background free near-field amplitude $s_{nf,n} = s_{sca,n}$ and phase $\varphi_{nf,n} = \varphi_{sca,n}$ images, as shown in Fig. 3.7e and f. The result reveals the expected dipole resonance of the antenna, characterized by strong fields at the rod extremities that are 180° out-of-phase [121]. Note that by filtering the direct term $s^*_{ref}\tilde{E}_{sca,n}$, the *multiplicative* background (compare chapter 3.3.2) is effectively removed [116, 118], as it is only contained in the autocorrelation term $\sum_m (E_{nf,n+m}E^*_{bg,m} + E_{bg,n+l}E^*_{nf,l})$ (compare eq. (3.6)).

3.3.5 Fourier transform infrared nano-spectroscopy

Fourier Transform Infrared nano-spectroscopy (nano-FTIR) is an operation mode of an s-SNOM that records IR spectra with nanoscale resolution [42, 122]. In contrast to the s-SNOM operation modes introduced before, it does not acquire a monochromatic image of a sample, but rather one IR spectrum at one single sample location. The experimental setup is illustrated in Fig. 3.8. A laser emits coherent IR broadband radiation (beam 1), which is divided by a beamsplitter into a probe (beam 2) and a reference beam (beam 3). The probe beam (2) is focused with a parabolic mirror (PM1) onto the tip apex. The same parabolic mirror collects and collimates the tip-scattered field E_{sca}, which is reflected at the beamsplitter and guided to the detector (beam 4), where it interferes with the reference beam (beam 3) that was reflected at the reference mirror (RM). The detector signal is demodulated at higher harmonics $n\Omega$ of the tip oscillation frequency Ω, such that we can assume $\sigma_{sca,n} = \sigma_{nf,n}$ for sufficiently large n (compare chapter 3.3.2).

To acquire a nano-FTIR spectrum, first, the reference mirror is linearly translated over a large distance up to 1600 μm, while recording the demodulated detector signal $I_{det,n}(d)$ as a function of mirror position d. The result of

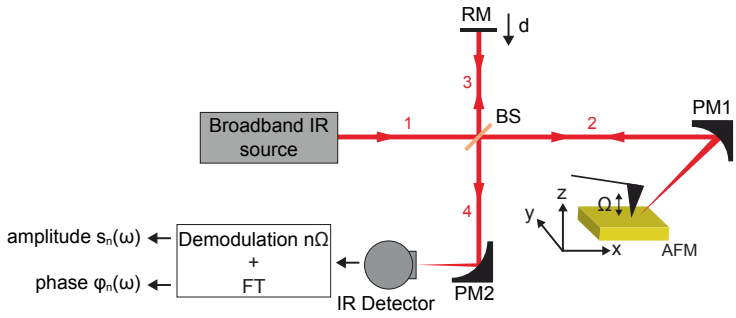

Figure 3.8: **Nano-FTIR spectroscopy experimental setup.** A laser source generates a broadband infrared super-continuum (1), which is separated by a beamsplitter (BS) in probe beam (2) and reference beam (3). The probe beam is focused with the parabolic mirror (PM1) on the vertically oscillating tip. PM1 collects the tip scattered, field which is guided to the detector (4). The reference mirror (RM) is translated over distance d, and the resulting interferogram is detected with an IR detector. Near-field amplitude $s_{nf,n}$ and phase $\varphi_{nf,n}$ are calculated by Fourier Transformation of the n^{th} order demodulated interferogram.

such a measurement is called an interferogram, which is exemplarily shown in Fig. 3.9 for a measurement on silicon. The interferogram shows a fast intensity modulation within an envelope function, which has a maximum in the center $d = 0\ \mu\text{m} \equiv d_0$. This maximum marks the white light position of the interferometer, which occurs when the difference between the two interferometer path have the same length. At this position d_0, the maximum of the envelope is created because the electric fields of all frequencies contained in the broadband beam interfere constructively, because the electromagnetic waves of all frequencies travel the same optical path length. For positions further away from the white light position, the envelope tends to zero because the electric fields of different frequencies interfere either constructively or destructively, resulting in an average signal of zero.

In a second step, the nano-FTIR spectrum is obtained by a complex-valued Fourier transformation $\tilde{I}_{det,n}(\omega)$ of the demodulated n-th order interferogram $I_{det,n}(d)$ with respect to d, yielding $\tilde{I}_{det,n}(\omega)$. Note that, in contrast to standard far-field FTIR spectroscopy techniques, nano-FTIR spectroscopy enables the measurement of the complex-valued tip-scattered field $E_{nf,n}(\omega)$, i.e., near-field

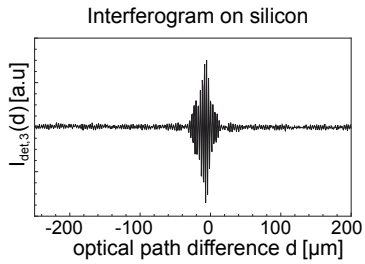

Figure 3.9: Measured Nano-FTIR interferogram $I_{det,3}(d)$ of a silicon sample of total 1400 μm length of 2048 pixel with integration time per pixel of 73 ms. The graph shows a zoom of central region for better illustration.

amplitude $s_{nf,n}(\omega)$ and phase $\varphi_{nf,n}(\omega)$ resolved spectrum, because the sample is located in one of the interferometer arms [42, 44].

In general the reference field as well as the spectral instrument response (i.e., contribution from absorption in air, dispersion of optical components, etc.) are unknown, such that nano-FTIR spectra of a sample of interest are normalized to nano-FTIR spectra of a material that does not exhibit a spectral response (in the IR typically gold or silicon is used). Hence, the normalized nano-FTIR spectrum $\eta_n(\omega)$ reads as

$$\eta_n(\omega) = \frac{\tilde{I}_n(\omega)}{\tilde{I}_n^{ref}(\omega)} \propto \frac{E_{nf,n}(\omega)}{E_{nf,n}^{ref}(\omega)} \propto \frac{\sigma_{nf,n}(\omega)}{\sigma_{nf,n}^{ref}(\omega)}. \tag{3.14}$$

The normalized nano-FTIR spectrum $\eta_n(\omega)$ is generally complex-valued, i.e., it yields the normalized near-field amplitude spectrum $s_{nf,n}(\omega)/s_{nf,n}^{ref}(\omega)$ and phase spectrum $\varphi_{nf,n}(\omega) - \varphi_{nf,n}^{ref}(\omega)$, which will be referred to in the following as $s_n(\omega)$ and $\varphi_n(\omega)$, respectively. Exemplarily, Fig. 3.10 shows the normalized nano-FTIR amplitude $s_3(\omega)$ and phase $\varphi_3(\omega)$ spectrum of the polymer Poly(methyl methacrylate) (PMMA). The normalized nano-FTIR phase spectrum $\varphi_3(\omega)$ (Fig. 3.10b) shows a spectral phase delay of the tip-scattered field due to absorption. It is is characterized by the peak at around 1735 cm^{-1} (dashed black line, Fig. 3.10b), which is associated to the stretching resonance of the C=O bonds in the PMMA molecules. The nano-FTIR phase spectrum can be used to identify absorptive properties of the sample [42, 44, 48], as

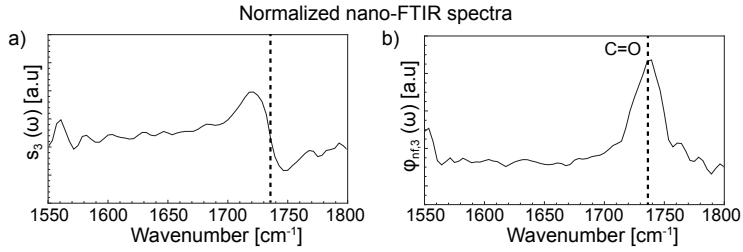

Figure 3.10: **Normalized nano-FTIR a) amplitude $s_3(\omega)$ and b) phase $\varphi_3(\omega)$ spectra of PMMA.** Before calculating the spectra through complex FT, a Hamming Window was applied. As typical for molecular absorption in nano-FTIR, $s_3(\omega)$ exhibits a dispersive behavior, while $\varphi_3(\omega)$ shows an absorption peak. Here, the absorption is due to the stretching of the C=O bond in the PMMA molecules.

will be discussed in detail in Chapter 6. In the nano-FTIR amplitude spectrum $s_n(\omega)$ (Fig. 3.10a), a molecular vibrational resonance is observed as as a dispersive-like shape of the spectrum.

Importantly, nano-FTIR spectroscopy is free of multiplicative background scattering, which was introduced in chapter 3.3.2. This can be seen by first recalling eq. 3.7, which expresses the detector signal I_{det} consisting of the reference wave E_{ref}, the background scattered field E_{bg}, and the near-field scattered field E_{nf}. The detector signal I_{det} is demodulated at higher harmonics $n\Omega$ of the tip oscillation frequency Ω, to suppress the background scattered field E_{bg}. As described in chapter 3.3.2, mathematically this can be shown by expanding E_{nf} and E_{bg} in a Fourier series, which yields the demodulated detector signal $I_{det,n}$ [116]

$$I_{det,n} \propto E^*_{ref} E_{nf,n} + E^*_{bg,0} E_{nf,n} + c.c. \tag{3.15}$$

considering that, for sufficiently large n (typically $n \geq 1$), the background scattered field $E_{bg,n} \approx 0$, but $E_{nf,n} \neq 0$. Eq. (3.15) still contains the multiplicative background term $E^*_{bg,0} E_{nf,n}$, which is removed in nano-FTIR spectroscopy employing the interferometric detection scheme as described in the following paragraph.

To record an interferogram, the reference mirror is translated linearly while recording the demodulated detector signal $I_{det,n}$ as a function of mirror po-

sition d, yielding the interferogram $I_{det,n}(d)$. The mirror translation causes a phase change of the reference wave according to $\phi_{ref} = d\omega/c$ for each spectral frequency ω of the reference field. Thus, the interferogram can be written as [123]

$$I_{det,n}(d) \propto \int \left(E^*_{ref}(d_0) e^{-id\omega/c} E_{nf,n} + E^*_{bg,0} E_{nf,n} + c.c. \right) d\omega, \tag{3.16}$$

where $E_{ref}(d_0)$ is the reference field at the white light position $d = 0$. In equation (3.16), the multiplicative background is contained in the term $E^*_{bg,0} E_{nf,n}$ and does not depend on the mirror position d. Hence, in the Fourier Transform $\tilde{I}_n(\omega)$ of the interferogram in eq. (3.16), i.e., in the calculated nano-FTIR spectrum, only the part of the spectrum for $\omega = 0$ contains the background field $E_{bg,0}$. Then, for $\omega > 0$ the acquired complex nano-FTIR spectrum reads as

$$\tilde{I}_{det,n}(\omega) \propto E_{ref}(d_0)^* E_{nf,n}, \tag{3.17}$$

which shows that through the asymmetric interferometric detection, the nano-FTIR spectrum does not contain any multiplicative background.

3.4 Experimental setup

In this work, two commercial s-SNOM (neaSNOM, Neaspec GmbH) for the IR and THz spectral range, respectively, were used as central part for all experiments, i.e., to perform CW nano-imaging and nano-FTIR spectroscopy. The laser light sources and all optics to manipulate and guide the laser beam to the s-SNOM were set up as part of the experimental scope of this work, which is shown in a simplified schematic in Figs. 3.11 and 3.12. In all experiments, the sample was placed below a cantilevered AFM tip (marked with black dot in Figs. 3.11 and 3.12), and illuminated with a focused laser beam through the parabolic mirrors PM1 (for IR) or PM2 (for THz).

First, the infrared setup is described. For CW infrared s-SNOM imaging, either a tunable CO_2 ($\lambda = 9.3\ \mu m - 10.7\ \mu m$, *Access Laser Company*, model *Merit G*) or a Quantum Cascade Laser (QCL) ($\lambda = 5.7\ \mu m - 6.7\ \mu m$, *Daylight Solutions Inc.*, model number *21060*) can be selected through Indium Tin Oxide (ITO) windows ITO2 and ITO3. ITO is a conductive coating that is transparent for visible light, but reflects infrared radiation. By coating, e.g.,

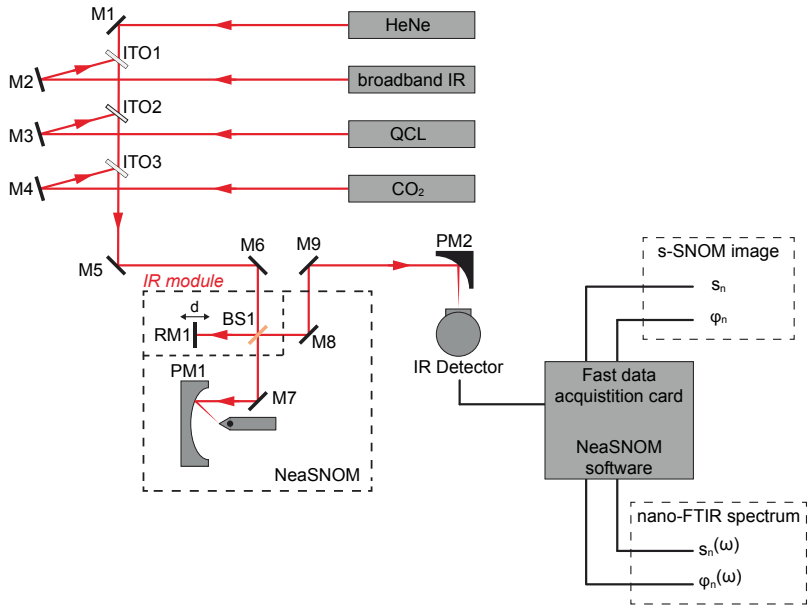

Figure 3.11: **IR s-SNOM setup used in this work.** The experimental setup comprises a neaSNOM near-field microscope, beamsplitter (BS1), a moving reference mirror (RM1), and a IR detector. As IR light sources are employed a CO_2 laser and a QCL for s-SNOM imaging, and a broadband IR super-continuum for nano-FTIR spectroscopy. A HeNe laser is used for alignment purposes only, several optical components (such as mirrors and windows) are used for guiding and selecting the respective laser beam, and a computer with a fast data acquisition card and the neaSNOM software is used for recording the data.

glass with ITO, such an ITO window can be used to combine the IR lasers and the HeliumNeon (HeNe, $\lambda = 633\ nm$) pilot laser. The HeNe laser beam is used for guiding and alignment of the IR beam, as IR radiation is not visible to the human eye, but the read beam of the HeNe laser is. Both IR lasers can be coupled into the s-SNOM by folding mirrors M5 and M6. A Zinc Selenide (ZnSe) beamsplitter BS1 divides the beam into sample and reference beam to form a Michelson interferometer. While the sample beam is focused on the tip and the sample is scanned below the tip, a piezoelectric stage moves the reference mirror RM1 of the IR module by a distance d in order to operate the

interferometer in Synthetic Optical Holography (SOH) mode. BS1 combines sample and reference beams, and a parabolic mirror PM2 focuses them onto a liquid nitrogen cooled detector surface (*Infrared Associates, Inc*, model *FTIR-16-0.10*). The detector signal is recorded with a fast data acquisition card, and the neaSNOM software calculates the demodulated near-field amplitude $s_{nf,n}$ and phase $\varphi_{nf,n}$ images according to Chapter 3.3.4.

To perform nano-FTIR spectroscopy, the broadband IR laser beam (ω = 800 cm^{-1} - 2000 cm^{-1}) based on difference frequency (DFG) was used. The broadband coherent mid-IR laser beam is generated by synchronously superimposing two pulsed near-infrared beams (*Toptica AG*, models *FFPro-IR* and *FFPro-SCIR*) in a GaSe crystal [41, 42, 124]. For nano-FTIR spectroscopy experiments, the mid-IR broadband beam is selected via ITO1, and split by BS1 into sample and reference beam. The reference mirror RM1 is moved over a distance d to record an interferogram via the IR detector, and nano-FTIR amplitude $s_n(\omega)$ and phase $\varphi_n(\omega)$ are calculated by the neaSNOM software according to Chapter 3.3.5.

Finally, to perform THz s-SNOM imaging, the THz laser beam (f = 0.8 THz - 7 THz, *Coherent Inc.*, model *SIFIR-50 FPL*) can be selected by ITO4 and coupled into the s-SNOM with mirror M13. The interferometer of the THz module is operated in SOH mode in exact analogy to the IR module, incorporating an undoped Silicon (Si) beamsplitter BS2 and reference mirror RM2. The THz radiation is then detected with a liquid Helium cooled Indium Antimonide hot electron bolometer (*QMC Instruments*, model *QFI/XB*), and evaluated via the s-SNOM software to calculate s-SNOM amplitude s_n and phase φ_n according to Chapter 3.3.4.

3.5 Models of tip-sample near-field interaction

In Chapter 3.3.1 it was described that the tip-sample interaction (referred to as near-field interaction) yields a near-field scattering that contains information about the local optical properties of the sample. In order to understand the signal measured in s-SNOM and obtain useful information about the sample, theoretical models of the near-field interaction are required. Two simple models are the Point Dipole Model (PDM) [40] and the Finite Dipole Model (FDM) [125], which have been successfully applied to describe predict the

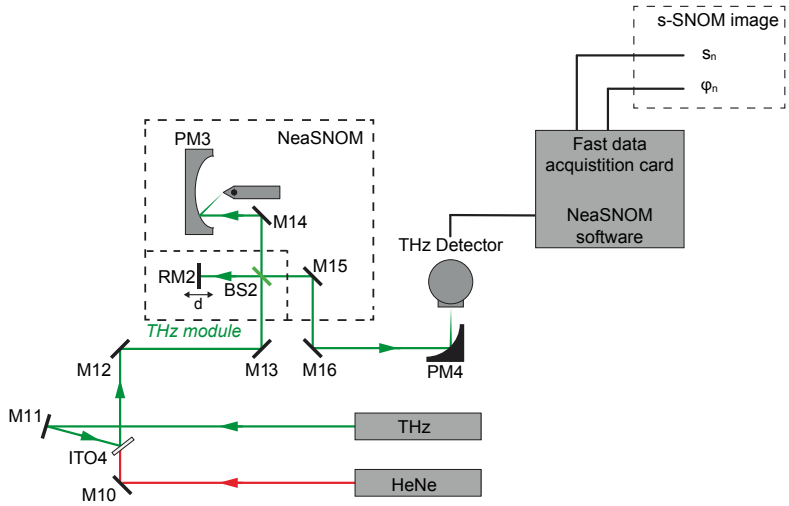

Figure 3.12: **THz s-SNOM setup used in this work.** The experimental setup comprises a neaSNOM near-field microscope, a beamsplitter (BS2), a moving reference mirror (RM2), and a THz detector. As THz light source is employed a Methanol gas laser. A HeNe laser is used for alignment purposes only, several mirrors are used for guiding and selecting the respective laser beam, and a computer with a fast data acquisition card and the neaSNOM software is used for recording the data.

s-SNOM near-field contrasts of polymers [31], metals [31], near-field phonon resonances [29, 126] and semiconductors [39]. Both models will be described in the following (adapted from reference [127] and [128]). They are illustrated in Figure 3.13.

3.5.1 Point-dipole model

In s-SNOM, the tip is illuminated by the incident electric field E_{in} and scatters the field E_{sca} into the far-field (compare Chapter 3.3.1). The ratio between E_{sca} and E_{in} is the complex-valued scattering coefficient $\sigma = E_{sca}/E_{in}$ [40]. As the tip is illuminated directly and via reflection at the sample surface, the total field at the tip location can be written as $(1 + r_s)E_{in}$, with r_s being the far-field reflection coefficient of the sample surface. This field polarizes the tip, inducing the dipole moment $p_t \propto \alpha_{eff}(1 + r_s)E_{in}$, with α_{eff} being the

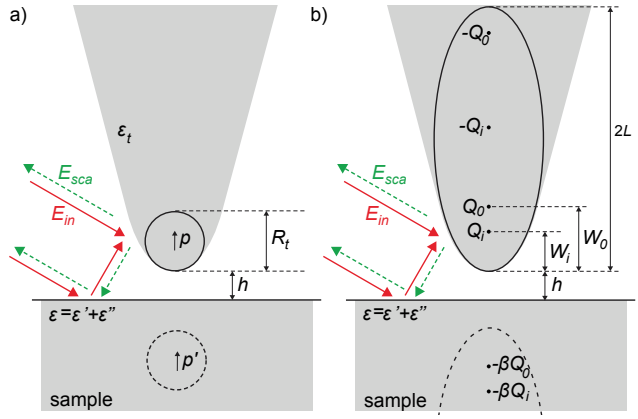

Figure 3.13: Schematics of the a) Point Dipole Model, and b) Finite Dipole Model.

effective polarizability of the tip. Note that α_{eff} is an important parameter, as it accounts for the near-field interaction between tip and sample and carries the information about the optical properties of the sample. By reciprocity, the tip scatters directly and via reflection at the sample surface into the far-field, yielding the total tip-scattered field $E_{sca} \propto (1 + r_s)p_t$ [28, 40, 125, 129]. Thus, the complex-valued scattering coefficient is given by

$$se^{i\varphi} = \sigma = \frac{E_{sca}}{E_{in}} \propto \alpha_{eff}(1 + r_s)^2, \tag{3.18}$$

with s and φ being scattering amplitude and phase, respectively. In general, this scattering coefficient is complex-valued, where the phase φ represents a potential phase shift between E_{sca} and E_{in} for a non-zero imaginary part of the sample's dielectric permittivity.

In the Point Dipole Model (PDM), the tip is approximated by a sphere with radius $R_t \ll \lambda$, dielectric permittivity ϵ_t, dipole moment p, and polarizability α, as illustrated in Fig. 3.13a. The polarizability of the sphere in air ($\epsilon_{air} \approx 1$) is given by

$$\alpha = 4\pi R_t^3 \frac{\epsilon_t - 1}{\epsilon_t + 2}. \tag{3.19}$$

As the radius R_t of the sphere is much smaller than the incident wavelength λ, the problem can be treated in the electrostatic limit of Mie-Theory [130, 131],

also known as Rayleigh-scattering. In this limit, the overall dipole moment of the sphere p can be described by a point dipole located in the center of the sphere. Above a sample surface, this point dipole p induces a mirror dipole $p' = p(\epsilon - 1)(\epsilon + 1)$ below the sample surface, which interacts with the tip dipole p. The quasi-static solution of the problem yields the tip's effective polarizability [40]

$$\alpha_{eff} = \frac{\alpha}{1 - \frac{\alpha\beta}{16\pi(h+R_t)^3}}, \tag{3.20}$$

with h being the height of the tip above the sample. β is the quasi-static near-field reflection coefficient that depends on the local dielectric function of the sample, ϵ, and is given by:

$$\beta = (\epsilon - 1)/(\epsilon + 1). \tag{3.21}$$

Equations (3.18), (3.20) and (3.21) express the relation between the tip-scattered field E_{sca} and the samples dielectric permittivity ϵ. In practice, however, E_{sca} also contains a strong background contribution E_{bg}, such that $E_{sca} \neq E_{nf}$ (compare Chapter 3.3.2). These background fields can be removed by employing interferometric detection schemes, such as pseudo-heterodyne detection (compare Chapter 3.3.3) or SOH (Chapter 3.3.4), which detect n^{th} order demodulated scattered field E_n, such that $E_n \approx E_{nf,n}$. Using eq. (3.18), E_n can be described by

$$E_n = \sigma_n E_{in} \propto \alpha_{eff,n}(1 + r_s)^2 E_{in} \tag{3.22}$$

with σ_n and $\alpha_{eff,n}$ being the n^{th} order Fourier coefficients of σ and α_{eff} with respect to tip height h, respectively.

Note that during s-SNOM imaging, ideally all parameters that effect the near-field scattering, except the sample's permittivity ϵ, are constant (such as incident field E_{in}, the reflection coefficient of the sample r_s, the tip's permittivity ϵ_t), such that $E_n \propto \alpha_{eff}$. Therefore, when scanning over different materials, and the permittivity of the sample ϵ is in good approximation the only parameter responsible for the s-SNOM material contrast mechanism. Such s-SNOM contrasts between different materials can hence be used to deduce information about the relative permittivity of the sample, ϵ [40, 44, 132].

Note that the PDM does not take into account the finite, elongated geometry of the tip [29, 66, 125, 133]. Therefore, more sophisticated models have been

developed, which can describe experimental s-SNOM data more quantitatively. This is particularly important for materials exhibiting strong resonances such as phonons or plasmon polaritons [125]. One of such superior models to predict s-SNOM material contrast is the Finite Dipole Model (FDM), which will be introduced in the following chapter 3.5.2.

3.5.2 Finite dipole model

For a better quantitative description and prediction of s-SNOM contrasts and nano-FTIR spectral peak positions, the Finite Dipole Model (FDM) was introduced [125, 134]. This model takes into account the elongated shape of the tip as illustrated in Figure 3.13b. The FDM approximates the tip by a perfectly conducting spheroid with length $2L$, which is located above a semi-infinite half-space representing the sample surface. The spheroid is polarized by an illuminating electric field E_{in}, with polarization parallel to the semi-major axis of the spheroid. The resulting electric field around the spheroid can be approximated by the electric field of two opposite point charges $\pm Q_0$ located in the apexes of the spheroid. These two point charges $\pm Q_0$ form the dipole moment $p_0 \approx 2LQ_0$ [117, 125, 128] (see sketch in Fig. 3.13b). Placing the spheroid above a sample surface, the FDM assumes that only the lower charge Q_0 contributes to the near-field interaction between tip and sample. This interaction can be described by a mirror charge below the sample surface with magnitude $Q_0' = -\beta Q_0$. β is the quasi-static reflexion coefficient as for the PDM in section 3.5.1. The mirror charge acts back on the spheroid, inducing the additional point charges Q_i and $-Q_i$, where only the charge Q_i (which is closer to the sample) and its image $Q_i' = -\beta Q_i$ contribute to the near-field interaction [125]. Note that Q_0 depends on the incident field and the geometry of the spheroid, but Q_i is a function of the dielectric properties of the sample.

Through a self-consistent treatment [117, 125, 128] of the problem, the induced charge Q_i can be written as:

$$Q_i = \beta \left(f_0 Q_0 + f_i Q_i \right) \tag{3.23}$$

where the geometric properties of the system are included in the functions f_0

and f_i:

$$f_{0,i} = \left(g - \frac{R_t + 2h + W_{0,i}}{2L} \frac{ln\frac{4L}{R_t+4h+2W_{0,i}}}{ln\frac{4L}{R_t}} \right). \tag{3.24}$$

$W_0 \approx 1.31R_t$ and $W_i = R_t/2$ (compare Fig. 3.13b) are the positions of the point charges Q_0 and Q_i, respectively, which can be deduced by considering the actual image charge distribution within the spheroid [125]. g is an empirical complex-valued factor describing the total charge induced in the spheroid. For typical infrared s-SNOM experiments one finds $|g| = 0.7 \pm 0.1$ [44, 117, 125].

The effective polarizability α_{eff} and hence the field E_{sca} scattered by the spheroid can be calculated by also considering the opposite point charge $-Q_i$ placed in the center of the spheroid in order to preserve charge neutrality [125, 128]. As a consequence, the two point charges $\pm Q_i$ form the dipole moment $p_i \approx Q_i L$, which is induced by the near-field interaction between tip and sample. Then, the effective polarizability α_{eff}, which is proportional to the tip-scattered field E_{sca} (compare eq. (3.18)), can be calculated from the ratio between p_0 and p_i [125, 128]:

$$\alpha_{eff} \propto \frac{p_i}{p_0} + 1 = \frac{1}{2} \frac{\beta f_0}{1 - \beta f_i} + 1 \tag{3.25}$$

By using the same argumentation as for the PDM (compare Chapter 3.5.1), it can be shown that the scattering coefficient $\sigma = E_{sca}/E_{in}$ is proportional to the effective polarizability (eq. (3.25)). Hence, using eq. (3.22), the measured n^{th} order s-SNOM material contrasts can be modeled by calculating the n^{th} order Fourier coefficients of α_{eff} with respect to tip height h.

3.5.3 Finite dipole model for layered samples

The Finite Dipole Model can be extended to account for a bulk sample with one layer on top, which is relevant for layers with thickness smaller than the near-field penetration depth into the sample (see Chapter 6). The description of the model in this section is adapted from reference *Hauer et al.* [128]. As illustrated in the sketch in Fig. 3.14, this model approximates the charge distribution in the tip apex by the monopole Q at distance z_0 above the sample surface, in a similar way as for the FDM. For a bulk sample covered with a layer of thickness d, the electric potential response Φ to the charge Q can be

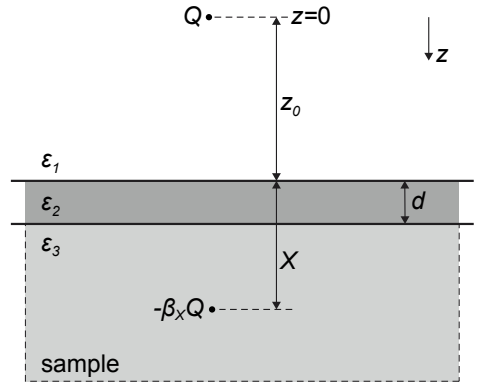

Figure 3.14: **Sketch of the Finite Dipole Model extended to layered samples.** Monopole Q at distance z_0 above the surface of a layer with thickness d. ϵ_i for $i = 1, 2, 3$ are the dielectric functions of air, layer, and sample, respectively. The potential response Φ of the sample is approximated by the monopole $-\beta_X Q$ at distance X below the sample surface. Figure adapted from ref. [128].

calculated by solving the boundary conditions for the total potential U and its derivative [128, 135]. The explicit expressions for U and Φ are given in Appendix A.

As presented in reference *Hauer et al.* [128], by using the electric potential response Φ, the formalism of the FDM can be extended to layered samples by approximating the potential response Φ by the potential of a point charge $Q' = -\beta_X Q$ at distance X under the sample surface (see sketch in Fig. 3.14). To determine β_X and the position X of the point charge Q', the potential and electric field of Q' have to coincide with the actual response of the sample at $z = 0$ (position of monopole Q). Enforcing these boundary conditions, which is not presented in detail here, leads to the important result [128]

$$\beta_X = -\left.\frac{\Phi^2}{\Phi'}\right|_{z=0} \tag{3.26}$$

and

$$X = \left.\frac{\Phi}{\Phi'}\right|_{z=0} - z_0. \tag{3.27}$$

These expressions for β_X and X can be used to extend the FDM to layered samples by evaluating $\beta_X^{0,i}$ and $X^{0,i}$ for Q_0 and Q_i, respectively (compare Fig.

3.13 and Eq. (3.23)), and inserting a modified version of Eq. (3.24),

$$f_{0,i} = \left(g - \frac{R_t + h + X_{0,i}}{2L} \right) \frac{ln\frac{4L}{R_t+2h+2X_{0,i}}}{ln\frac{4L}{R_t}}, \tag{3.28}$$

and $\beta_X^{0,i}$ into the expression for the effective polarizability α_{eff} in Eq. (3.25).

4 Cantilevered THz-resonant antennas with nanoscale tip apex

In this chapter, the development THz-resonant scanning probe tips that yield strongly enhanced and nanoscale confined THz near fields at their tip apex is presented. The tips with length in the order of the THz wavelength ($\lambda = 96.5\ \mu m$) were fabricated by focused ion beam (FIB) machining and attached to standard atomic force microscopy (AFM) cantilevers. Measurements of the near-field intensity at the very tip apex (25 nm radius) as a function of tip length, via graphene-based (thermoelectric) near-field detection, indicate their first and second order geometrical antenna resonances for tip length of 33 and 78 μm, respectively. On resonance, we find that the near-field intensity is enhanced by one order of magnitude compared to tips of 17 μm length (standard AFM tip length), which is corroborated by numerical simulations that further predict remarkable intensity enhancements of about 10^7 relative to the incident field. Because of the strong field enhancement and standard AFM operation of our tips, we envision manifold and straightforward future application in scattering-type THz near-field nanoscopy and THz photocurrent nano-imaging, nanoscale nonlinear THz imaging, or nanoscale control and manipulation of matter employing ultra-strong and ultrashort THz pulses.

4.1 Introduction

Terahertz (THz) radiation [136, 137], loosely defined between 0.1 and 10 THz (wavelength $\lambda = 3000 - 30\ \mu m$)[136], can access vibrational and rotational resonances in molecules[19, 138, 139] and low-energy dynamic processes in solid-state matter or devices[139–141]. For many applications, a strong THz field concentration is required, for example, for high-resolution THz imaging or for THz sensing of small amounts of matter [136, 138]. This can be accomplished by focusing THz radiation using far-field optics. However, the focal

spot size is limited by diffraction to about $\lambda/2 = 15 - 1500\ \mu m$. A nanoscale field confinement can be achieved by concentrating THz radiation with the use of metal antennas [142, 143], sharp metal wires [38, 138, 144–146], or subwavelength apertures or slits [138, 146–148]. In particular, the THz field concentration at a sharp tip apex can be achieved by exploiting the lightning rod effect, or by adiabatic compression of an electromagnetic wave propagating along a long, tapered metal wire [38, 145, 147, 149, 150]. Field confinements as large as $\lambda/4600$ have been already reported [151]. Applications of near-field enhancement at nanoscale metal tips include the THz control of photoemission [152], nanoscale-resolved THz scattering-type scanning near-field microscopy (s-SNOM) [33, 37, 153, 154], ultrafast sub-cycle THz nano-spectroscopy [155] or THz photocurrent nanoscopy [156].

In many experiments, the illuminated metal tip is much longer than the THz wavelength λ, in order to guarantee strong near-field enhancements and scattering from the tip. For subwavelength-scale THz imaging, the rather long tips of a scanning tunneling microscope (STM) [156–158] can be employed. In the case of nonconducting samples, the long metal tips can be scanned over the sample surface via shear-force control that utilizes a tuning fork [159, 160]. Alternatively, the tips of standard AFM cantilevers may be used for THz near-field imaging [37, 155]. While this approach can be performed with standard and easy-to-use AFM instrumentation, the AFM tips suffer from low field enhancement due to the large mismatch between tip length ($\ll \lambda$) and THz wavelength λ. AFM tips of a length on the order of the THz wavelengths potentially exhibiting geometric antenna resonances that provide large field enhancements have not been developed yet, despite their advantage to enable nanoscale THz control and imaging applications based on widely available AFM instrumentation.

In this thesis, we developed cantilevered antenna probes with nanoscale tip apex for resonant nano-focusing of THz radiation. Their lengths were designed to support antenna modes to resonantly enhance the THz field at the tip apex. We attached the antennas to standard AFM cantilevers to allow for a precise control of the position of the THz hotspot on a sample surface using standard AFM instrumentation. To characterize the antenna probes, we measured the near-field intensity directly at the tip apex using a graphene-based THz photodetector [64, 161], rather than deducing it by detecting the tip-scattered

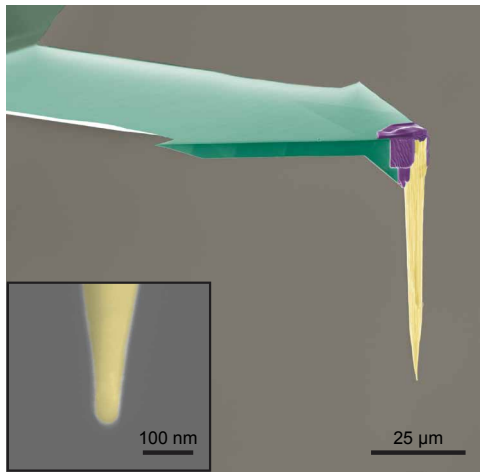

Figure 4.1: False color SEM image of a FIB fabricated THz antenna tip showing Si cantilever (green), FIB deposited Pt (purple) and the Pt/Ir antenna tip (yellow).

light in the far field. We find that our tips support antenna resonances and corroborate our findings with numerical simulations and antenna theory.

4.2 Tip fabrication

Fig. 4.1 shows a false color scanning electron microscopy (SEM) image of a FIB fabricated THz antenna probe using a Helios 450 DualBeam (FEI, Netherlands) electron microscope [73, 162]. To fabricate the THz antenna probes we use standard Si AFM cantilevers (*Nanoworld*, model *Arrow NCR*, Switzerland) and replaced the original tip by a several tens of micrometers long solid metal tip. To illustrate the fabrication process, we show in Figure 4.2 SEM images of different fabrication steps. As basis we used the Si AFM cantilevers, where we first cylindrically remove the tip as shown in Figure 4.2 a) and b). Then, a high aspect ratio conical tip is milled out of a solid Pt80/Ir20 wire (supplied by *Advent Research Materials*, England) (Fig. 4.2 c), cut at the desired length and fitted into the cylindrical grove in the Si cantilever (Fig. 4.2 d). The cone was attached by FIB induced deposition of platinum (purple, Fig. 4.1). Finally, to achieve a high field confinement and enhancement, the tip apex

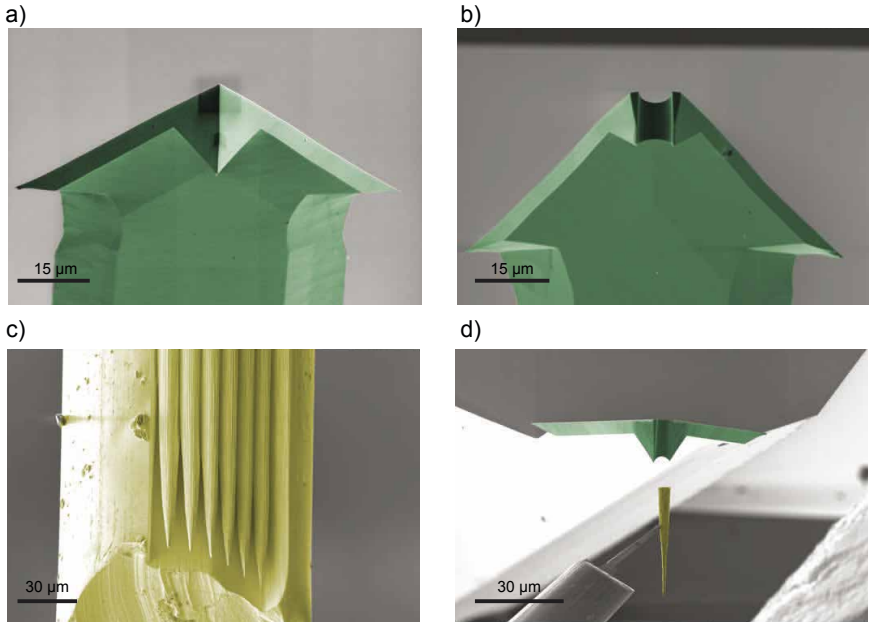

Figure 4.2: Illustration of the FIB fabrication process of resonant THz antenna probes. a) Several cones cut from a 125 μm thick Pt/Ir wire. b) Commercial Si AFM tip (NanoWorld, Arrow NCR). The ion beam is moved along the red dashed line to remove the original tip c) Si AFM cantilever with tip removed. d) A pre-milled Pt/Ir cone is fitted into the prepared cantilever and attached using focused ion beam deposition of Pt.

was sharpened and adjusted to a diameter of (50 $\pm$ 3 nm). This was achieved by circular ion milling along the tip axis, while monitoring the apex diameter with the electron beam and adjusting the milling parameters such as the ion beam current. The value of 50 nm was chosen due to its high reproducibility and better comparability with standard Pt/Ir coated AFM tips, which have a similar apex diameter. In principle a further reduction of the tip apex diameter below 10 nm is possible [75]. In total we fabricated six different tips with lengths 17 μm, 33 μm, 43 μm, 55 μm, 65 μm, and 78 μm (see Figure 4.3), in order to study the near-field intensity at the tip apex as a function of tip length.

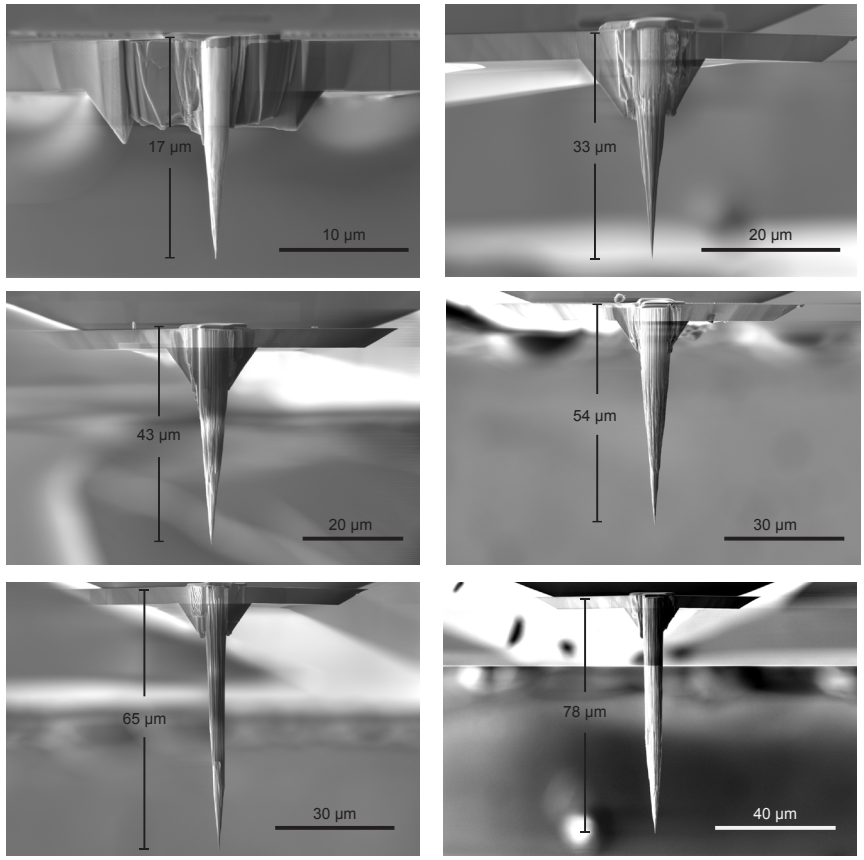

Figure 4.3: Length measurement of six fabricated THz antenna tips.

4.3 Tip characterization

4.3.1 Graphene split-gate near-field detector

To characterize the cantilevered THz antennas, we employed them as scanning probe tips in a scattering-type Scanning Near-field Optical Microscope (*Neaspec GmbH*, model *s-SNOM*, Germany), as described in Chapter 3. The tip is oscillating vertically at the mechanical resonance frequency Ω with oscillation amplitude was 40 nm. The tips were illuminated with the focused THz beam ($\lambda = 96.5\ \mu m$, 3.11 THz) of a gas laser (*Coherent Inc.*, model *SIFIR-50 FPL*, USA), which provides monochromatic radiation up to 100 mW power. In con-

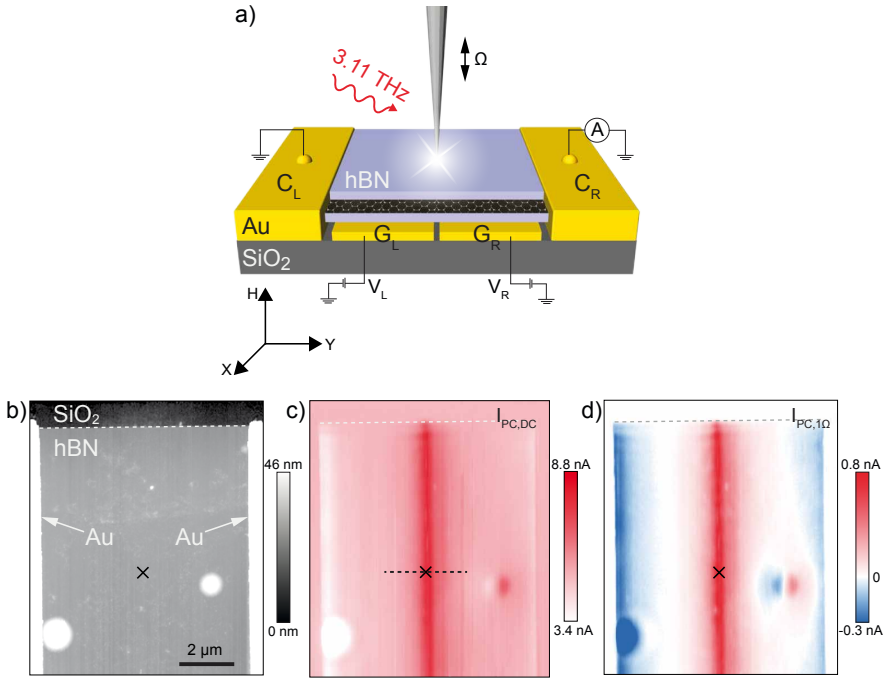

Figure 4.4: **Terahertz antenna tip and THz near-field detector:** a) Schematics of the THz near-field detector. The laser illuminated antenna probe concentrates the light in the near-field region of the tip apex. The near-field induced photocurrent in the hBN-graphene-hBN heterostructure is detected through the two lateral contacts, C_L and C_R. Applying voltages V_L and V_R to the two backgates, G_L and G_R, allows one to separately control the carrier concentration in the graphene to the left and to the right of the gap between them. b) AFM topography image of the THz near-field detector. c,e) Images of direct (photo)current (DC), $I_{PC,DC}$ and photocurrent recorded at frequency 1Ω $I_{PC,1\Omega}$. The white/gray dashed horizontal lines mark the edge of the graphene device. The black cross identifies the position of the measured approach curves shown in Fig. 4.6. The horizontal dashed black line marks the line profiles in Fig. 4.8.

trast to standard s-SNOM, we did not detect the tip-scattered field but used a graphene-based THz detector [64, 163] (illustrated in Fig. 4.4 a) to measure the near-field intensity directly at the tip apex. The detector device [64, 163]

was fabricated by Yuanda Gao and James Hone from Columbia University in New York City (USA), and Kenji Watanabe and Takashi Taniguchi from the National Institute for Material Science in Tsukuba, Japan, and consists of a graphene sheet encapsulated between two layers (9 nm top, 27 nm bottom) of hexagonal Boron Nitride (hBN). This hBN-graphene-hBN heterostructure is placed on top of two gold backgates, which are laterally separated by a gap of 150 nm. By applying voltages V_L and V_R to the gates, the carrier concentration in the graphene can be controlled separately. In our experiment we have chosen the carrier concentrations $n_{L/R} = +/- 2.6 \times 10^{11} cm^{-1}$, yielding a sharp pn-junction across the gap between the two gates. When the tip is placed above the gap, the near field at the apex locally heats the electrons in the graphene, yielding a photocurrent I_{PC} according to $I_{PC} = (S_L - S_R) * \Delta T$ [64, 163, 164]. Here, ΔT is the local temperature gradient below the tip and $(S_L - S_R)$ is the local variation of the Seebeck coefficient S (in our device generated by the strong carrier density gradient i.e. the pn-junction above the gap). The photocurrent I_{PC} is measured via the two lateral source and drain gold contacts C_L and C_R, and is found to be proportional to the near-field intensity [165] for the power applied in our experiments, as shown in Fig. 4.5. Then, for fixed gate voltages, the photocurrent I_{PC} is proportional to the temperature gradient, which in turn is proportional to the near-field intensity at the tip apex [166]. By employing this kind of near-field detector, the direct detection of the tips' near field offers the advantage that only the tip illumination needs to be adjusted. There is no need for a detection beam path as in s-SNOM experiments, which typically comprises an interferometer [24] that requires not only accurate adjustment of the collection and detector optics, but also of the beam quality and wavefronts. This significant reduction of adjustment steps enables a more reliable and accurate comparison of the near-field enhancement at the apex of different tips.

4.3.2 Test of mechanical properties and THz nano-focusing capabilities

We first demonstrate that the antenna probes allow for stable AFM imaging and nanoscale THz focusing. To that end, we recorded a topography image (Fig. 4.4 b) of the detector device (using the 78 μm long antenna probe),

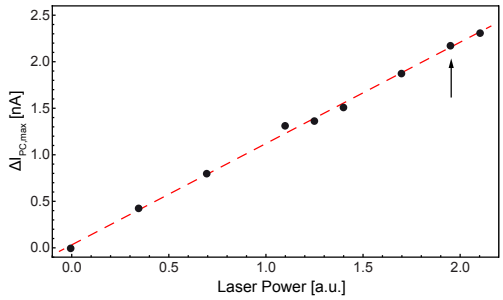

Figure 4.5: **Linear dependence of the photocurrent I_{PC} on the THz laser illumination power.** The black dots are measured data points and the red dashed line is a linear least-squares fit to the data. The arrow marks the power applied in the experiment.

showing the top surface (hBN layer) of the detector above the active region, as well as the lateral Au contacts (left and right) that collect the photocurrent. It clearly verifies a stable AFM operation using our THz antenna probes, despite their comparably large size and hence mass (60 pg $>$ 80 times the mass of standard Si tip), which reduces the mechanical cantilever resonance frequency by nearly a factor two (from 252 kHz for the cantilever with standard Si tip to 139 kHz). To demonstrate the THz nano-focusing functionality of the antenna probe, we recorded a DC photocurrent image $I_{PC,DC}$ (Fig. 4.4 c) simultaneously to the topography. We see a bright vertical stripe of strong photocurrent $I_{PC,DC}$ in the image center, which reveals the strong photo-thermoelectric current generation near the pn-junction. The stripe has a width of 0.6 μm (full width half maximum), which verifies that the THz radiation can be focused by the tip to a deeply subwavelength scale spot. Further, we observe a strong photocurrent $I_{PC,DC}$ close to the lateral source and drain contacts. It arises from a less-defined local doping of the graphene near the contacts [167, 168]. The photocurrent abruptly drops to a constant background value (see discussion in following paragraph) at the graphene edge (marked by the white dashed line in Fig. 4.4 c) and at the metal contacts. From the signal change at the contact we estimate spatial resolution (i.e., lateral field confinement at the tip apex) of about 100 nm ($\lambda/1000$), verifying the conversion of incoming THz radiation into a highly confined nano-focus at the tip apex, and hence the functionality of our tips as high-resolution THz near-field probes.

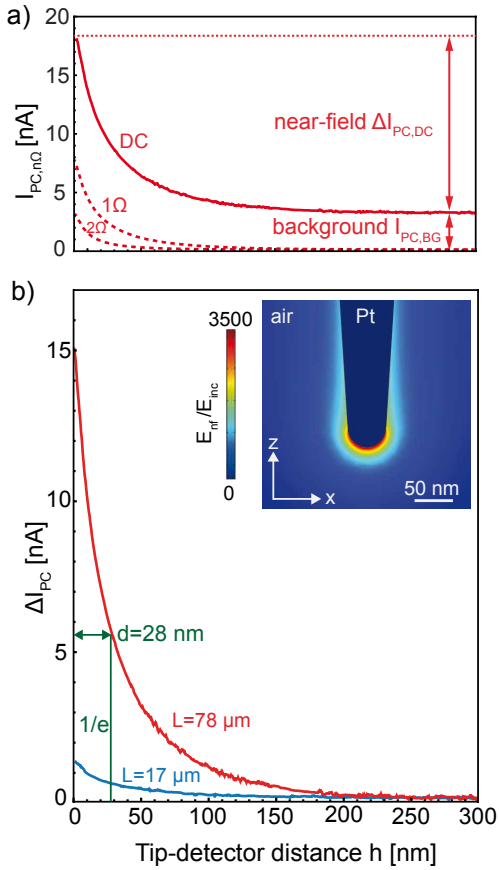

Figure 4.6: **Photocurrent as a function of tip-detector distance.** a) DC photocurrent, $I_{PC,DC}$, and demodulated photocurrent, $I_{PC,1\Omega}$ and $I_{PC,2\Omega}$. b) DC photocurrent after background subtraction $\Delta I_{PC} = I_{PC,DC} - I_{PC,BG}$, for tips of lengths $L = 78\ \mu m$ (red) and $17\ \mu m$ (blue). The inset shows the numerically calculated electric near-field distribution around the apex of a $78\ \mu m$ long antenna tip.

For quantifying the vertical field confinement, we recorded the photocurrent $I_{PC,DC}$ as a function of distance h between tip and detector (solid red curve in Fig. 4.6 a) at the position marked by a black cross in Fig. 4.4 d. The photocurrent $I_{PC,DC}$ decays rapidly with increasing h. For large h it approaches asymptotically the constant value of 3.3 nA, which we assign to a background photocurrent $I_{PC,BG}$ that is generated by the diffraction-limited illumination of

the whole device. Knowing $I_{PC,BG}$, we can extract the near-field contribution $\Delta I_{PC} = I_{PC,DC} - I_{PC,BG}$ to determine vertical confinement (1/e decay length d) of the THz near field (Fig. 4.6 b). We measure $d = 28$ nm, revealing a deep subwavelength-scale vertical field confinement at the tip apex (amounting to about $\lambda/3500$), which agrees well with the numerically calculated near-field distribution at the tip apex (50 nm diameter) of a 78 μm long Pt tip (inset of Fig. 4.6 b).

Interestingly, the background contribution ($I_{PC,BG} = 3.3$ nA) is remarkably small compared to the near-field signal, $\Delta I_{PC} = 15.1$ nA, which typically is not the case in scattering-type and tip-enhanced near-field techniques. We explain this finding by the small active area of the THz detector, which is significantly smaller than the THz focus illuminating the tip. The small but non-negligible background signal can be fully suppressed by demodulating the detector signal at harmonics $n\Omega$ of the tip oscillation frequency Ω (similar to s-SNOM and infrared photocurrent nanoscopy [37, 116, 166]), yielding the signal $I_{PC,n\Omega}$. Recording $I_{PC,n\Omega}$ as a function of tip-detector distance h for $n = 1$ and 2 (dashed red curves in Fig. 4.6 a) indeed shows that the demodulated photocurrent signal completely vanishes for large tip-detector distances h. Due to the "virtual tip-sharpening" effect by higher harmonic signal demodulation [41, 169], we measure a decreasing 1/e decay length of $d_1 = 17$ nm ($\lambda/5600$) and $d_2 = 9$ nm ($\lambda/10500$) for $n = 1$ and $n = 2$, respectively. The demodulation also allows for background-free photocurrent nano-imaging, as demonstrated in Fig. 4.4 d (demodulation at $n = 1$), where the photocurrent drops to $I_{PC,n\Omega} = 0$ nA on the lateral Au contacts and on the SiO_2 substrate (white areas in Fig. 4.4 d).

4.3.3 Verification of antenna resonances

Having verified a proper AFM operation and THz nano-focusing capability of the FIB-fabricated tips, we compare in the following the near-field intensity at the apex of differently long tips. In Fig. 4.6b we compare $\Delta I_{PC,DC}$ as a function of tip-detector distance h for a 78 μm and a 17 μm long tip. The measurements were taken at the same position on the photodetector, marked by a black cross in Fig. 4.4d (5.5 μm from the device edge along the pn-junction). While the background signal $\Delta I_{PC,DC}$ at large distances h is comparable for both tips, we observe at contact ($h = 0$ nm) a significantly

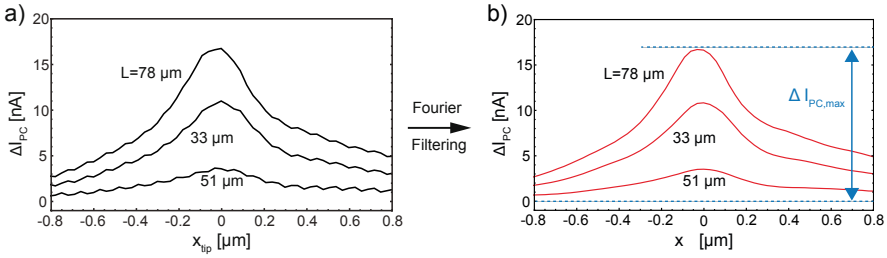

Figure 4.7: **DC photocurrent line profiles.** a,b) Photocurrent ΔI_{PC} line profiles taken along the dashed line in Fig. 4.4d using 33 μm, 51 μm, and 78 μm long antenna tips as recorded (a) and after Fourier filtering (b).

enhanced photocurrent for the 78 μm long tip. For more detailed insights into the dependence of the near-field intensity enhancement on the tip length, we performed photocurrent measurements with six differently long tips. To that end, we recorded line profiles of ΔI_{PC} (average of 100, marked in Fig. 4.4 e by dashed black horizontal line) across the pn-junction. The recording of line profiles, rather than approach curves, offers the advantage that measurement errors due to uncertainties in tip positioning can be minimized. Note that we did not analyze the background-free demodulated photocurrent signals $I_{PC,n\Omega}$, since they do not reveal the near-field intensity but the vertical gradients of the near-field intensity. In Fig. 4.7 a we plot three line profiles showing the near-field photocurrent ΔI_{PC} obtained with tips of length $L = 17$ μm, 33 μm, and 78 μm. During the measurement of the DC approach curves (Figure 4.6) and the line profiles (Figure 4.8a), a periodic noise of 50 Hz could not fully be eliminated. To filter the data, we used Fourier analysis, where first the respective data set was Fourier transformed. In the Fourier domain, we identified the frequency, f_0, corresponding to 50 Hz and removed the respective data points. The removed data points were replaced by a linear interpolation between the two adjacent points. Finally, the inverse Fourier transformation of the resulting data set yields the presented DC approach curves (Figure 4.6b) and line profiles (Figure 4.7 b).

All three photocurrent ΔI_{PC} line profiles in Fig. 4.7 exhibit a maximum near-field photocurrent $\Delta I_{PC,max}$ at the position of the pn-junction (x = 0 nm), and decay to either side towards the source and drain contacts. As seen

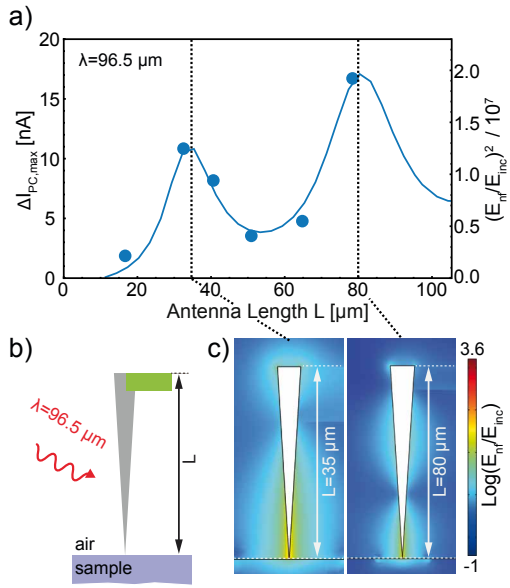

Figure 4.8: **THz nano-focusing as a function of tip length.** a) Maximum photocurrent $\Delta I_{PC,max}$ as a function of antenna length (blue dots) compared to numerical simulation of the near-field intensity enhancement at the tip apex (blue solid line). The vertical axes of the numerical simulation was manually adjusted such that best agreement to the experimental data points was obtained. b) Sketch of numerically simulated geometry (see more details in schematics C in Fig. 4.6a) showing the tip (gray), the silicon cantilever (green), and the detector device (purple). c) Electric near-field distribution (logarithm of the electric field enhancement) of $L = 35\ \mu m$ and 80 μm long tips, showing the first and second fundamental antenna resonance.

before in Fig. 4.6c, we find a strong variation of the near-field photocurrent for the different tips. Plotting $\Delta I_{PC,max}$ as a function of antenna length L for the six different tips (blue dots in Fig. 4.8a), we find that $\Delta I_{PC,max}$ strongly depends on the tip length L, indicating minima and maxima and thus antenna resonances. The longest antenna probe ($L = 78\ \mu m$) yields the strongest, nearly nine-fold near-field intensity enhancement compared to the shortest tip ($L = 17\ \mu m$). Note that both the tip length and the tip apex diameter determine the photocurrent signal. A larger tip diameter reduces the lateral

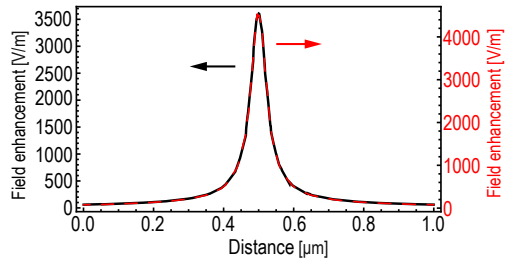

Figure 4.9: Calculated lateral field confinement below the tip apex (50 nm diameter) for length $L = 35\ \mu m$ and 80 μm. For both tips, the field enhancement is strongest right below the tip apex, and decays for larger lateral distances, while the maximum field enhancement is different for the different tips. However, the lateral field confinement is independent of the tips length for constant apex diameter (50 nm).

field confinement below the tip, thus illuminating the detector on a larger area, while the field enhancement is reduced. For a constant tip diameter, it can be shown that a variation of the tip length only varies the field enhancement but not the field confinement, as can be seen in Fig. 4.9. Fig. 4.9 shows the calculated horizontal (along the x-axis right below the tip) line profile of the field enhancement for tips with length $L = 35\ \mu m$ and 80 μm. For both tips, the field enhancement is strongest right below the tip apex, and decays for larger lateral distances, while the maximum field enhancement is different for the different tips (3600 for $L = 35\ \mu m$ and 4700 for $L = 80\ \mu m$). However, the lateral field confinement is independent of the tips length for constant apex diameter of 50 nm. Hence, we can isolate the effect of the antenna length (field enhancement) on the photocurrent by adjusting the apex diameter of each tip to the same value. For the presented experiments, we fabricated all tips with a diameter of 50 nm, which was highly reproducible with an accuracy of ± 3 nm.

To elucidate the variations of the near-field enhancement for different tips, we performed numerical full-wave simulations of THz-illuminated tips with a geometry as depicted in Fig. 4.8b (for more detail see schematics C in Fig. 4.10a). The numerical simulations were done using the commercial software Comsol (Stockholm, Sweden) based on finite element methods in the frequency

domain. In all simulations, the conical tip had an apex radius $R = 20$ nm and a ratio length/width = 8, which in good approximation represents the experimentally fabricated tips. For the metal we used a dielectric permittivity of Pt $\epsilon_{Pt} = -5000 + i * 12000$ resulting from a Drude model fit in reference [170]. The part of the cantilever to which the tips were attached was simulated as a piece of silicon of 6 μm thickness (obtained from SEM image) and 5 μm length and width, and its length and width were chosen to obtain convergence of the numerical simulations. The tip was illuminated by a plane wave E_{in} with wavelength $\lambda = 96.5$ μm (3.11 THz) at an angle of 60° relative to the tip axis, with the sample placed 20 nm beneath it, while the electric field enhancement E_{nf} was calculated 10 nm below the tip apex. The graphene was simulated as a conductive 2D layer with a Fermi energy $E_F = \nu_F * \hbar * \sqrt{|n| * \pi} \approx 500$ meV, a relaxation time $\tau = \frac{\mu E_F}{\nu_F^2} \approx 1.2$ ps, with Fermi velocity $\nu_F = 10^8$ cm s^{-1}, and carrier sheet density $n = 6.57 * 10^{12}$ cm^{-2}. We assumed high quality graphene with a mobility of $\mu = 40000$ cm^2/V*s [171]. The gate voltages were converted to carrier sheet densities via $n_{L,R} = (0.73{*}10^{16} m^{-2} V^{-1}(V_{L,R} - V_{CNP}))$. $V_{CNP} = 0.15$ V is the gate voltage at the charge neutrality point (CNP), which was determined by examining the gate dependence of the device. The coefficient $0.73 * 10^{16}$ was calculated as the static capacitance of the 27 nm thick hBN bottom layer with dielectric constant 3.56 [172].

The blue curve in Figure 4.8a shows the calculated near-field intensity enhancement $f = \left(\frac{E_{nf}}{E_{in}}\right)^2$ between tip and hBN surface (10 nm below the tip). An excellent agreement with the experimentally measured near-field photocurrent (blue dots) is observed. Particularly, the calculation exhibits the maxima at tip lengths of about $L_{res,1} = 34$ μm and $L_{res,2} = 81$ μm. The logarithm of the near-field distributions shown in Fig. 4.8c let us identify the maxima as first and second order antenna resonance, respectively. The latter is excited because of retardation along the tip axis, caused by the inclined illumination relative to the tip axis [173]. The two resonances yield an impressive field intensity enhancement of about 1.2×10^7 and 2×10^7. Most important, the resonant tips increase the field intensity enhancement by about one order of magnitude compared to the 17 μm long tip, which length is that of standard AFM tips.

Compared to classical dipolar radio wave antennas [173] - where $L_{res,n} = n\lambda/2$ with n being the resonance order - we find that (i) the antenna tip's

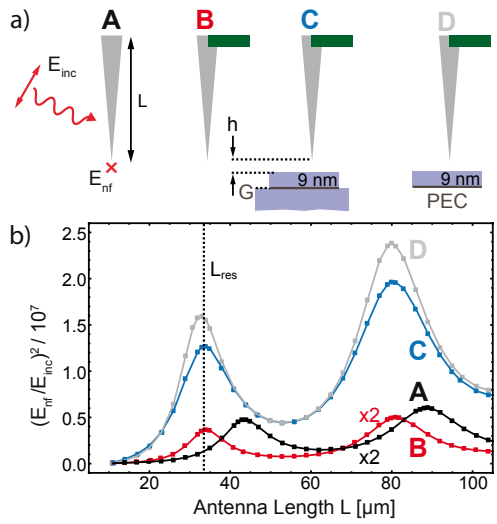

Figure 4.10: **Simulation of the THz near-field enhancement.** a) Antenna geometries considered in the simulation. A, conical antenna tip; B, antenna tip with Si cantilever; C, as in panel B but with detector device below (9 nm hBN-graphene-bulk hBN) tip apex; D, as in panel C, replacing graphene with a PEC. b) Near-field intensity enhancement as a function of tip length, for geometries A-D depicted in panel a.

resonances occur at shorter lengths, and (ii) their resonance lengths do not scale linearly with n (we measure $L_{res,1} = \lambda/2.82$ and $L_{res,2} = \lambda/1.19$). These deviations may be explained by resonance shifts caused by the presence of the cantilever or photodetector. To understand the resonance shifts and to establish future design rules for resonant THz probes, we performed simulations considering a systematic variation of the tip?s environment. First, we calculated the near-field intensity enhancement 10 nm below the apex of an isolated antenna tip (illustrated by sketch A in 4.10a) as a function of the tip length (black curve, Fig. 4.10b). In good agreement with classical antenna theory [173] ($L_{res,n} = n\lambda/2$), we find the first two antenna resonances at $L_{res,1} = 44\ \mu m = \lambda/2.19$ and $L_{res,2} = 89\ \mu m = \lambda/1.08$. The small deviation from $L_{res,n} = n\lambda/2$ we explain by the conical shape of the tip [173]. By adding a silicon cantilever to the tip shaft (sketch B in Fig. 4.10a), the resonance length of the calculated spectrum (red curve in Fig. 4.10b) shift to

$L_{res,1} = 34\ \mu m = \lambda/2.8$ and $L_{res,2} = 81\ \mu m = \lambda/1.2$, while the peak height is reduced by about 27 and 17 percent, respectively. Both observations can be explained by a capacitive loading of the tip antenna by the Si cantilever [173]. Next, the sample (detector device) is considered in the simulations (sketch C in Fig. 4.10a). It is placed 20 nm below the tip apex, and the field enhancement is measured 10 nm below the tip. The calculated spectrum is shown by the blue curve in Fig. 4.10b. Compared to geometry B (red curved in Fig. 4.10b), the near-field intensities at the resonance lengths $L_{res,1}$ and $L_{res,2}$ are significantly enhanced by a factor of about seven. This enhancement can be explained by the near-field coupling between tip and sample. Interestingly, the near-field coupling does not further shift the antenna resonance, which typically occurs at visible and infrared frequencies when an antenna is brought in close proximity to a dielectric or metallic sample [11].

To better understand the absence of resonance shifts due to tip-detector coupling, we first studied the role of the graphene in the near-field coupling. We repeated the numerical calculation, but replaced the graphene with a perfect electric conductor (PEC) (geometry D in Fig. 4.10a). Although the PEC layer perfectly screens the near fields at the tip apex, the antenna spectrum (gray curve, Fig. 4.10b) shows only a minor increase of the peak heights of about twenty percent, and a minor resonance length shift ($L_{res,1} = 33.5\ \mu m = \lambda/2.9$ and $L_{res,2} = 80.5\ \mu m = \lambda/1.2$) compared to geometry C (blue curve, Fig. 4.10b). The results imply that graphene at THz frequencies acts as a nearly metallic reflector for the tip's near fields. This can be explained by the convergence of the Fresnel reflection coefficient toward one for the large wavevectors associated with the near fields at the tip apex [174]. Consequently, a strong near-field coupling between tip and graphene occurs, leading to a strongly enhanced field at the tip apex. In this regard, the nearly negligible spectral shift of the antenna resonance may be even more surprising.

4.3.4 Classical RF antenna theory model

We explain the negligible sample-induced spectral shift of the antenna resonance with the help of radio frequency (RF) theory [173]. In the RF range, circuit theory is an essential tool for the efficient design of antennas and has recently been adopted for the visible and infrared spectral range [175–177]. We consider the tip above the sample as an antenna arm (for simplicity a thin

metal rod) above a metallic ground plane. A sketch and the corresponding circuit model are shown in Figs. 4.11a and b. The antenna arm is described by its intrinsic (dipole) impedance, $Z_A = R_A + iX_A$, where R_A and X_A are the dipole's resistance and reactance, respectively (see Fig. 4.11d) [173]. The antenna impedance $Z_A = R_A + iX_A$ was calculated using standard equations from RF antenna theory [173], with antenna resistance R_A (neglecting ohmic losses) and reactance X_A, which are given by

$$\begin{aligned} R_A &= \frac{1}{2}\frac{\eta}{2\pi \sin(\frac{kl}{2})^2}\Big\{C + ln(kl) - C_i(kl) + \\ &\quad + \frac{1}{2}\sin(kl)\big[S_i(2kl) - 2S_i(kl)\big] + \\ &\quad + \frac{1}{2}\cos(kl)\big[C + ln(\frac{kl}{2}) + C_i(2kl) - 2C_i(kl)\big]\Big\} \end{aligned} \tag{4.1}$$

and

$$\begin{aligned} X_A &= \frac{1}{2}\frac{\eta}{4\pi \sin(\frac{kl}{2})^2}\Big\{2S_i(kl)\cos(kl)\big[2S_i(kl) - S_i(2kl)\big] - \\ &\quad - \sin(kl)\big[2C_i(kl) - C_i(2kl) - C_i(\frac{kD^2}{2l})\big]\Big\}. \end{aligned} \tag{4.2}$$

$C = 0.5772$ is the Euler constant, k the wave vector of the electromagnetic wave, l the antenna length, D the antenna diameter, η the impedance of the surrounding medium (for free space $\eta = 377\ \Omega$) and S_i and C_i are the sine and cosine integrals given by $S_i(z) = \int_z^\infty \frac{\sin(t)}{t}dt$ and $C_i(z) = \int_z^\infty \frac{\cos(t)}{t}dt$. The air gap between tip and sample can be considered as a capacitive load with impedance given by [176]

$$Z_{gap} = R_{gap} + iX_{gap} = -\frac{ih}{\omega\varepsilon D^2} \tag{4.3}$$

with gap height h, THz frequency ω, the dielectric permittivity of the gap filling medium $\varepsilon = 1$ and the diameter of both the antenna arm and the gap D. Because of the open circuit operation of our antenna (the antenna is connected to neither a source nor a receiver), the input impedance $Z_{in} = R_{in} + iX_{in}$ of the antenna can be considered as a serial combination of the two impedances Z_A and Z_{gap}, which is illustrated in Fig. 4.11a and b [121, 175, 177]. In this circuit model, a resonance occurs for $X_{in} = 0$ [176, 178], that is, when the

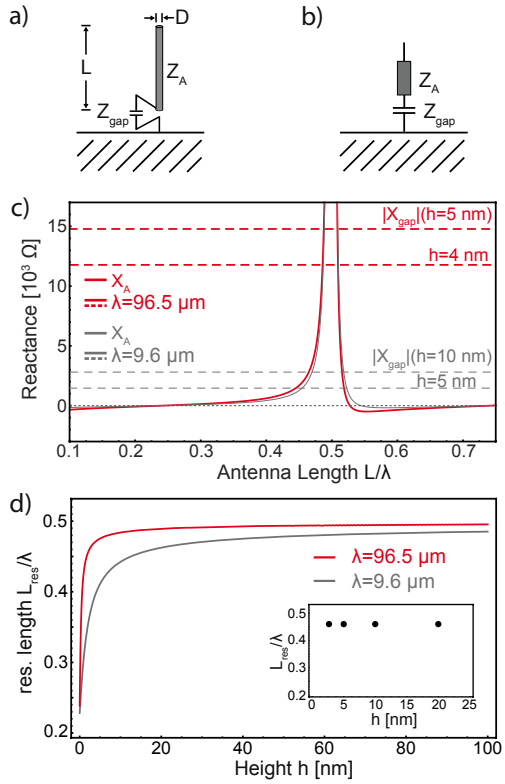

Figure 4.11: a, b) RF circuit model of a linear wire antenna above ground with input impedance Z_{in}, antenna impedance Z_A, and gap impedance Z_{gap}. c) Calculated antenna reactance, X_A (solid lines), and gap reactance, X_{gap} (dashed lines), as a function of antenna length L for wavelength $\lambda = 96.5\ \mu m$ (red) and $\lambda = 9.6\ \mu m$ (black). d) Calculated antenna resonance length, L_{res}, normalized to the excitation wavelength, λ, as a function of gap height h. The inset shows a numerical calculation of the resonance length, L_{res}, for a THz antenna tip above a PEC surface.

capacitive reactance of the load cancels the intrinsic inductive reactance of the antenna, $-X_{gap} = X_A$.

To understand the antenna resonance, we discuss X_A and X_{gap} as a function of the antenna arm length L. The red curve in Fig. 4.11c shows X_A for an illumination wavelength $\lambda = 96.5\ \mu m$. It was calculated according to eq. (4.2) from reference [173], assuming a metal rod of diameter $D = 50$ nm

(corresponding to the tip apex diameter). We find $X_A = 0$ for $L \approx \lambda/4$, which represents the first closed circuit resonance of a classical RF antenna comprising a metal rod (of length L) on a ground plane, not considering the air gap yet. At $L \approx \lambda/2$ we find that X_A diverges, indicating the first open circuit (scattering) resonance [176]. To see how the antenna resonance depends on the capacitive coupling across the air gap, we plot the capacitive reactance $|X_{gap}|$ for gap heights of $h = 4$ nm and 5 nm (horizontal dashed red lines in Fig. 4.11c). We observe that $|X_{gap}|$ decreases with decreasing gap height (i.e., the gap capacitance increases) and the intersection between X_A and $|X_{gap}|$ (resonance condition) shifts the antenna resonance length L_{res} from $\lambda/2$ towards $\lambda/4$ for further decreasing gap width (see also Fig. 4.11d). Interestingly, the resonance length $L_{res} \approx \lambda/2$ barely shifts until gap heights as small as 5 nm are reached. Obviously, the capacitance of an air gap larger than 5 nm is negligibly small and thus yields a large capacitive reactance that is comparable to the inductive reactance of the antenna close to its open circuit resonance.

We show in Figure 4.11d the antenna resonance length L_{res} as a function of the gap width h (red curve). For $h > 5$ nm we find that L_{res} is nearly constant and only slightly smaller than $\lambda/2$. Only in close proximity to the substrate ($h < 5$ nm) the resonance length rapidly decreases. For comparison, we numerically calculated the antenna resonance length of a metal tip above a perfectly conducting ground plane. The result (inset Fig. 4.11d) confirms that the antenna resonance of a tip does not shift for tip-detector distances larger than 5 nm, although the antenna resonance length ($L_{res} = 44\ \mu m = \lambda/2.19$) is slightly smaller than that obtained by antenna theory. This can be attributed to the conical shape of the tip, which is not considered in the antenna circuit model. Based on these theoretical results we can explain the absence of resonance shifts in our experiments and the numerical simulations shown in Figs. 4.8 and 4.10 by the relatively large average distance $h = 30$ nm between tip and graphene. We conclude that in future design of THz resonant probes and interpretation of results one needs to consider the possibility of resonance shifts only for very small tip-detector distances depending on tip radius.

We finally we discuss the results in the wider context of optical antennas. We used the antenna circuit model to calculate the resonance shifts for a mid-infrared illumination wavelength ($\lambda = 9.6\ \mu m$; gray curve in Fig. 4.11d).

For the same antenna diameter D, we observe that a significant shift of the resonance length L_{res} occurs already at much larger gap width h. This can be attributed to the decreasing capacitive gap reactance X_{gap} when the frequency is increased (compare Eq. 4.3), while the inductive antenna reactance X_A barely changes (compare grey and red curves in Fig. 4.11c). We note that our calculations do not consider plasmonic effects, which at higher frequencies cause further resonance shifts, although not being the root cause for them.

4.4 Summary and conclusion

In summary, we have demonstrated the FIB fabrication of sharp, several tens of micrometer long THz antenna tips on standard AFM cantilevers. To evaluate their performance, we applied a graphene-based THz detector to measure the relative near-field intensity directly at the tip apex. The tips were found to support strong antenna resonances, in excellent agreement with numerical calculations. At resonance, the tips provide a nine-fold near-field intensity enhancement at the tip apex as compared to tips of a length that is typical in AFM, while the numerical simulations predict resonant near-field intensity enhancement factors of up to 10^7 relative to the incident field. Our nanoscale THz-resonant near-field probes promise exiting future applications, including scattering-type THz near-field microscopy with enhanced sensitivity, nanoscale nonlinear THz imaging or nanoscale control and manipulation of matter using ultra-strong and ultrashort THz pulses [141, 179–182]. We envision even stronger field enhancement by further reducing the tip apex diameter form currently 50 nm to well below 10 nm.

5 Understanding the image contrast of material boundaries in IR nanoscopy reaching 5 nm spatial resolution

In s-SNOM, a quantitatively accurate understanding of image contrast formation at materials boundaries, and thus spatial resolution is a surprisingly unexplored terrain. In this chapter we introduce the write/read head of a commercial hard disk drive (HDD) as a most suitable test sample for fundamental studies, given its well-defined sharp material boundaries perpendicular to its ultra-smooth surface. We obtain unprecedented and unexpected insights into the s-SNOM image formation process, free of topography-induced contrasts that often mask and artificially modify the pure near-field optical contrast. Across metal-dielectric boundaries, we observe non-point-symmetric line profiles for both IR and THz illumination, which are fully corroborated by numerical simulations. We explain our findings by a sample-dependent confinement and screening of the near fields at the tip apex, which will be of crucial importance for an accurate understanding and proper interpretation of high-resolution s-SNOM images of nano-composite materials. We also demonstrate that with ultra-sharp tungsten tips the apparent width (and thus resolution) of sharp material boundaries can be reduced to about 5 nm.

5.1 Introduction

Scattering-type scanning Near-field Optical Microscopy (s-SNOM) [24] is a scanning probe technique for visible, infrared, and terahertz imaging and spectroscopy with nanoscale spatial resolution. It has proven large application potential ranging from materials characterization [47, 183] to biosciences [41, 45]. In s-SNOM, a full-metal or metal-coated Atomic Force Microscope (AFM) tip is illuminated with p-polarized light. The tip acts as an antenna and concentrates the illumination at its apex to a near-field spot on the scale of the apex

radius. When brought into close proximity to a sample, the near fields interact with the sample and modify the tip-scattered field [112]. By recording the tip-scattered field while scanning the sample, a near-field image is obtained. It is generally accepted that essentially the tip's apex radius determines the achievable resolution, which is typically in the range of a few tens of nanometers [28, 184]. Although the resolution is a key parameter in s-SNOM - as in any other microscopy technique - it has been barely studied in detail experimentally.

The spatial resolution in microscopy is often evaluated by measuring the width of a typically point-symmetric line profile across the sharp boundary between two different materials [185–187]. Such line profiles can be considered as the so-called Edge Response Function (ERF). The characteristic width w of the ERF can be determined via its derivative, which is also known as the Line Spread Function (LSF). The LSF represents the image of a line-like object and is typically a bell-shaped symmetric function centered at the material boundary. The width of the LSF determines according to a specific criterion (e.g. Rayleigh or Sparrow) [2].

In s-SNOM experiments, w (often interpreted as the spatial resolution in analogy to other microscopy techniques) is typically measured directly in a line profile recorded across the boundary [30, 37, 113, 154] or via its derivative [188]. Values as small as $w = 10$ to 40 nm (evaluated using different criteria) have been reported for a broad spectral range extending from visible to terahertz frequencies [30, 113, 189]. However, the boundary between two different materials typically exhibits a step in topography, which challenges the reliable evaluation of w due to tip-sample convolution, [27, 190–192], potentially resulting in a large over- or underestimation. To tackle this problem, a sample with a well-defined sharp material boundary but without topographic features is highly desired [190, 191].

In this chapter we introduce the read/write head of a hard disk drive (HDD) as a truly topography-free resolution test sample, exhibiting nanoscale-defined metal-dielectric boundaries perpendicular to its ultra-smooth surface. It serves as an analogue to the knife-edge test target [186, 187] in classical optical microscopy and allows for detailed analysis of the s-SNOM image contrast with metal tips of apex radii down to 3 nm. We demonstrate that with these tips the ERF width (evaluated as full width half maximum of the corresponding

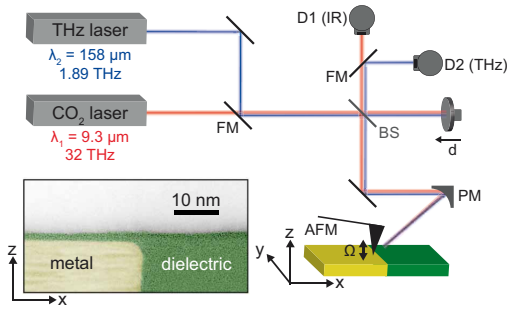

Figure 5.1: **Schematics of the THz and IR s-SNOM setup.** AFM, atomic force microscope; FM, flip mirror; BS, beam splitter; PM, parabolic mirror; D1, IR detector; D2, THz detector. The inset shows a STEM image of a cross section of our sample, which consists of the edge of a magnetic shield structure in a read/write of a HDD head.

LSF) w can be smaller than 5 nm. We further find, surprisingly, that the derivative of the ERF in s-SNOM is generally an asymmetric function. Its width depends on the side of the material boundary where it is evaluated. On the metal side, we find an unexpectedly short near-field probing range that can be one order of magnitude below the tip apex diameter, which we explain by screening of the tip's near field by a metal sample. We corroborate our results by numerical simulations and discuss the implications of our findings for the interpretation of s-SNOM images in general.

5.2 Experimental setup and sample

Figure 5.1 shows the experimental setup and the HDD read/write-head sample. For measurements we utilized a commercial s-SNOM (Neaspec GmbH) as described in section 3.4. The tip was illuminated by either a CO_2 ($\lambda_1 = 9.3\ \mu$m) or a THz ($\lambda_2 = 158\ \mu$m) laser beam with the polarization plane parallel to the tips axis. The tip acts as an antenna and concentrates the incoming radiation at the tip apex. In close proximity to a sample, the near fields interact with a sample and modify the tip-scattered field. The tip-scattered light is recorded by detector D1 (IR) or D2 (THz), and contains information about the local optical properties of the sample. An interferometric detection scheme, operated in synthetic optical holography (SOH) mode [118], enables the recording

of both amplitude s and phase φ images. For background suppression, the tip is oscillated vertically at a frequency Ω and the tip-scattered signal is demodulated at higher harmonics n of the cantilever oscillation frequency Ω, yielding background-free near-field amplitude $s_{nf,n}$ and phase $\varphi_{nf,n}$ images, which will be referred to s_n and φ_n for the scope of this chapter 5.

For evaluating the resolution of the setup employing different tips, we use the read/write head of a commercial HDD as resolution test sample, and more specifically the edge of one of its magnetic shield structures. The lower left inset in Figure 5.1 shows a false color Scanning Transmission Electron Microscopy (STEM) image of a cross section of the sample. The contrast in the image lets us recognize sharply separated areas of metal (marked yellow) and dielectric material (marked green). According to the manufacturer of the HDD [193], the metal is Permalloy (Fe/Ni 20/80), and the dielectric is Al_2O_3. Further, we observe in the STEM image a dielectric capping layer of around 1.5 nm covering the metal, and thus also the material boundary. Most importantly for s-SNOM imaging, the STEM image shows that the sample surface is smooth down to the sub-nm scale, even in the sample area, where the material changes abruptly.

5.3 s-SNOM imaging of resolution test sample

Figure 5.2 shows the s-SNOM imaging results of the material boundary. As near-field probe we employed an 80 μm long Pt/Ir tip (Rocky Mountain Nanotechnology, RM), operated at A = 25 nm tapping amplitude. We used long RM tips rather than standard cantilevered Pt/Ir-coated AFM tips (around 10 μm long) because of their better performance as near-field probes in the THz spectral range [72, 74]. The RM tip radius of r = 23 nm is comparable to the standard metal-coated tips utilized in s-SNOM. We first recorded a topography image of the sample (Fig. 5.2a), from which we extracted a line profile (Fig. 5.2b) along the black dashed line. The line profile shows a maximum topography variation of 4 , which confirms the flatness of the sample. Simultaneously with topography, we recorded IR (32 THz) and THz (1.89 THz) s-SNOM amplitude images from s_2 to s_4. As an example, we show in Fig. 5.2a the IR s_4 image. We observe two regions with high and low near-field amplitude signal, which lets us recognize the metal and dielectric material, respectively [37, 113].

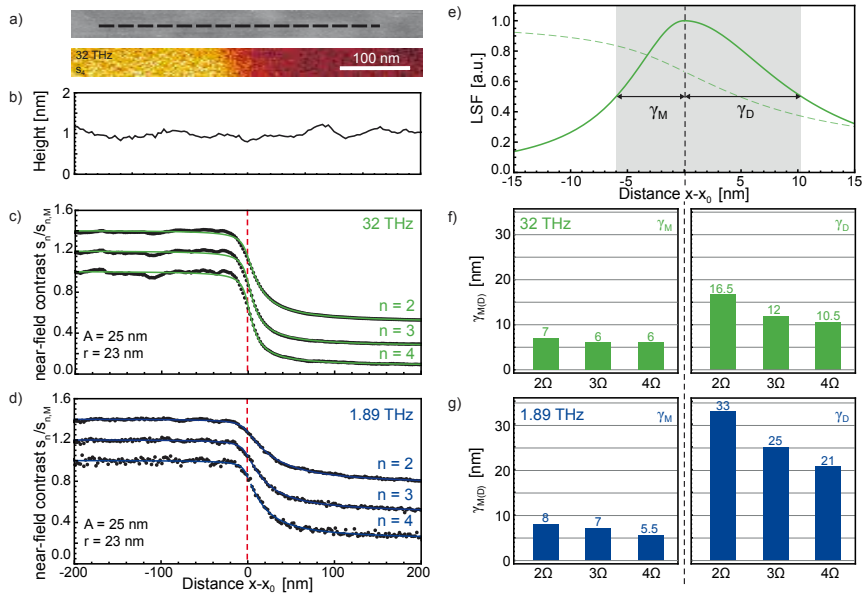

Figure 5.2: **s-SNOM measurements on the resolution test sample.** a) AFM topography and IR s-SNOM amplitude s_4 ($\lambda = 9.3$ μm) images of sample. b) Topography line profile extracted along the dashed line in a). c,d) Measured IR and THz near-field amplitude contrast $s_n/s_{n,M}$ line profiles (average of 20) for harmonics n = 2 to 4 (black dots), and their respective fits using the integral of an asymmetric Lorentzian as described in text (green/blue lines). Tapping amplitude A = 25 nm, tip radius r = 23 nm. The curves are vertically offset for better visibility. e) Derivative (solid line) of the fit of the s_4 line profile (dashed line) taken from panel d). f,g) HWHM $\gamma_{M(D)}$ of the derivatives of line profile fits in c) and d) on the metal and dielectric side, respectively.

To analyze the s-SNOM signal transition across the material boundary, we averaged 20 line profiles for each of the IR and THz images s_2 to s_4. To do this, we first cross-correlated the line profiles for the second demodulation order n = 2 in order to obtain the lateral offset between them. We then corrected for this lateral offset for each demodulation order n = 2 to 4. The second demodulation order was used for finding the offsets because it provides a better signal to noise ratio than higher orders, which enables a higher accuracy of the cross-correlation. The averaging ensures an accurate measurement of

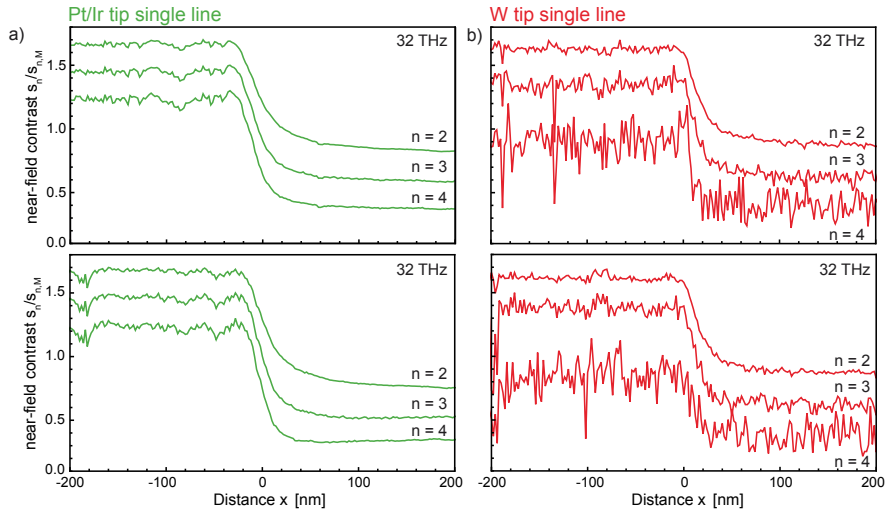

Figure 5.3: **Two different individual s-SNOM amplitude contrast s_n/s_M line profiles before averaging** a) For the Pt/Ir tip and b) the W tip for demodulation orders n=2, 3, 4 at 32 THz and tapping amplitude A=25 nm.

the apparent width of the material boundary, as individual line profiles can exhibit an untypical small or large width due to noise, which is illustrated at two examples in Fig. 5.3. The averaged line profiles (black dots) are shown in Figure 5.2 c and d. In agreement with former observations, we observe that (i) the near-field contrast (i.e. the ratio between the near-field signal on metal and on dielectric material) increases for increasing demodulation orders n [132, 194] and (ii) the contrast is higher for the IR than for THz. The difference between the IR and THz material contrast can be attributed to frequency-dependent dielectric permittivities of the sample. Most important, and not having been recognized in previous s-SNOM experiments, the line profiles in Fig. 5.2c and d are *not* point-symmetric, which we will study and discuss in the following.

The *asymmetric* line profiles require a careful analysis in order to properly interpret the s-SNOM contrast at material boundaries. As a first step towards

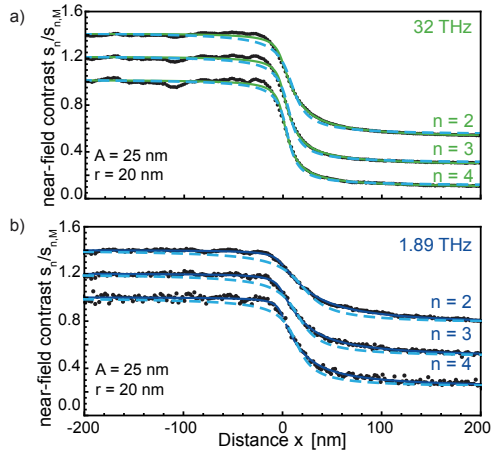

Figure 5.4: **Comparison of symmetric and asymmetric fit** a,b) Measured IR and THz near-field amplitude contrast s_n/s_M line profiles (average of 20) for harmonics n = 2 to 4 (black dots), and their respective fits using the integral of an asymmetric Lorentzian as described in text (green/blue lines). For comparison, the graphs also show a symmetric fit of the data (light blue dashed line). Tapping amplitude A = 25 nm, tip radius r = 23 nm. The curves are vertically offset for better visibility

this goal, we approximate the line profiles by the empirically found fit function:

$$\Theta(x) \quad = \quad \begin{cases} \pi^{-1} f_M \arctan(\frac{x-x_0}{\gamma_M}) + b & \text{for } x < x_0 \\ \pi^{-1} f_D \arctan(\frac{x-x_0}{\gamma_D}) + b & \text{for } x \geq x_0 \end{cases}, \tag{5.1}$$

with fit parameters x_0 (interface position) and b (vertical offset). To account for the asymmetry of the line profiles, the fit parameters $f_{M(D)}$ and $\gamma_{M(D)}$ assume different values for the metal ($x < x_0$) and the dielectric ($x \geq x_0$) sides. Further, the continuity of Θ and its derivative across the material interface are enforced. These fits are shown as green and blue solid curves in Fig. 5.2 c and d, excellently matching the experimental data. Please note that that the agreement between data and *symmetric* fits is much worse, which is shown for comparison in Figure 5.4. This finding corroborates that indeed *asymmetric* fitting is required to correctly analyze the experimental line profiles. We next use these fits to quantify the asymmetry of the line profile. To that end, we

calculate the derivative of the fit function $\Theta(x)$, which is given by a piecewise Lorentzian (exemplarily shown in Fig. 5.2 e for the IR s_4 line profile):

$$L(x)(x) = \begin{cases} \left(\frac{f_M}{2\pi}\right)\left(\frac{\gamma_M}{(x-x_0)^2+(\gamma_M)^2}\right) & \text{for } x < x_0 \\ \left(\frac{f_D}{2\pi}\right)\left(\frac{\gamma_D}{(x-x_0)^2+(\gamma_D)^2}\right) & \text{for } x \geq x_0 \end{cases}, \tag{5.2}$$

with different half width at half maxima (HWHM) $\gamma_{M(D)}$ for the metal and the dielectric sides. Note that in the context of this work, we call this derivative the Line Spread Function (LSF) in analogy to the general concepts of resolution in classical optical microscopy as described in the introduction. The bar diagrams in Figs. 5.2 f and g summarize the different values for γ of the IR and THz measurements for demodulations orders n = 2 to 4. We find that the γ_D are about three to four times larger than the γ_M, quantifying the significant asymmetry of the line profiles. The total material boundary width w, defined as $w = \gamma_M + \gamma_D$, decreases from 23.5 nm to 16.5 nm (IR line profile) and from 41 nm to 26.5 nm (THz line profile) when the demodulation order increases from n = 2 to n = 4 (Fig. 5.2 f,g). The sharpening of the material boundary by higher-harmonic demodulation and the values for w agree well with previous studies [169, 194, 195], which, however, did not recognize the asymmetry of the profiles. Our quantitative analysis further shows that the material boundary is located not exactly central to the signal transition (see further discussion below), which is critical when a precise localization of material boundary form s-SNOM profiles is desired. The analysis also shows that a significant near-field signal tail into one material does not necessarily indicate unidirectional material gradient, for example caused by unidirectional material diffusion. Our results clearly show that asymmetric line profiles with substantial levels of asymmetry can occur at well-defined sharp material boundaries, a fact that seems to be intrinsic to the near-field interaction and probing process. We will elucidate this phenomenon below.

5.4 Ultra-sharp, FIB fabricated tips for 5 nm resolution

To reduce the perceived width w of the material boundary in the s-SNOM line profile, i.e. to increase the spatial resolution, we employed Focused Ion

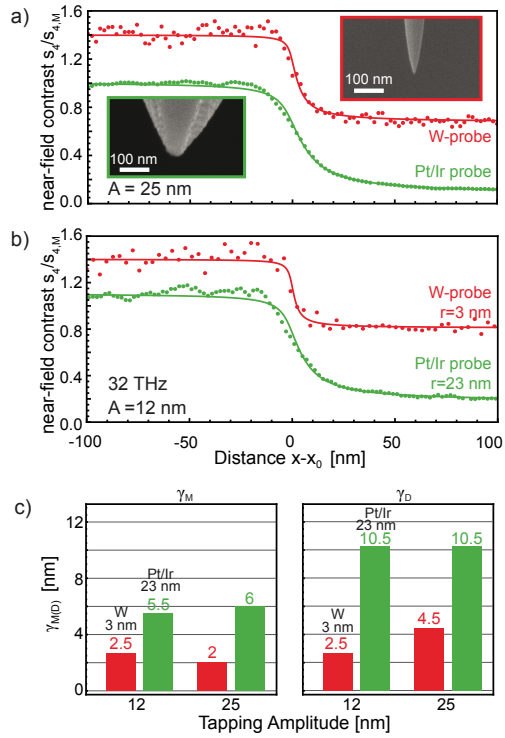

Figure 5.5: **s-SNOM resolution test measurements for different probe sizes at 32 THz.** a) Near-field amplitude contrast $s_4/s_{4,M}$ line profiles recorded with ultra-sharp W tip (r = 3 nm) (red dots) and commercial Pt/Ir tip (r = 23 nm) (green dots, same data as in Fig. 5.2c) at A = 25 nm tapping amplitude. The green and red solid lines show the respective fits on the data. The upper right and lower left inset shows an SEM image of the W-tip and Pt/IR-tip, respectively. The curves are vertically offset for improved representation. b) Near-field amplitude contrast $s_4/s_{4,M}$ line profiles and their respective fits recorded with ultra-sharp W tip (r = 3 nm) (red) and commercial Pt/Ir tip (r = 23 nm) (green) at A = 12 nm tapping amplitude. c) $\gamma_{M(D)}$ evaluated for the line profiles recorded with the W- and Pt/Ir-tips at A = 25 nm and A = 12 nm tapping amplitudes.

Beam (FIB) machining to fabricate Tungsten (W) tips with a reduced tip radius of only r = 3 nm (see upper right SEM image in Fig. 5.5) [74, 162]. The tungsten (W) tips were fabricated by FIB machining using a Helios450s

electron microscope (FEI,Netherlands). We used standard Si atomic force microscopy (AFM) cantilevers and first made a cylindrical grove into the tip. Then, a high aspect ratio cone was milled out of a solid tungsten wire, cut at around 12 μm length, and fitted into the cylindrical grove in the Si cantilever. The cone was attached by FIB induced deposition of silicon oxide. Details of this procedure can be found in chapter 4.2 and reference [74]. Finally, the tip apex was sharpened by circular ion milling along the tip axis, as described in detail in reference [73]. To reach a very small tip apex radius of 3 nm, it is crucial to gradually reduce the milling current down to about 7 pA. Note that fabrication of ultra-sharp tips with radii as small as 3 nm required a hard material such as W. With Pt/Ir we achieved apex radii of about 10 nm and with Au not better than 12 nm. We assign this finding to diffusion of metal atoms under ion bombardment, which is higher for Au than for Pt/Ir and W. Further studies are needed to clarify the mechanisms involved in the tip sharpening process.

Utilizing the ultra-sharp full-metal W probes, we recorded line profiles across the material boundary at 32 THz illumination and a tapping amplitude of A = 25 nm. The red dots in Fig. 5.5 a show the s_4 line profile (average of 50 profiles using the same procedure as described in the previous section 5.3) and the corresponding fit (red curve). For comparison we show the line profile obtained with the Pt/Ir probe (green; same data and fit as in Fig. 5.2 c). By measuring $\gamma_{M(D)}$ for both line profiles (summarized in Fig. 5.5 c), we find that w is reduced by more than a factor of two when the W-tip is used. The improvement, however, is surprisingly small, considering that the tip radius of the W tip is around eight times smaller than that of the Pt/Ir tip. We attribute this finding to the relatively large tapping amplitude of A = 25 nm, which is comparable to the radius of the Pt/Ir tip (r = 23 nm) but much larger than the radius of the W tip (r = 3 nm). According to previous studies [194, 196], the width w can be improved by reducing the tapping amplitude. We thus recorded a line profile using both the Pt/Ir and W tip with a reduced tapping amplitude of A = 12 nm (green and red data in Fig. 5.5 b, respectively). The resulting values for $\gamma_{M(D)}$ are shown in Fig. 5.5 c. For the Pt/Ir tip, we measure w = 16.5 nm, which is comparable to that of the line profile at larger tapping amplitude A = 25. For the W-tip the width w of the material boundary decreases further, to about 5 nm,which clearly demonstrates that

ultra-sharp metal tips can push the s-SNOM resolution well below 10 nm. We note that this reduction is mainly caused by the reduced γ_D of the LSF on the dielectric side of the material boundary. On the metal side, the 1.5 nm-thick dielectric capping layer makes the metal/dielectric boundary a subsurface object (SEM image; Fig. 5.1), for which the resolution is well known to be diminished compared to objects directly at the surface [194, 197]. It also has to be noted that numerous experiments reliably reveal a decrease of the near-field amplitude s_n-signal with decreasing tip diameter, which requires averaging of several line profiles to obtain sufficiently high signal to noise (S/N) ratios. We attribute this behavior to the stronger localization of the near field for sharper tip apices and thus the reduction of the sample volume participating in the near-field interaction with the tip, which is not compensated by the increased field enhancement at sharper tip apices.

5.5 Numerically simulation line profiles

In Figure 5.6 we show results of a numerical study, which aims at corroborating and understanding the asymmetry of the s-SNOM line profiles observed in our experimental study (Figures 5.2 and 5.5). We performed numerical full-wave simulations of the s-SNOM imaging process using the commercial software package Comsol. A conical tip of 8 μm length and apex radius r = 23 nm length is placed above a sample modeled by metallic permittivity of $\epsilon_M = -1200{+}750i$ on the left side ($x < 0$ nm) and a dielectric material of $\epsilon_D = 1.05{+}0.19i$ (Al_2O_3) [198] on the right side ($x > 0$ nm) of the material boundary at $x = 0$ nm (see illustration in Fig. 5.6a). We assume a p-polarized plane wave illumination (electric field E_{in}) at 32 THz at an angle of $\alpha = 60°$ relative to the tip axis, as in our s-SNOM. The tip-scattered electric field E_{sca} is proportional to the complex-valued dipole moment P, calculated numerically according to [199]

$$P = \int \sigma(r) r dr, \tag{5.3}$$

where $\sigma(\mathbf{r})$ is the surface charge density, $\mathbf{r}$ is the radius vector, and the integral is carried out over the whole tip surface. Note that P can be considered as the sum of the tip's dipole moment p_0 arising from the polarization induced by the incoming radiation E_{in} and the induced dipole moment p_{ind} originating

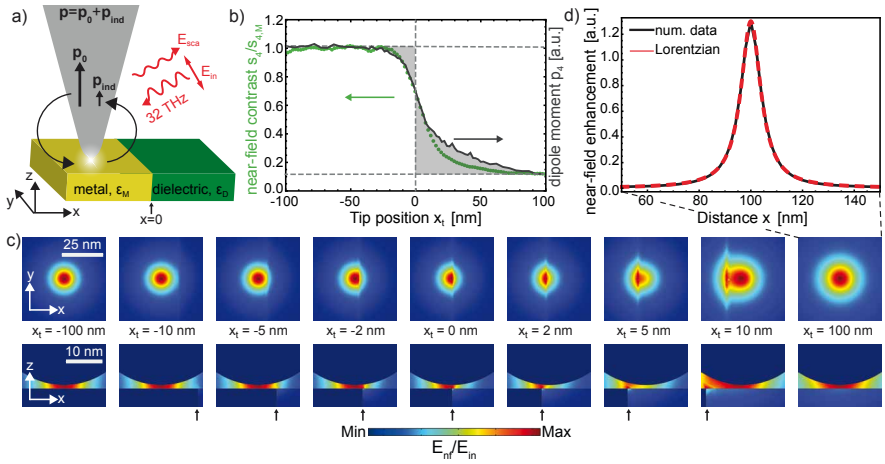

Figure 5.6: **Numerical simulation of IR s-SNOM line profiles.** a) Sketch of the geometry. A tip with apex radius r = 23 nm and length 8 μm is placed above a sample consisting of metal on the left ($x < 0$ nm) and dielectric material on the right ($x > 0$ nm) side. The material boundary is at $x = 0$. b) Simulated (gray curve) and measured (green dots, same data as in Fig. 5.2 s-SNOM amplitude contrast $s_4(x_t)/s_(4,M)(x_t)$ for a tapping amplitude A = 25 nm for different tip positions x_t relative to the material boundary. c) Electric near-field distribution below the tip apex for different tip positions x_t in the xy-plane ($z = 0$ nm) and xz-plane ($y = 0$ nm) for tip-sample separation of 1 nm. The arrow marks the material boundary. d) Profile of the simulated electric near-field distribution along the x-axis when the tip is placed above the dielectric material (black curve) ($x_t = 100$ nm). Fit of a Lorentzian function (red curve) to the simulated near-field profile.

from the tip's near-field interaction with the sample, the latter yielding the s-SNOM signal. To simulate the measured s-SNOM signal we have to take into account that the tip is oscillating, and the detector signal is demodulated at higher harmonics of $n\Omega$. Accordingly, we calculate the scattered field, $E_{sca}(z_t)$, as a function of tip height z_t above the sample. Assuming a vertical sinusoidal motion of the tip with frequency Ω and tapping amplitude A = 24.5 nm, we calculate the time evolution of the detector signal $E_{sca}(z_t(t))$ with $z_t(t) = 0.5 + A/2 \cdot (1 + \cos(\Omega t))$. The n-th Fourier coefficient of $E_{sca}(z_t(t))$ is then the mathematical analogue of the complex-valued s-SNOM signal $s_n e^{i\varphi_n}$.

By calculating s_n as a function of tip position x_t, we obtain the simulated line profile $s_n(x_t)$ across the material boundary. The gray curve in Fig. 5.6b shows the result obtained for demodulation at $n = 4$. For comparison, we also show the experimental line profile $s_4(x)$ (green dots, same data as in Fig. 5.2c). A good match between the simulated and the experimental line profiles is found after normalization of both near-field profiles to their average value on metal. We note that the model over-predicts the asymmetry slightly, essentially on the dielectric side of the material boundary. We explain this observation by differences in tip and sample geometry in experiment and simulations. For example, we simulate a perfect material boundary and a perfect conical metal tip, while in the experiment the sample's material boundary is slightly rounded (see STEM image in Fig. 5.1) and the tip has a more complicated (pyramidal) shape. We did not take into account the more complicated geometry in the simulation due to limited computation power. We further note that no lateral shift in x-direction was applied to the simulated data (Fig. 5.2c) in order to match the experimental data, which confirms the position of the material boundary found by the fitting procedure introduced in Fig. 5.2. Most importantly, the simulation clearly confirms the asymmetry of s-SNOM line profiles across a material boundary.

To explain the asymmetry of the line profiles, we show in Fig. 5.6 d the calculated electric near-field distribution around the tip apex, E_{nf}/E_{in}, for different tip positions x_t. On the metal and dielectric surface, far away from the material boundary at x_t = -100 nm and x_t = 100 nm, respectively, we observe that the near-field distribution in the plane of the sample (xy-plane) is symmetric. However, the near field confinement is markedly different, indicating a larger probing range of the tip on the dielectric side. When the tip approaches the boundary from the dielectric side, the near-field distribution is already significantly modified at $x_t = 10$ nm, revealing a near-field interaction with metal across the material boundary. Subsequently, the tip- scattered field and the s-SNOM amplitude signals s_n increase. On the other hand, when the tip approaches the boundary from the metal side, a significant modification of the near-field distribution requires the tip be closer than 5 nm to the interface ($x_t >$ -5 nm). We explain this finding by the screening of the tip$\tilde{\text{O}}$s near fields by the metal sample, which reduces the probing range and prevents the detection of the material boundary via the tip-scattered field for tip-boundary

distances larger than 5 nm. The absence of strong near-field screening on the dielectric side thus explains the asymmetry of the s-SNOM line profiles across the boundary between metal and dielectric. In the experiment, the near-field screening by the metal is reduced due to the rounded edge of the material interface (see Fig. 5.1), resulting in a reduced asymmetry of the measured line profiles compared to the simulated one (Fig. 5.6b). We expect that the near-field screening is less important for boundaries between two materials with low dielectric contrast, which would make s-SNOM line profiles more symmetric. We finally note the electric near-field distribution below the tip apex can be well approximated by a Lorentzian function (Fig. 5.6d). This observation might explain why the s-SNOM line profiles can be well fitted by the integral of Lorentzian functions, but certainly further studies are required for a more comprehensive understanding. Although the presented results are discussed in the context of s-SNOM, we expect the same effect of screening to occur in images acquired by other AFM-based optical microscopy techniques, such as tip-enhanced photo-thermal expansion microscopy [107] and photo-induced force microscopy [200] that rely on the material profiling via tip-enhanced near fields.

5.6 Summary and conclusion

In summary, we showed that the read/write head of a HDD can serve well as a topography-free test sample for fundamental s-SNOM experiments. It allowed for detailed studies of contrast, resolution, and shape of material boundaries, yielding unprecedented insights into the image contrast formation. Using tips with a standard apex diameter of about 50 nm, we find that the width w of a material boundary in s-SNOM images is around 20 nm, which is in agreement with former reports. However, the line profiles exhibit an asymmetry that has not been observed before, which we corroborate via numerical calculations. The asymmetry can be explained by the tip-sample near-field interaction, which has significant spatial variations across material boundaries. Particularly, we find that the near field at the tip apex is strongly screened on the metal side, which reduces the apparent width of the material boundary in s-SNOM images. We expect that a similar effect will occur at the boundary between two dielectric materials of high and low refractive index because the

screening by polarization charges in high-index dielectrics is nearly as large as in metals. Considering this effect will be of critical importance for avoiding misinterpretation of asymmetric line profiles as, for example, continuous (i.e. not sharp) changes of dielectric properties caused by non-uniform doping, directional diffusion, etc. In the future, it will also be interesting to study how near-field screening affects the spatial resolution when two closely spaced objects are imaged. We further envision that near-field screening could be exploited to increase the s-SNOM resolution for molecule imaging, for example by depositing them on top of a sharp material boundary. We finally note that with custom-made ultra-sharp tips of 3 nm radius we can reduce the apparent material boundary to about 5 nm. On the other hand, both the signal and S/N ratio decrease for sharper tips, which will require to increase the field enhancement at the apex of ultra-sharp tips, for example by engineering and optimizing the antenna performance of the tip shaft.

6 Nanoscale chemical identification of thin films using infrared near-field spectroscopy and standard Fourier transform infrared references

This chapter establishes a solid basis for the interpretation of infrared near-field spectra of thin organic films on highly reflective substrates and provides guidelines for their straightforward comparison to standard far-field Fourier transform infrared (FTIR) spectra. Particularly, the spectral behavior of near-field absorption and near-field phase is studied, both quantities signifying the presence of a molecular resonance. It is demonstrated that the near-field phase spectra only weakly depend on the film thickness and can be used for an approximate comparison with grazing incidence FTIR (GI-FTIR) spectra. In contrast, the near-field absorption spectra can be compared more precisely with far-field spectra: for ultra-thin films they match well GI-FTIR spectra, while for thick films a good agreement with standard transmission FTIR spectra is found. Our results are based on experimental data obtained by nanoscale FTIR (nano-FTIR) spectroscopy and supported by a comprehensive theoretical analysis.

6.1 Introduction

The interferometric detection in s-SNOM nano-imaging and nano-FTIR spectroscopy yields both near-field amplitude s_n and phase φ_n. It has been found that the near-field phase spectra, $\varphi(\omega)$, relate to the absorptive properties of molecular samples [31, 201–203]. However, a quantitative comparison with transmission far-field FTIR spectroscopy [5] reveals that the peak positions do not necessarily coincide [44, 45]. Instead, for thick organic films, the peak positions of FTIR absorbance spectra match well with that of the so-called near-

field or nano-FTIR absorption spectra $a_n(\omega) = s_n(\omega)\sin(\varphi_n(\omega))$ [42, 204, 205]. This finding promises a convenient identification of nano-materials in the mid-IR fingerprint region by simply comparing nano-FTIR absorption spectra with standard FTIR spectra from databases. On the other hand, recent studies indicate that nano-FTIR absorption spectra of thin samples (thickness $d <$ tip apex radius R_t) on highly reflective substrates are blue-shifted, while matching well with grazing-incidence FTIR (GI-FTIR) spectra [45]. In this chapter, we address this issue with an experimental and theoretical study of near- and far-field infrared spectra of thin organic films of varying thickness on highly reflective substrates. We provide basic physical insights and practical guidelines for nanoscale material characterization based on direct comparison of near-field spectra with standard far-field references.

6.2 Sample description and experimental results

As sample we used spin-coated polymer films of Poly(methyl methacrylate) (PMMA) on silicon, as PMMA exhibits well-defined molecular vibrational resonances [42]. As typical in s-SNOM and nano-FTIR, a silicon substrate is used to enhance the near-field signal of the organic film (substrate-enhanced near-field spectroscopy) [129, 206]. The samples were fabricated by Thales V. A. G. de Oliveira at CIC Nanogune, San Sebastián, Spain.

For the experiments, we used a commercial s-SNOM and nano-FTIR setup (*Neaspec GmbH*, model *neaSNOM*, Germany), illustrated in Figure 6.1(a) and described in detail in Chapter 3. A gold-coated standard AFM tip oscillating vertically at frequency Ω =120 kHz was employed as near-field probe. The tip was illuminated by either a tunable quantum cascade laser (QCL, *Daylight Solutions, Inc.*, USA) or a broadband mid-infrared laser continuum [42]. For effective background suppression, the tip-scattered signal was demodulated at higher harmonics $n\Omega$ of the cantilever oscillation frequency, yielding near-field amplitude and phase signals, s_n and φ_n , respectively [24]. Throughout this chapter $n = 3$.

By using the QCL and operating the interferometer in synthetic optical holography (SOH) mode (compare Chapter 3.3.4) [118] two sets of single-wavelength near-field amplitude s_3 and phase φ_3 images (Fig. 6.1d) were

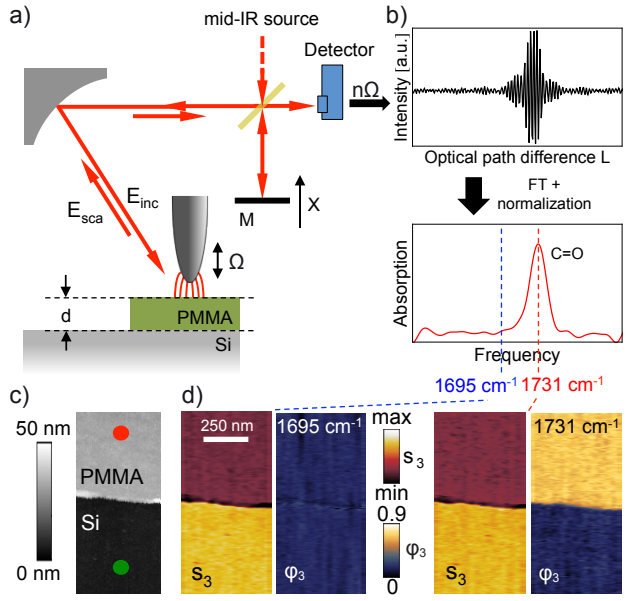

Figure 6.1: Near-field imaging and spectroscopy of thin polymer films. a) s-SNOM and nano-FTIR setup. b) Near-field interferogram and the corresponding near-field absorption spectrum. c) Topography of a 31 nm PMMA film on Si. Red and green dots mark positions where PMMA and reference nano-FTIR spectra were taken. d) Near-field amplitude s_3 and phase φ_3 images at 1695 cm−1 and 1731 cm^{-1}.

recorded simultaneously to topography (Fig. 6.1c). The images recorded on resonance with the C=O stretching bond of the PMMA molecules (1731 cm−1) verify both the nanoscale spatial resolution of the setup and the expected phase contrast (revealing absorption) relative to the non-absorbing silicon substrate [31]. Off-resonance (1695 cm^{-1}), the vanishing phase contrast indicates the absence of molecular absorption.

For nano-FTIR spectroscopy, the reference mirror M in Figure 6.1a is translated at a fixed sample position to acquire an interferogram of the tip-scattered mid-infrared laser continuum (Fig. 6.1 b), as described in Chapter 3.3.5. A complex Fourier transformation yields near-field amplitude $s_{nf,3}(\omega)$ and phase $\varphi_{nf,n}(\omega)$ spectra, as introduced in section 3.3.5. Analogous to far-field FTIR spectroscopy, the nano-FTIR data of the PMMA film are normalized to a non-absorbing reference (here silicon), yielding the complex-

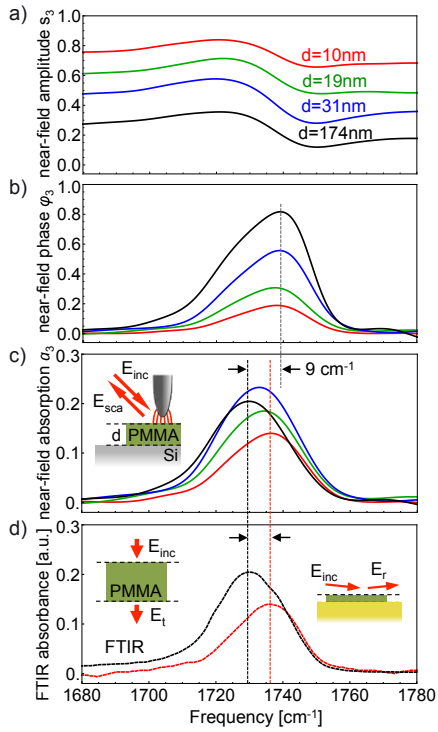

Figure 6.2: **Experimental spectra of PMMA.** a) nano-FTIR amplitude, b) phase, and c) absorption spectra of PMMA films (average of 40 interferograms, 53 min acquisition time per spectrum, 7 cm^{-1} resolution, × 60 zero filling). d) FTIR spectrum of 1 μm thick PMMA on CaF_2 and GI-FTIR spectrum of 10 nm thin PMMA on Au substrate. Vertical black and red lines mark the peak positions.

valued normalized PMMA spectrum (near-field contrast) $\eta_3(\omega) = s_3 e^{i\varphi_3} = (s_{3,PMMA}/s_{3,Si})e^{i(\varphi_{3,PMMA}-\varphi_{3,Si})}$.

Figure 6.2 shows the measured nano-FTIR spectra for PMMA films of different thicknesses d and compares them to far-field FTIR spectra, which were recorded by Roman Krutokhvostov at CIC nanoGUNE. All far-field spectra display the absorbance, that is, $A_t = -log(I_t/I_0)$ for FTIR and $A_r = -log(R/R_0)$ for GI-FTIR spectroscopy. I_t is the power transmitted through the sample, and I_0 is the incident power. R is the power reflected from the film on a substrate, and R_0 is the power reflected at the bare substrate. All near-field amplitude s_3 spectra (Fig. 6.2a) reveal a dispersive behavior around

the C=O resonance, whereas the phase φ_3 spectra (Fig. 6.2b) exhibit an absorption-like peak at 1738 cm^{-1}. Both observations are typical for the spectral near-field response of an organic material [31, 129, 201]. With decreasing film thickness, the amplitude values increase, which can be explained by the enhanced near-field interaction between tip and silicon substrate through the thin polymer film [129, 206, 207]. Simultaneously, the peak height of the phase decreases, which can be attributed to the reduced amount of the probed PMMA [129]. Importantly, we observe that the peak position in all phase spectra is nearly independent of the film thickness, while being blue-shifted by about 3 cm^{-1} compared to the GI-FTIR spectrum (Fig. 6.2d). The peak position of the near-field absorption spectra a_3 (Fig. 6.2c), in contrast, shifts to lower frequencies when the film thickness increases. Interestingly, the peak position of the thick-film near-field absorption spectrum ($d = 174$ nm) matches well the far-field FTIR peak of bulk PMMA (dashed black curve, Fig. 6.2d), while the near-field absorption spectrum of the thinnest film ($d = 10$ nm) matches well the GI-FTIR spectrum (dashed red curve, Fig. 6.2(d)).

6.3 Theory

6.3.1 Transmission and grazing incidence FTIR far-field spectra

To understand the experimental results, we performed a theoretical comparison of far- and near-field spectra based on the film's dielectric permittivity $\varepsilon = \varepsilon' + i\varepsilon''$. The absorbance spectra, A_t, of thick films measured by transmission FTIR spectroscopy yield the absorption coefficient $\kappa = \mathrm{Im}(\sqrt{\varepsilon}) = \mathrm{Im}(\sqrt{\varepsilon' + i\varepsilon''})$ [5, 199], which is the imaginary part of the complex-valued index of refraction $N = n + i\kappa$. The permittivity of a material can be expressed in terms of the refractive index as:

$$\epsilon = N^2 = (n + i\kappa)^2 = n^2 - \kappa^2 + 2in\kappa. \tag{6.1}$$

Using this expression, we can approximate for weak oscillators ($\varepsilon'' < \varepsilon'$ and $\kappa < n$), e.g. molecular vibrational resonances, $|\epsilon| = |n^2 + \kappa^2| \approx n^2$ and $|\epsilon| \approx \epsilon'$,

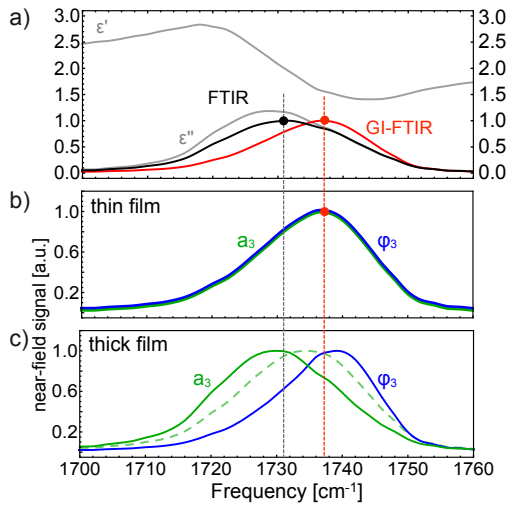

Figure 6.3: **Calculated spectra of PMMA (normalized to peak maximum).** a) Real and imaginary part of the dielectric permittivity of PMMA obtained by infrared ellipsometry (data previously used in [31]) [208] (gray curves). FTIR spectrum (black curve) and GI-FTIR spectrum (red curve) calculated using eqs. (6.2) and (6.9), respectively. b) Nano-FTIR absorption a_3 and phase φ_3 for an ultra-thin film calculated using eq. (6.15). c) Nano-FTIR absorption a_3 (green dashed) and phase φ_3 (blue) for a thick film according to Eqs. (6.17) and (6.18), respectively. Green curve is the calculation using the Finite Dipole Model (FDM) [125], which approximates the tip by an elongated, non-resonant metal spheroid. The employed model parameters are: tapping amplitude $A = 45$ nm, $R_t = 30$ nm, and the semi-major axis of the tip-spheroid $L = 300$ nm.

and obtain for the measured absorbance the expression

$$A_t \propto \frac{1}{2\sqrt{\varepsilon'}}\varepsilon''. \tag{6.2}$$

We find that $\kappa(\omega)$ (black curve, Fig. 6.3a) is slightly blue-shifted compared to $\varepsilon''(\omega)$ (lower gray curve, Fig. 6.3a), owing to the frequency-dependance of $\varepsilon'(\omega)$ (upper gray curve, Fig. 6.3a).

GI-FTIR spectroscopy measures the power reflected at a thin film on a highly reflecting, typically gold covered, substrate. This power R is proportional to

$|r|^2$, with r being the far-field reflection coefficient of the film-substrate system

$$r = \frac{r_{12} + r_{23} exp(2ik_{z,2}d)}{1 + r_{12}r_{23} exp(2ik_{z,2}d)}. \tag{6.3}$$

Here, $r_{ij} = (\varepsilon_j k_{z,i} - \varepsilon_i k_{z,j})/(\varepsilon_j k_{z,i} + \varepsilon_i k_{z,j})$ are the single interface Fresnel reflection coefficients for p-polarized light and $k_{z,i} = (2\pi/\lambda)\sqrt{\varepsilon_i - \sin^2\Theta}$. The indices $i, j = 1, 2, 3$ refer to air, film, and substrate, respectively (see Fig. 6.4), Θ is the angle of incidence and λ is the free-space wavelength. For simplicity, we substitute in the following ε_2 (the film's dielectric function) by ε. For optically thin films with $d \ll \lambda$, eq. (6.3) can be well approximated by the two lowest orders of its Taylor expansion in $k_{z,2}d \ll 1$:

$$r = \frac{r_{12} + r_{23}}{1 + r_{12}r_{23}} + 2ik_{z,2}d\frac{r_{23}(1 - r_{12}^2)}{1 + r_{12}r_{23}} + \mathcal{O}\left(k_{z,2}d\right)^2 \tag{6.4}$$

with the 0th-order term yielding the pure reflection from the substrate r_{13} (i.e., no film) and the 1st order term describing the thickness-dependence [44]. Assuming $r_{23} \approx 1$ for highly reflective substrates we can write the normalized reflected power as

$$\frac{R}{R_0} \simeq \left|1 + 2k_{z,2}d\frac{1 - r_{12}}{1 + r_{12}}\right|^2. \tag{6.5}$$

By defining $\delta^2 = 1 - \sin^2(\Theta) \ll 1$ for grazing incidence ($\Theta \sim 90°$), we find

$$k_{z,i} = (2\pi/\lambda)\sqrt{\epsilon - 1 + \delta^2}. \tag{6.6}$$

Neglecting $\delta^2 \ll 1$ for $\epsilon \neq 1$ and assuming illumination from air ($\epsilon_1 = 1$), the reflection coefficient r_{12} can be written as

$$r_{12} \simeq \frac{\epsilon\delta - \sqrt{\epsilon - 1}}{\epsilon\delta + \sqrt{\epsilon - 1}} \tag{6.7}$$

By inserting eq. (6.7) into eq. (6.5) and using eq. (6.6) we find for the normalized reflected power:

$$\frac{R}{R_0} = \left(1 - 2\frac{(2\pi/\lambda)d}{\delta}\right)^2 + \left(\frac{2(2\pi/\lambda)d}{\delta}\right)^2 \left(1 - \frac{\epsilon'}{|\epsilon|^2}\right)^2. \tag{6.8}$$

Neglecting quadratic terms in $(2\pi/\lambda)d$ and approximating $log(1-x) \approx -x$ for

$x \ll 1$ we finally obtain for the GI-FTIR reflectance the expression

$$\frac{R}{R_0} = 8\pi \frac{d}{\lambda} \frac{1}{\varepsilon'^2} \varepsilon'' \equiv A_r. \tag{6.9}$$

Equation (6.9) explains the blueshift of the experimental GI-FTIR spectrum in Figure 6.2, as the prefactor $1/(\varepsilon')^2$ has a much steeper slope around the resonance than the prefactor $1/\sqrt{\varepsilon'}$ in eq. (6.2). This blushift can also be seen in Figure 6.3a, showing the GI-FTIR (red curve) and FTIR (black curve) spectra of PMMA calculated according to Eqs. (6.9) and (6.2), respectively.

6.3.2 Near-field spectra of ultra-thin and thick organic films

For a theoretical analysis of the nano-FTIR spectra, we describe the tip-scattered field according to established s-SNOM models for non-resonant tips [24, 125]. The incident field E_{inc} illuminates the tip directly and via the reflection r from the sample surface (illustrated in Fig. 6.4). The total field illuminating the tip, $(1+r)E_{inc}$, polarizes the tip and induces a dipole moment $p \propto (1+r)E_{inc}$, which by reciprocity, radiates back into the far field directly and via the reflection, yielding the scattered field $E_{sca} \propto (1+r)^2 E_{inc}$. In close proximity to the sample, the polarized tip interacts with the sample via the near fields localized at the tip apex. This interaction can be described as an infinite series of near-field "reflections" between tip and sample [132, 209] (illustrated in Fig. 6.4), where the reflection at the sample surface is given by a quasi-static near-field reflection coefficient β. Limiting ourselves to a single near-field reflection from the sample, we can describe the demodulated near-field signal by $s_n e^{i\varphi_n} \propto E_{sca,n} \propto \beta(1+r)^2 E_{inc} + O(\beta^2)$. As for optically thin films $r \approx r_{sub}$ [44], the normalization to the scattering from the substrate yields the near-field contrast

$$\eta_3(\omega) \approx \frac{\beta(\omega)}{\beta_{sub}}. \tag{6.10}$$

For a film on a substrate, β is given by a quasi-static version of eq. (6.3) [128]

$$\beta = \frac{\beta_{12} + \beta_{23} e^{-2qd}}{1 + \beta_{12}\beta_{23} e^{-2qd}} \tag{6.11}$$

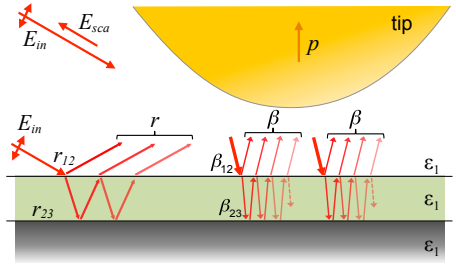

Figure 6.4: Illustration of the far-field illumination of the tip, and of the near-field interaction/scattering between the tip and the sample.

with $\beta_{ij} = (\varepsilon_j - \varepsilon_i)/(\varepsilon_j + \varepsilon_i)$ and q representing the in-plane momentum of the waves scattered by the tip. While in principle the tip generates a wide spectrum of momenta q, the main contribution to the scattering is determined by the tip radius R_t: $q \sim 1/R_t \gg 1/\lambda$ [128]. Thus, the near-field measurements can be analyzed without rigorous integration. In the following, the two limiting cases of an ultra-thin and thick organic film on a substrate are discussed.

For an ultra-thin film, $d \ll R_t$, on a substrate, we find $qd \sim d/R_t \ll 1$. We thus can approximate β in eq. (6.11) by its Taylor expansion in qd which yields the quasi-static analogue of the far-field reflection coefficient in eq. (6.4):

$$\beta = \frac{\beta_{12} + \beta_{23}}{1 + \beta_{12}\beta_{23}} + 2qd\frac{\beta_{23}(1 - \beta_{12}^2)}{1 + \beta_{12}\beta_{23}} + \mathcal{O}\left(qd\right)^2 \tag{6.12}$$

Neglecting expansion orders larger than one and using eq. (6.10) we obtain the near-field contrast

$$\eta_3 = 1 - 2qd\frac{1 - \beta_{12}^2}{1 + \beta_{12}\beta_{23}}\frac{\beta_{23}}{\beta_{12}\beta_{23}} \tag{6.13}$$

For highly reflective substrates with $\beta_{23} \approx 1$ (e.g. Au or Si), we can simplify the near-field contrast η_3 in eq. (6.10) to

$$\eta_3 \approx 1 - 2qd\frac{1 - \beta_{12}^2}{(1 - \beta_{12}^2)} = 1 - 2qd\frac{1 - \beta}{1 + \beta} = 1 - 2qd/\varepsilon. \tag{6.14}$$

By neglecting ϵ'' in the denominator of eq. (6.15) and approximate $\arctan(x) \approx x$ for $x \ll 1$ in the derivation of φ_3, we find for the near-field absorption a_3

and phase φ_3:

$$a_3 \approx \varphi_3 \approx 2qd\frac{1}{\varepsilon'^2}\varepsilon''. \tag{6.15}$$

Comparing eq. (6.15) with the GI-FTIR signal in eq. (6.9), we see that apart from the pre-factors the expressions are virtually identical. This result explains the good experimental agreement between the near-field absorption, near-field phase, and GI-FTIR spectra of the thinnest PMMA film in Figure 6.2. Note that an additional linear frequency-dependence of the factor $1/\lambda \propto \omega$ in eq. (6.9) is of no significant influence due to the typically small width of molecular spectral features. We corroborate our analysis by calculating the near-field absorption $a_3 = \mathrm{Im}(\eta_3)$ and phase φ_3 spectra of PMMA according to eq. (6.15) (see Fig. 6.3b). The results show an excellent agreement of the nano-FTIR peak positions with the peak position of the GI-FTIR spectrum (red curve, Fig. 6.3a). We explain this agreement by the similarity of the probing mechanisms. In GI-FTIR, the probing electric field experiences reflection at the film surface and the substrate, as well as absorption in the film (reflection-absorption measurements [5]). The same reflection and absorption processes occur for the near fields when the film is thinner than the near-field decay length (compare Eqs. (6.3) and (6.11)).

The other limiting case is a thick film, $d \gg R_t$, hence $qd \sim d/R_t \gg 1$ (though still $d \ll \lambda$). Thus the exponential in eq. (6.11) tends to zero, $exp(-2qd) \to 0$, β (eq. (6.11)) reduces to

$$\beta \simeq \beta_{12} = \frac{\epsilon - 1}{\epsilon + 1}. \tag{6.16}$$

Hence, we recover the near-field absorption reported in refs. [42] and [44]

$$a_3 = \mathrm{Im}(\eta_3) \propto \mathrm{Im}(\beta_{12}) \simeq \frac{2}{(\varepsilon' + 1)^2}\varepsilon'' \tag{6.17}$$

Evaluating eq. (6.17) for PMMA, we observe a redshift of the near-field absorption peak (green dashed curve, Fig. 6.3c) compared to the GI-FTIR (red curve, Fig. 6.3a) and near-field phase (blue curve, Fig. 6.3c) spectra. The slight blue-shift compared to the far-field absorbance spectrum of $\kappa\omega$ (eq. (6.2), black curve, Fig. 6.3a) vanishes completely when the higher order terms neglected in eq. (6.10) are considered, e.g., when the near-field contrast is calculated according to the Finite Dipole Model [125] (green curve, Fig. 6.3c). We thus confirm the experimentally observed good match between the near-

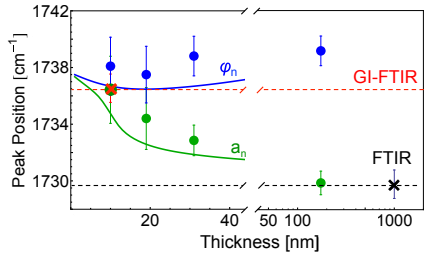

Figure 6.5: **Spectral peak positions as a function of PMMA film thickness.** Symbols are the measured positions of the near-field phase φ_3 (blue dots), near-field absorption a_3 (green dots), GI-FTIR (red cross), and transmission FTIR (black cross) spectra. Solid lines are the calculated peak positions using the FDM-based model by Hauer et al. [128] with model parameters as in Figure 6.3.

field absorption a_3 and the FTIR spectrum. It can be understood by the fact that both transmission FTIR and nano-FTIR absorption of thick films are dominated by absorption in the film, with no significant far-field, respectively, near-field, reflection at the substrate.

For the near-field phase of thick organic films, we obtain

$$\varphi_3 = \arg(\eta_3) \approx \mathrm{Im}(\beta) \approx \frac{2}{\varepsilon'^2 - 1}\varepsilon''. \tag{6.18}$$

The spectrum of $\varphi_3(\omega)$, calculated for PMMA according to (6.18) (blue curve, Fig. 6.3c), is blue-shifted by about 2 cm^{-1} but comparable to the GI-FTIR spectrum (red curve, Fig. 6.3a), confirming the observations in Figure 6.2.

For intermediate film thicknesses, the near-field response is determined by the interplay between the thick and the ultra-thin film regimes depending on the value $qd \sim d/R_t$ (eq. (6.11)), giving rise to thickness-dependent peak shifts. To verify the trends observed in Figure 6.2, we calculated the peak positions in nano-FTIR absorption and phase spectra based on a more rigorous quasi-analytical s-SNOM model for layered samples [128]. The calculated peak position for nano-FTIR absorption (green curve, Fig. 6.5) quickly redshifts with increasing film thickness d, while the phase peak position (blue curve, Fig. 6.5) stays nearly constant. Both observations are in good agreement with the experimental results (green and blue dots, Fig. 6.5). The systematic blueshift of the calculation compared to the experiment is attributed to differences in

the permittivity of PMMA used in experiments (495 kDa molecular weight) and in calculations (950 kDa).

Note that the results and analysis are valid only for highly reflective substrates typically employed in nano-FTIR. Calculations for weakly reflecting substrates (not presented here) indicate that the film thickness-related behavior of nano-FTIR absorption and phase spectra essentially reverse. That is, the nano-FTIR absorption peak position stays almost constant with thickness and matches well the transmission FTIR. On the other hand, the peak position of the phase spectrum is thickness-dependent: for thin films, it matches the transmission FTIR spectrum, while for thicker films it shifts towards the GI-FTIR spectrum.

6.4 Summary and conclusion

In summary, we studied the peak positions in near-field phase φ_n and near-field absorption a_n spectra of thin organic films, both quantities related to the absorption in molecular samples. We found that the spectral position of the near-field phase is nearly constant with varying film thickness, while being blueshifted by a few wavenumbers compared to GI-FTIR spectra. When a small shift is of no major importance, near-field phase spectra promise material identification of a sample of unknown or varying thickness (size). The peak positions in near-field absorption spectra were found to agree well with that of GI-FTIR and FTIR spectra for ultra-thin and thick films, respectively, allowing for a direct comparison. When the sample thickness is intermediate or unknown, and a highly accurate measurement of an absorption feature is required, modeling is necessary to extract the absorption coefficient κ, which can be directly compared with FTIR absorbance spectra [132]. Note that our results and guidelines also apply for other amplitude- and phase-resolved s-SNOM-based spectroscopic techniques, which, for example, employ tunable laser sources.

A Potential response of a layered sample to monopole Q

To extend the Finite Dipole Model to layered sample, as introduced in Section 3.5.3, the potential response Φ to a monopole charge Q at distance z_0 above a bulk sample with a top layer of thickness d needs to be calculated. This can be achieved by solving the boundary conditions for the total potential U and its derivative perpendicular to the interface [128, 135]. Choosing the spatial coordinate z perpendicular to the sample surface, the potential above the sample in cylindrical coordinates (r, θ, z) is given by [135]

$$U = -\frac{Q}{4\pi\epsilon_0}\left(\frac{1}{\sqrt{r^2+z^2}} + \Phi\right) \tag{A.1}$$

with

$$\Phi = \int_0^\infty A(k)e^{kz}J_0(kr)dk, \tag{A.2}$$

$$A(k) = e^{-2kz_0}\frac{\beta_{12} + \beta_{23}e^{-2kd}}{1 - \beta_{12}\beta_{23}e^{-2kd}}. \tag{A.3}$$

J_0 is the zeroth order Bessel function of first kind, ϵ_0 the vacuum permittivity, ϵ_i with $i = 1, 2, 3$ the dielectric permittivities of air, layer, and sample, respectively. d is the thickness of the layer and β_{ij} the quasi-static reflection coefficient at interface ij:

$$\beta_{ij} = \frac{\epsilon_i - \epsilon_j}{\epsilon_i + \epsilon_j}. \tag{A.4}$$

B Bibliography

[1] Bernhard Schrader, editor. *Infrared and Raman spectroscopy*. VCH Verlagsgesellschaft mbH, 1995.

[2] Max Born and Emil Wolf. *Principles of Optics*. Cambridge University Press, 7th edition, 1999.

[3] Alan J. Lacey, editor. *Light Microscopy in Biology*. Oxford University Press, 2nd edition, 1999.

[4] Jerome Mertz. *Introduction to optical microscopy*. Roberts and Company Publishers, Greenwood Village, CO, USA, 2016.

[5] Peter R. Griffith and James A. de Haseth. *Fourier Transform Infrared Spectroscopy*. John Wiley & Sons, Inc., Hoboken New Jersey, 2nd edition, 2007.

[6] Daniel M. Mittleman. *Sensing with Terahertz Radiation*. Springer Berlin Heidelberg, 2003.

[7] Claus Klingshirn. *Semiconductor Optics*. Springer Berlin Heidelberg, 2nd edition, 2005.

[8] Susan L. Dexheimer, editor. *Terahertz Spectroscopy*. Taylor & Francis Group, LLC, Boca Raton, USA, 2008.

[9] Ernst Abbe. Beiträge zur theorie der mikroskops und der mikroskopischen wahrnehmung. *Archiv für Mikroskopische Anatomie*, 9(1):413–461, 1873.

[10] Lord Rayleigh. Investigations in optics, with special reference to the spectroscope. *Philosophical Magazine*, 8:261–274, 1879.

[11] Lukas Novotny and Bert Hecht. *Principles of Nano-Optics*. Cambridge University Press, 2nd edition, 2012.

[12] Guozhong Cao. *Nanostructures and Nanomaterials: Synthesis, Properties and Applications*. World Scientific Publishing, Singapore, 2004.

[13] Philippe Knauth and Joop Schoonman, editors. *Nanocomposites*. Springer Berlin Heidelberg, 2008.

[14] Changhong Ke, editor. *Recent advances in nanotechnology*. Apple Academic Press, Toronto, 2011.

[15] Gustav Van Tendeloo, Dirk van Dyck, and Stephen J. Pennycook, editors. *Handbook of Nanoscopy*, volume 1 + 2. Wiley-VCH, 2012.

[16] E. Mayer, H. J. Hug, and R. Bennewitz. *Scanning Probe Microscopy: The Lab on a Tip*. Springer, 2004.

[17] Zhong Lin Wang. *Scanning Microscopy for Nanotechnology*. Springer New York, New York, NY, 2006.

[18] S. Morita, editor. *Roadmap of Scanning Probe Microscopy*. Springer, Berlin Heidelberg New York, 2007.

[19] P.U. Jepsen, D.G. Cooke, and M. Koch. Terahertz spectroscopy and imaging - modern techniques and applications. *Laser & Photon. Rev.*, 5(1):124–166, Oct 2010.

[20] Qingkai Yu, Luis A Jauregui, Wei Wu, Robert Colby, Jifa Tian, Zhihua Su, Helin Cao, Zhihong Liu, Deepak Pandey, Dongguang Wei, Ting Fung Chung, Peng Peng, Nathan P Guisinger, Eric A Stach, Jiming Bao, Shin-Shem Pei, and Yong P Chen. Control and characterization of individual grains and grain boundaries in graphene grown by chemical vapour deposition. *Nat Mater*, 10(6):443–9, Jun 2011.

[21] W. Zouaghi, M. D. Thomson, K. Rabia, R. Hahn, V. Blank, and H. G. Roskos. Broadband terahertz spectroscopy: principles, fundamental research and potential for industrial applications. *European Journal of Physics*, 34:179–199, 2013.

[22] Y. Inouye and S. Kawata. Near-field scanning optical microscope with a metallic probe tip. *Optics Letters*, 19(3):159, February 1994.

[23] F. Zenhausern, M. P. O. O'Boyle, and H. K. Wickramasinghe. Apertureless nearfield optical microscope. *Applied Physics Letters*, 64(13):1623–1625, 1994.

[24] Fritz Keilmann and Rainer Hillenbrand. *Nano-optics and Near-field Optical Microscopy*, chapter IV: Apertureless Near-Field Optical Microscopy. Artech/House, 1st edition, 2008.

[25] R. Hillenbrand and F. Keilmann. Complex optical constants on a subwavelength scale. *Physical Review Letters*, 85(14):3029–32, October 2000.

[26] Rainer Hillenbrand, Bernhard Knoll, and Fritz Keilmann. Pure optical contrast in scattering-type scanning near-field optical microscopy. *Journal of Microscopy*, 202:77–83, 2001.

[27] T. Taubner, R. Hillenbrand, and F. Keilmann. Performance of visible and mid-infrared scattering-type near-field optical microscopes. *Journal of microscopy*, 210(Pt 3):311–4, June 2003.

[28] Markus B. Raschke and Christoph Lienau. Apertureless near-field optical microscopy: Tip-sample coupling in elastic light scattering. *Applied Physics Letters*, 83(24):5089–5091, 2003.

[29] R Hillenbrand, T Taubner, and F Keilmann. Phonon-enhanced light matter interaction at the nanometre scale. *Nature*, 418(6894):159–62, July 2002.

[30] Markus B. Raschke, Leopoldo Molina, Thomas Elseasser, Dong Ha Kim, Wolfgang Knoll, and Karsten Hinrichs. Apertureless near-field vibrational imaging of block-copolymer nanostructures with ultrathin spatial resolution. *Chemphyschem*, 6(10):2197–2203, 2005.

[31] T. Taubner, R. Hillenbrand, and F. Keilmann. Nanoscale polymer recognition by spectral signature in scattering infrared near-field microscopy. *Applied Physics Letters*, 85(21):5064, 2004.

[32] B Deutsch, R Hillenbrand, and L Novotny. Near-field amplitude and phase recovery using phase-shifting interferometry. *Optics Express*, 16(2):494–501, January 2008.

[33] Hou-Ton Chen, Roland Kersting, and Gyu Cheon Cho. Terahertz imaging with nanometer resolution. *Applied Physics Letters*, 83(15):3009, 2003.

[34] Kanglin Wang, Adrian Barkan, and Daniel M. Mittleman. Propagation effects in apertureless near-field optical antennas. *Applied Physics Letters*, 84(2):305–307, 2004.

[35] Gyu Cheon Cho, Hou-Tong Chen, Simon Kraatz, Nicholas Karpowicz, and Roland Kersting. Apertureless terahertz near-field microscopy. *Semiconductor Science and Technology*, 20:286–292, 2005.

[36] Fritz Keilmann, Andreas J. Huber, and Rainer Hillenbrand. Nanoscale conductivity contrast by scattering-type near-field optical microscopy in the visible, infrared and thz domains. *Journal of Infrared, Millimeter and Terahertz Waves*, 30(12):1255–1268, 2009.

[37] Andreas J. Huber, Fritz Keilmann, J. Wittborn, Javier Aizpurua, and Rainer Hillenbrand. Terahertz near-field nanoscopy of mobile carriers in single semiconductor nanodevices. *Nano Letters*, 8(11):3766–3770, 2008.

[38] Aurele Joseph Louis Adam. Review of near-field terahertz measurement methods and their applications. *Journal of Infrared, Millimeter and Terahertz Waves*, 32:976–1019, 2011.

[39] Fritz Keilmann and Rainer Hillenbrand. Near-field microscopy by elastic light scattering from a tip. *Philosophical Transactions of the Royal Society A*, 362(1817):787–805, April 2004.

[40] Fritz Keilmann and Rainer Hillenbrand. *Nano-optics and Near-field Optical Microscopy*. Artech/House, 1st edition, 2008.

[41] Sergiu Amarie, Paul Zaslansky, Yusuke Kajihara, Erika Griesshaber, Wolfgang W. Schmahl, and Fritz Keilmann. Nano-ftir chemical mapping of minerals in biological materials. *Beilstein Journal of Nanotechnology*, 3:312–323, 2012.

[42] Florian Huth, Alexander Govyadinov, Sergiu Amarie, Wiwat Nuansing, Fritz Keilmann, and Rainer Hillenbrand. Nano-FTIR absorption spec-

troscopy of molecular fingerprints at 20 nm spatial resolution. *Nano Letters*, 12(8):3973–8, August 2012.

[43] Bernhard Knoll and Fritz Keilmann. Near-field probing of vibrational absorption for chemical microscopy. *Nature*, 399:134–137, March 1999.

[44] Alexander A. Govyadinov, Iban Amenabar, Florian Huth, P. Scott Carney, and Rainer Hillenbrand. Quantitative measurement of local infrared absorption and dielectric function with tip-enhanced near-field microscopy. *The Journal of Physical Chemistry Letters*, 4:1526–1531, 2013.

[45] Iban Amenabar, Simon Poly, Wiwat Nuansing, Elmar H. Hubrich, Alexander A. Govyadinov, Florian Huth, Roman Krutokhvostov, Lianbing Zhan, Joachim Heberle, Alexander M. Bittner, and Rainer Hillenbrand. Structural analysis and mapping of individual protein complexes by infrared nanospectroscopy. *Nature Communications*, 4(2890), December 2013.

[46] Joanna M Atkin, Paul M Sass, Paul E Teichen, Joel D Eaves, and Markus B Raschke. Nanoscale probing of dynamics in local molecular environments. *J Phys Chem Lett*, pages 4616–4621, Nov 2015.

[47] Eric A. Muller, Benjamin Pollard, and Markus B. Raschke. Infrared chemical nano-imaging: Accessing structure, coupling, and dynamics on molecular length scales. *The Journal of Physical Chemistry Letters*, 6(1275-1284), 2015.

[48] Stefan Mastel, Alexander A. Govyadinov, Thales V. A. G. de Oliveira, Iban Amenabar, and Rainer Hillenbrand. Nanoscale-resolved chemical identification of thin organic films using infrared near-field spectroscopy and standard fourier transform infrared references. *Applied Physics Letters*, 106(023113), 2015.

[49] Vesna Stanic, Francisco Carlos Barbosa Maia, Raul de Oliveira Freitas, Fabiano Emmanuel Montoro, and Kenneth Evans-Lutterodt. The chemical fingerprint of hair melanosomes by infrared nano-spectroscopy. *Nanoscale*, 10:14245–14253, 2018.

[50] Shixin Huang, Mohamadamin Makaram, Sarah N. Kiemle, Hossein Hamedi, Moujhur Sau, Daniel J. Cosgrove, and Seong H. Kim. Inhomogeneity of cellulose microfibril assembly in plant cell walls revealed with sum frequency generation microscopy. *Journal of Physical Chemistry B*, 122(19):5006–5019, 2918.

[51] Matthias Rang, Andrew C Jones, Fei Zhou, Zhi-Yuan Li, Benjamin J Wiley, Younan Xia, and Markus B Raschke. Optical near-field mapping of plasmonic nanoprisms. *Nano Letters*, 8(10):3357–63, October 2008.

[52] Andrew C Jones, Robert L Olmon, Sara E Skrabalak, Benjamin J Wiley, Younan N Xia, and Markus B Raschke. Mid-IR plasmonics: near-field imaging of coherent plasmon modes of silver nanowires. *Nano Letters*, 9(7):2553–8, July 2009.

[53] Pablo Alonso-Gonzáles, Martin Schnell, Paulo Sarriugarte, Heidar Sobhani, Chihhui Wu, Nihal Arju, Alexander Khanikaev, Federico Golmar, Pablo Albella, Libe Arzubiaga, Felix Casanova, Luis E Hueso, Peter Nordlander, Gennady Shvets, and Rainer Hillenbrand. Real-space mapping of Fano interference in plasmonic metamolecules. *Nano Letters*, 11(9):3922–6, September 2011.

[54] Martin Schnell, Pablo Alonso-González, Libe Arzubiaga, Felix Casanova, Luis E. Hueso, Andrey Chuvilin, and Rainer Hillenbrand. Nanofocusing of mid-infrared energy with tapered transmission lines. *Nature Photonics*, 5(April):283–287, 2011.

[55] S. Mastel, S. E. Grefe, G. B. Cross, a. Taber, S. Dhuey, S. Cabrini, P. J. Schuck, and Y. Abate. Real-space mapping of nanoplasmonic hotspots via optical antenna-gap loading. *Applied Physics Letters*, 101(13):131102, 2012.

[56] Pablo Alonso-Gonzáles, Pablo Albella, Martin Schnell, Jianing Chen, Florian Huth, Aitzol García-Etxarri, Felix Casanova, Federico Golmar, Libe Arzubiaga, Luis E. Hueso, Javier Aizpurua, and Rainer Hillenbrand. Resolving the electromagnetic mechanism of surface-enhanced light scattering at single hot spots. *Nature Communications*, 3:684, January 2012.

[57] Vladimir A. Zenin, Radu Malureanu, Ilya P. Radko, Andrei V. Lavrinenko, and Sergey I. Bozhevolni. Near-field characterization of bound plasmonic modes in metal strip waveguides. *Optics Express*, 24(5):4582–4590, 2016.

[58] Andrei Andryieuski, Vladimir A. Zenin, Radu Malureanu, Valenty S. Volkov, Sergey I. Bozhevolni, and Andrei V. Lavriknenko. Direct characterization of plasmonic slot waveguides and nanocouplers. *Nano Letters*, 14:3925–3929, 2014.

[59] Jianing Chen, Michela Badioli, Pablo Alonso-Gonzáles, Sukosin Thongrattanasiri, Florian Huth, Johann Osmond, Marko Spasenovic, Alba Centena, Amaia Pesquera, Philippe Godignon, Amaia Zurutuza Elorza, Nicolas Camara, F. Javier García de Abajo, Rainer Hillenbrand, and Frank H. L. Koppens. Optical nano-imaging of gate-tunable graphene plasmons. *Nature*, 487:77, 2012.

[60] Z. Fei, A. S. Rodin, G. O. Andreev, W. Bao, A. S. McLeod, M. Wagner, L. M. Zhang, Z. Zhao, M. Thiemens, G. Dominguez, M. M. Fogler, A. H. Castro-Neto, C. N. Lau, Fritz Keilmann, and D. N. Basov. Gate-tuning of graphene plasmons revealed by infrared nano-imaging. *Nature*, 487(83), 2012.

[61] S. Dai, Z. Fei, Q. Ma, A. S. Rodin, M. Wagner, A. S. McLeod, M. K. Liu, W. Gannett, W. Regan, K. Watanabe, T. Taniguchi, M. Thiemens, G. Dominguez, A. H. Castro-Neto, A. Zettl, F. Keilmann, P. Jarillo-Herrero, M. M Fogler, and D. N. Basov. Tunable phonon polaritons in atomically thin van der waals crystals of boron nitride. *Science (New York, N.Y.)*, 343:1125–1129, 2014.

[62] Edward Yoxall, Martin Schnell, Alexey Yu. Nikitin, Oihana Txoperena, Achim Woessner, Mark B. Lundeberg, Felix Casanova, Luis E. Hueso, Frank H. L. Koppens, and Rainer Hillenbrand. Direct observation of ultraslow hyperbolic polariton propagation with negative phase velocity. *Nature Photonics*, 9:674–679, 2015.

[63] D. N. Basov, M. M. Fogler, and F. J. Garcia de Abajo. Polaritons in van der waals materials. *Science*, 354(6309):aag1992–aag1992, Oct 2016.

[64] Pablo Alonso-González, Alexey Y. Nikitin, Yuanda Gao, Achim Woessner, Mark B. Lundeberg, Alessandro Principi, Nicolò Forcellini, Wenjing Yan, Saül Vélez, Andreas. J. Huber, Kenji Watanabe, Takashi Taniguchi, Félix Casanova, Luis E. Hueso, Marco Polini, James Hone, Frank H. L. Koppens, and Rainer Hillenbrand. Acoustic terahertz graphene plasmons revealed by photocurrent nanoscopy. *Nature Nanotechnology*, 12:31–35, 2017.

[65] Alexey Yu. Nikitin, Pablo Alonso-Gonzáles, S. Vélez, Stefan Mastel, Alba Centena, Amaia Pesquera, Amaia Zurutuza, Felix Casanova, L. E. Hueso, Frank H. L. Koppens, and Rainer Hillenbrand. Real-space mapping of tailored sheet and edge plasmons in graphene nanoresonators. *Nature Photonics*, 10:239–244, April 2016.

[66] Bernhard Knoll and Fritz Keilmann. Infrared conductivity mapping for nanoelectronics. *Applied Physics Letters*, 77:3980–3982, 2000.

[67] J. S. Samson, G. Wollny, E. Bründermann, A. Bergner, A. Hecker, G. Schwaab, A. D. Wiek, and M. Havenith. Setup of a scanning near field infrared microscope (snim): imaging of sub-surface nano-structures in gallium-doped silicon. *Physical Chemistry Chemical Physics*, 8(6):753–758, 2006.

[68] M. M. Quazilbash, M. Brehm, Byung-Gyu Chae, P.-C. Ho, G. O. Andreev, Bong-Jun Kim, Sun Jin Yun, A. V. Balatsky, M. B. Maple, Fritz Keilmann, Hyun-Tak Kim, and D. N. Basov. Mott transition in vo_2 revealed by infrared spectroscopy and nano-imaging. *Science*, 318:1750–1753, 2007.

[69] J M Stiegler, A J Huber, S L Diedenhofen, J Gómez Rivas, R E Algra, E P a M Bakkers, and R Hillenbrand. Nanoscale free-carrier profiling of individual semiconductor nanowires by infrared near-field nanoscopy. *Nano Letters*, 10(4):1387–92, April 2010.

[70] Earl T. Ritchie, David J. Hill, Tucker M. Mastin, Panfilo C. Deguzman, James F. Cahoon, and Joanna M. Atkin. Mapping free-carriers in multijunction silicon nanowires using infrared near-field optical microscopy. *Nano Letters*, 17(11):6591–6597, Oct 2017.

[71] Andrea Arcangeli, Francesco Rossella, Andrea Tomadin, Jihua Xu, Daniele Ercolani, Lucia Sorba, Fabio Beltram, Alessandro Tredicucci, Marco Polini, and Stefano Roddaro. Gate-tunable spatial modulation of localized plasmon resonances. *Nano Letters*, 16(9):5688–93, Sep 2016.

[72] Clemens Liewald, Stefan Mastel, Jeffrey L. Hesler, Andreas J. Huber, Rainer Hillenbrand, and Fritz Keilmann. All-electronic terahertz nanoscopy. *Optica*, 5(2):159–163, 2018.

[73] Florian Huth, Andrey Chuvilin, Martin Schnell, Iban Amenabar, Roman Krutokhvostov, Sergei Lopatin, and Rainer Hillenbrand. Resonant antenna probes for tip-enhanced infrared near-field microscopy. *Nano Letters*, 13:1065–1072, 2013.

[74] Stefan Mastel, Mark B. Lundeberg, Pablo Alonso-González, Yuanda Gao, Kenji Watanabe, Takashi Taniguchi, James Hone, Frank H. L. Koppens, Alexey Y. Nikitin, and Rainer Hillenbrand. Terahertz nanofocusing with cantilevered terahertz-resonant antenna tips. *Nano Letters*, 17(11):6526–6533, Oct 2017.

[75] Stefan Mastel, Alexander A. Govyadinov, Curdin Maissen, Andreas Berger, Andrey Chuvilin, and Rainer Hillenbrand. Understanding the image contrast of material boundaries in ir nanoscopy reaching 5 nm spatial resolution. *ACS Photonics*, 5(8):3372–3378, 2018.

[76] Michael J. Rust, Mark Bates, and Xiaowei Zhuang. Sub-diffraction-limit imaging by stochastic optical reconstruction microscopy (storm). *Nature Methods*, 3(10):793–796, October 2006.

[77] Xiaowei Zhuang. Nano-imaging with storm. *Nature Photonics*, 3(7):365–367, July 2009.

[78] Eric Betzig, George H. Patterson, Rachid Sougrat, O. Wolf Lindwasser, Scott Olenych, Juan S. Bonifacino, Michael W. Davidson, Jennifer Lippincott-Schwartz, and Harald F. Hess. Imaging intracellular flourescent proteins at nanometer resolution. *Science*, 313:1642–1645, 2006.

[79] Kim I. Mortensen, L. Stirling Churchman, James A. Spudish, and Henrik Flyvbjerg. Optimized localization analysis for single-molecule tracking and super-resolution microscopy. *Nature Methods*, 7:377–381, 2010.

[80] Dominik Wildanger, Brian R. Patton, Heiko Schill, Luca Marseglia, J. P. Hadden, Sebastian Kauer, Andreas Schönle, John G. Rarity, Jeremy L. O'Brian, Stefan W. Hell, and Jason M. Smith. Solid immersion facilitates fluorescence microscopy with nanometer resolution and sub-ångström emitter localization. *Advanced Materials*, 24(44), 2012.

[81] Stefan W. Hell and Jan Wichmann. Breaking the diffraction resolution limit by stimulated emission: stimulated-emission-depletion flourescence microscopy. *Optics Letters*, 19(11):780–782, 1994.

[82] Katrin I. Willig, Silvio O. Rizzoli, Volker Westphal, Reinhard Jahn, and Stefan W. Hell. Sted microscopy reveals that synaptotagmin remains clustered after synaptic vesicle exocytosis. *Nature*, 440:935–939, 2006.

[83] J. Goldstein. *Scanning electron microscopy and X-ray microanalysis*. Kluwer Academic/Plenum Publishers, 3rd edition, 2003.

[84] Stephen J. Pennycook and Peter D. Nellist, editors. *Scanning Transmission Electron Microscopy - Imaging and Analysis*. Springer Science+Business, 2011.

[85] G. Binning, H. Rohrer, Ch. Gerber, and E. Weibel. Surface studies by scanning tunneling microscopy. *Physical Review Letters*, 49(1):57–61, 1982.

[86] G. Binnig and C. F. Quate. Atomic force microscope. *Physical Review Letters*, 56(9):930–933, March 1986.

[87] Peter Eaton and Paul West. *Atomic Force Microscopy*. Oxford University Press, first edition, 2010.

[88] Stefan Mastel. Infrared near-field nanoimaging and nanospectroscopy with a quantum cascade laser. Master's thesis, Department of Physics and Astronomy, University of Heidelberg, 2014.

[89] E. Synge. A suggested method for extending microscopie resolution into the ultra-microscopie regime. *Philosophical Magazine*, 6(356), 1928.

[90] E. Synge. An application of piezoelectricity to microscopy. *Philosophical Magazine*, 13(297), 1932.

[91] E. A. Ash and G. Nicholls. Super-resolution aperture scanning microscope. *Nature*, 237, June 1972.

[92] D. W. Pohl, W. Denk, and M. Lanz. Optical stethoscopy: Image recording with resolution $\lambda/20$. *Applied Physics Letters*, 44(7):651, 1984.

[93] A. Lewis, M. Isaacson, A. Harootunian, and A. Muray. Development of a 500 A spatial resolution light microscope. *Ultramicroscopy*, 13:227–232, 1984.

[94] E. Betzig, J. K. Trautmann, T. D. Harris, J. S. Weiner, and R. L. Kostelak. Breaking the diffraction barrier: Optical microscopy on a nanometer scale. *Science*, 251:1468–1470, March 1991.

[95] Rainer Hillenbrand. *Nahfeldoptische Amplitude- und Phasenkontrstmikroskopie zur nanoskopischen optischen Abbildung von Materialkontrasten und optische resonanten Partikeln*. PhD thesis, Technische Universität München, 2001.

[96] Bernhard Knoll and Fritz Keilmann. Electromagnetic fields in the cutoff regime of tapered metallic waveguides. *Optics Communications*, 162:177–181, April 1999.

[97] Curtis Marcott, Tadashi Awatani, Jiping Ye, David Gerrard, Michael Lo, and Kevin Kjoller. Review of nanoscale infrared spectroscopy applications to energy related materials. *Spectroscopy Europe*, 26(1), 2014.

[98] Alexandre Dazzi and Craig B. Prater. Afm-ir: Technology and applications in nanoscale infrared spectroscopy and chemical imaging. *Chemical Reviews*, Dec 2016.

[99] Brian T. O'Callahan, Jun Yan, Fabian Menges, Eric A. Muller, and Markus B. Raschke. Photoinduced tip-sample forces for chemical nanoimaging and spectroscopy. *Nano Letters*, 18:5499–5505, 2018.

[100] Derek Nowak, William Morrison, H. K. Wickramasinghe, Junghoon Jahng, Eric Porma, Lei Wan, Ricardo Ruiz, Thomas R. Albrecht, Kristin Schmidt, Jane Frommer, Daniel P. Sanders, and Sung Park. Nanoscale chemical imaging by photoinduced force microscopy. *Science Advances*, 2(1501571), 2016.

[101] Ryan A. Murdick, William Morrison, Derek Nowak, Thomas R. Albrecht, Junghoon Jahng, and Sung Park. Photoinduced force microscopy: A technique for hyperspectral nanochemical mapping. *Japanese Journal of Applied Physics*, 56(08LA04), 2017.

[102] Mohammad Almajhadi and H. Kumar Wickramasinghe. Contrast and imaging performance in photo induced force microscopy. *Optics Express*, 25(22):26923–26938, 2017.

[103] Alexandre Dazzi, R. Prazeres, F. Glotin, and J. M. Ortega. Local infrared microspectroscopy with subwavelength spatial resolution with an atomic force microscope tip used as a photothermal sensor. *Optics Letters*, 30(18):2388–2390, 2005.

[104] C Mayet, A Dazzi, R Prazeres, F Allot, F Glotin, and J M Ortega. Sub-100 nm IR spectromicroscopy of living cells. *Optics Letters*, 33(14):1611–3, July 2008.

[105] Aaron M Katzenmeyer, Vladimir Aksyuk, and Andrea Centrone. Nanoscale infrared spectroscopy: improving the spectral range of the photothermal induced resonance technique. *Analytical Chemistry*, 85(4):1972–9, February 2013.

[106] Basudev Lahiri, Glenn Holland, and Andrea Centrone. Chemical imaging beyond the diffraction limit: Experimental validation of the ptir technique. *Small*, 9(3):439–445, 2012.

[107] Feng Lu, Mingzhou Jin, and Mikhail A. Belkin. Tip-enhanced infrared nanospectroscopy via molecular expansion force detection. *Nature Photonics*, 8(4):307–312, Jan 2014.

[108] K. B. Crozier, A. Sundaramurthy, G. S. Kino, and C. F. Quate. Optical antennas: Resonators for local field enhancement. *Journal of Applied Physics*, 94(7):4632–4642, Oct 2003.

[109] A. Madrazo, R. Carminati, M. Nieto-Vesperinas, and J.-J. Greffet. Polarization effects in the optical interaction between a nanoparticle and a corrugated surface: implications for apertureless near-field microscopy. *Journal of the Optical Society of America A*, 15(1):109, 1998.

[110] Marco Salerno, Joachim R. Krenn, B. Lamprecht, Gerburg Schider, Harald Ditlbacher, Nordin Félidj, Alfred Leitner, and Franz R. Aussenegg. Plasmon polaritons in metal nanostructures: the optoelectronic route to nanotechnology. *Optoelectronics Review*, 10(3):217–224, 2002.

[111] J. R. Krenn and J. C. Weeber. Surface plasmon polaritons in metal stripes and wires. *Philosophical Transactions of the Royal Society of London, Series A*, 362:739–756, 2004.

[112] Jean-Jacques Greffet and Rémi Carminati. Image formation in near-field optics. *Progress in Surface Science*, 56(3):133–237, 1998.

[113] R. Hillenbrand and F. Keilmann. Material-specific mapping of metal/semiconductor/dielectric nanosystems at 10 nm resolution by backscattering near-field optical microscopy. *Applied Physics Letters*, 80(1):25, 2002.

[114] Kuan-Ting Lin, Susumu Komiyama, Sunmi Kim, Ken-ichi Kawamura, and Yusuke Kajihara. A high signal-to-noise ratio passive near-field microscope equipped with a helium-free cryostat. *Review of Scientific Instruments*, 88(1):013706, Jan 2017.

[115] Maria C. Giordano, Stefan Mastel, Clemens Liewald, Lorenzo L. Columbo, Massimo Brambilla, Leonardo Viti, Antonio Politano, Kai Zhang, Lianhe Li, A. Giles Davies, Edmund H. Linfield, Rainer Hillenbrand, Fritz Keilmann, Gaetano Scamarcio, and Miriam S. Vitiello. Phase-resolved terahertz self-detection near-field microscopy. *Optics Express*, 26(14):18423–18435, 2018.

[116] Nenad Ocelic, Andreas J. Huber, and Rainer Hillenbrand. Pseudoheterodyne detection for background-free near-field spectroscopy. *Applied Physics Letters*, 89(10):101124, 2006.

[117] Nenad Ocelic. *Quantitative Near-field Phonon-polariton Spectroscopy*. PhD thesis, Technische Universität München, Boltzmannstraße 15, München, 2007.

[118] Martin Schnell, P. Scott Carney, and Rainer Hillenbrand. Synthetic optical holography for rapid nanoimaging. *Nature Communications*, 5:3499, 2014.

[119] D. Gabor. A new microscopic principle. *Nature*, 161:777–778, 1948.

[120] P. Hariharan. *Basics of holography*. Cambridge University Press, 2002.

[121] Martin Schnell, A. García-Etxarri, Andreas J. Huber, Kenneth B. Crozier, Javier Aizpurua, and Rainer Hillenbrand. Controlling the near-field oscillations of loaded plasmonic nanoantennas. *Nature Photonics*, 3(April):287–291, 2009.

[122] F Huth, M Schnell, J Wittborn, N Ocelic, and R Hillenbrand. Infrared-spectroscopic nanoimaging with a thermal source. *Nature Materials*, 10(5):352–6, May 2011.

[123] Florian Huth. *Nano-FTIR - Nanoscale Infrared Near-Field Spectroscopy*. PhD thesis, Universidad del Pais Vasco, 2015.

[124] Fritz Keilmann and Sergiu Amarie. Mid-infrared frequency comb spanning an octave based on an er fiber laser and difference-frequency generation. *Journal of Infrared, Millimeter, and Terahertz Waves*, 33(5):479–484, 2012.

[125] Antonija Cvitkovic, Nenad Ocelic, and Rainer Hillenbrand. Analytical model for qunatitative prediction of material contrast in scattering-type near-field optical microscopy. *Optics Express*, 15(14):8550–8565, 2007.

[126] N Ocelic and R Hillenbrand. Subwavelength-scale tailoring of surface phonon polaritons by focused ion-beam implantation. *Nature Materials*, 3(9):606–9, September 2004.

[127] Iban Amenabar. *Infrared nanospectroscopy and hyperspectral nanoimaging of organic matter*. PhD thesis, Universidad del Pais Vasco, 2017.

[128] Benedikt Hauer, Andreas P. Engelhardt, and Thomas Taubner. Quasi-analytic model for scattering infrared near-field microscopy on layered systems. *Optics Express*, 20(12):13173–13188, 2012.

[129] Javier Aizpurua, Thomas Taubner, F Javier García de Abajo, Markus Brehm, and Rainer Hillenbrand. Substrate-enhanced infrared near-field spectroscopy. *Optics Express*, 16(3):1529–45, February 2008.

[130] Gustav Mie. Beiträge zur optik trüber medien, speziell kolloidaler metalllösungen. *Annalen der Physik*, 25(3):377–455, 1908.

[131] C. F. Bohren and D. R. Huffmann. *Absorption and Scattering of Light by Small Particles*. John Wiley & Sons, Inc., 1st edition, 1983.

[132] Alexander A. Govyadinov, Stefan Mastel, Federico Golmar, Andrey Chuvilin, P. Scott Carney, and Rainer Hillenbrand. Recovery of permittivity and depth from near-field data as a step toward infrared nanotomography. *ACS Nano*, 8(7):6911–6921, 2014.

[133] Andreas J. Huber, Nenad Ocelic, Thomas Taubner, and Rainer Hillenbrand. Nanoscale resolved infrared probing of crystal structure and of plasmon-phonon coupling. *Nano Letters*, 6(4):774–778, 2006.

[134] L. M. Zhang, G. O. Andreev, Z. Fei, a. S. McLeod, G. Dominguez, M. Thiemens, a. H. Castro-Neto, D. N. Basov, and M. M. Fogler. Near-field spectroscopy of silicon dioxide thin films. *Physical Review B*, 85(7):075419, February 2012.

[135] Biao Wang and C. H. Woo. Atomic force microscopy-induced electric field in ferroelectric thin films. *Journal of Applied Physics*, 94(6):4053–4059, Sep 2003.

[136] Bradley Ferguson and Xi-Cheng Zhang. Materials for terahertz science and technology. *Nature Materials*, 1(1):26–33, September 2002.

[137] Masayoshi Tonouchi. Cutting-edge terahertz technology. *Nature Photonics*, 1:97–105, 2007.

[138] Daniel M. Mittleman. Frontiers in terahertz sources and plasmonics. *Nature Photonics*, 7:666–669, 2013.

[139] Jason B. Baxter and Glenn W. Guglietta. Terahertz spectroscopy. *Analytical Chemistry*, 83:4342–4368, 2011.

[140] Ronald Ulbricht, Euan Hendry, Jie Shan, Tony F. Heinz, and Mischa Bonn. Carrier dynamics in semiconductors studied with time-resolved terahertz spectroscopy. *Rev. Mod. Phys.*, 83(2):543–586, Jun 2011.

[141] Tobias Kampfrath, Koichiro Tanaka, and Keith A. Nelson. Resonant and nonresonant control over matter and light by intense terahertz transients. *Nature Photon*, 7(9):680–690, Aug 2013.

[142] Cheryl Feuillet-Palma, Yanko Todorov, Angela Vasanelli, and Carlo Sirtori. Strong near field enhancement in thz nano-antenna arrays. *Scientific Reports*, 3:1361, 2013.

[143] Andrea Toma, Salvatore Tuccio, Mirko Prato, Francesco De Donato, Andrea Perucchi, Paola Di Pietro, Sergio Marras, Carlo Liberale, Remo Proietti Zaccaria, Francesco De Angelis, Liberato Manna, Stefano Lup, Enzo Di Fabrizio, and Luca Razzari. Squeezing terahertz light into nanovolumes: Nanoantenna enhanced terahertz spectroscopy (nets) of semiconductor quantum dots. *Nano Letters*, 15(386-391), 2015.

[144] N. C. J. van der Valk and P. C. M. Planken. Electro-optic detection of subwavelength terahertz spot sizes in the near field of a metal tip. *Applied Physics Letters*, 81(9):1558–1560, 2002.

[145] Stefan A. Maier, Steve R. Andrews, L. Martín-Moreno, and F. J. García-Vidal. Terahertz surface plasmon-polariton propagation and focusing on periodically corrugated metal wires. *Physical Review Letters*, 97(17), Oct 2006.

[146] Victoria Astley, Rajind Mendis, and Daniel M. Mittleman. Characterization of terahertz field confinement at the end of a tapered metal wire waveguide. *Applied Physics Letters*, 95(3):031104, 2009.

[147] S. Hunsche, M. Koch, I. Brener, and M. C. Nuss. Thz near-field imaging. *Optics Communications*, 150:22–26, 1998.

[148] M. A. Seo, H. R. Park, S. M. Koo, D. J. Park, J. H. Kang, O. K. Suwal, S. S. Choi, P. C. M. Planken, G. S. Park, N. K. Park, and et al. Terahertz field enhancement by a metallic nano slit operating beyond the skin-depth limit. *Nature Photonics*, 3(3):152–156, Feb 2009.

[149] Kanglin Wang and Daniel M. Mittleman. Metal wires for terahertz wave guiding. *Nature*, 432:376–379, Nov 2004.

[150] Huawei Liang, Shuangchen Ruan, and Min Zhang. Terahertz surface wave propagation and focusing on conical metal wires. *Optics Express*, 16(22):18241–18248, 2008.

[151] F. Kuschewski, H.-G. von Ribbeck, J. Döring, S. Winnerl, Lukas M. Eng, and S. C. Kehr. Narrow-band near-field nanoscopy in the spectral range from 1.3 to 8.5 thz. *Applied Physics Letters*, 108(113102), 2016.

[152] L. Wimmer, G. Herink, D. R. Solli, S. V. Yalunin, K. E. Echternkamp, and C. Ropers. Terahertz control of nanotip photoemission. *Nature Physics*, 10(6):432–436, May 2014.

[153] H.-G. von Ribbeck, Markus Brehm, D. W. van der Weide, S. Winnerl, O. Drachenko, M. Helm, and Fritz Keilmann. Spectroscopic thz near-field microscopy. *Optics Express*, 16(5):3430–3438, 2008.

[154] Kiwon Moon, Youngwoong Do, Meehyun Lim, Gyuseok Lee, Hyeona Kang, Kee-Su Park, and Haewook Han. Quantitative coherent scattering spectra in aperturelless terahertz pulse near-field microscopes. *Applied Physics Letters*, 101(011109), 2012.

[155] M. Eisele, t. L. Cocker, M. A. Huber, M. Plankl, L. Viti, D. Ercolani, L. Sorba, M. S. Vitiello, and R. Huber. Ultrafast multi-terahertz nano-spectroscopy with sub-cycle temporal resolution. *Nature Photonics*, 8:841–845, 2014.

[156] Tyler L. Cocker, Vedran Jelic, Manisha Gupta, Sean J. Molesky, Jacob A. J. Burgess, Glenda De Los Reyes, Lyubov V. Titova, Ying Y. Tsui, Mark R. Freeman, and Frank A. Hegmann. An ultrafast terahertz scanning tunnelling microscope. *Nature Photonics*, 7(8):620–625, Jul 2013.

[157] Tyler L. Cocker, Dominik Peller, Ping Yu, Jascha Repp, and Rupert Huber. Tracking the ultrafast motion of a single molecule by femtosecond orbital imaging. *Nature*, 539(7628):263–267, Nov 2016.

[158] Vedran Jelic, Krzysztof Iwaszczuk, Peter H. Nguyen, Christopher Rathje, Graham J. Hornig, Haille M. Sharum, James R. Hoffman, Mark R. Freeman, and Frank A. Hegmann. Ultrafast terahertz control of extreme tunnel currents through single atoms on a silicon surface. *Nature Physics*, Feb 2017.

[159] Franz J. Giessibl. High-speed force sensor for force microscopy and profilometry utilizing a quartz tuning fork. *Applied Physics Letters*, 73(26):3956–3958, Dec 1998.

[160] F. Buersgens, G. Acuna, C. H. Lang, S. I. Potrebic, S. Manus, and R. Kersting. Shear force control for a terahertz near field microscope. *Review of Scientific Instruments*, 78(11):113701, Nov 2007.

[161] Xinghan Cai, Andrei B Sushkov, Ryan J Suess, Mohammad M Jadidi, Gregory S Jenkins, Luke O Nyakiti, Rachael L Myers-Ward, Shanshan Li, Jun Yan, D Kurt Gaskill, Thomas E Murphy, H Dennis Drew, and Michael S Fuhrer. Sensitive room-temperature terahertz detection via the photothermoelectric effect in graphene. *Nat Nanotechnol*, 9(10):814–9, Oct 2014.

[162] Andrew Wang and Manish J. Butte. Customized atomic force microscopy probe by focused-ion-beam-assisted tip transfer. *Applied Physics Letters*, 105(5):053101, Aug 2014.

[163] Mark B Lundeberg, Yuanda Gao, Achim Woessner, Cheng Tan, Pablo Alonso-González, Kenji Watanabe, Takashi Taniguchi, James Hone, Rainer Hillenbrand, and Frank H L Koppens. Thermoelectric detection and imaging of propagating graphene plasmons. *Nat Mater*, Sep 2016.

[164] Nathaniel M. Gabor, Justin C. W. Song, Qiong Ma, Nityan L. Nair, Thiti Tychatanapat, Kenji Watanabe, Takashi Taniguchi, Leonid S. Levitov, and Pablo Jarillo-Herrero. Hot carrier-assisted intrinsic photoresponse in graphene. *Science*, 334:648–652, 2011.

[165] Xiaodong Xu, Nathaniel M Gabor, Jonathan S Alden, Arend M van der Zande, and Paul L McEuen. Photo-thermoelectric effect at a graphene interface junction. *Nano Letters*, 10(2):562–6, Feb 2010.

[166] Achim Woessner, Pablo Alonso-González, Mark B Lundeberg, Yuanda Gao, Jose E Barrios-Vargas, Gabriele Navickaite, Qiong Ma, Davide Janner, Kenji Watanabe, Aron W Cummings, Takashi Taniguchi, Valerio Pruneri, Stephan Roche, Pablo Jarillo-Herrero, James Hone, Rainer Hillenbrand, and Frank H L Koppens. Near-field photocurrent nanoscopy

on bare and encapsulated graphene. *Nature Communications*, 7:10783, 2016.

[167] Eduardo J. H. Lee, Kannan Balasubramanian, Ralf Thomas Weitz, Marko Burghard, and Klaus Kern. Contact and edge effects in graphene devices. *Nature Nanotechnology*, 3(8):486–490, Jun 2008.

[168] G. Giovannetti, P. A. Khomyakov, G. Brocks, V. M. Karpan, J. van den Brink, and P. J. Kelly. Doping graphene with metal contacts. *Physical Review Letters*, 101(2), Jul 2008.

[169] Bernhard Knoll and Fritz Keilmann. Enhanced dielectric contrast in scattering-type scanning near-field optical microscopy. *Optics Communications*, 182:321–328, 2000.

[170] M. A. Ordal, Robert J. Bell, R. W. Alexander, L. L. Long, and M. R. Querry. Optical properties of fourteen metals in the infrared and far infrared: Al, co, cu, au, fe, pb, mo, ni, pd, pt, ag, ti, v and w. *Applied Optics*, 24(24):4493–4499, 1985.

[171] L Wang, I Meric, P Y Huang, Q Gao, Y Gao, H Tran, T Taniguchi, K Watanabe, L M Campos, D A Muller, J Guo, P Kim, J Hone, K L Shepard, and C R Dean. One-dimensional electrical contact to a two-dimensional material. *Science*, 342(6158):614–7, Nov 2013.

[172] Achim Woessner, Mark B. Lundeberg, Yuanda Gao, Alessandro Principi, Pablo Alonso-Gonzáles, Matteo Carrega, Kenji Watanabe, Takashi Taniguchi, Giovanni Vignale, Marco Polini, James Hone, Rainer Hillenbrand, and Frank H. L. Koppens. Highly confined low-loss plasmons in graphene-boron nitride heterostructures. *Nature Materials*, 14:421–425, 2014.

[173] Constantine A. Balanis. *Antenna Theory*. John Wiley & Sons, Inc., Hoboken New Jersey, 2005.

[174] Deok-Soo Kim, Hyuksang Kwon, Alexey Yu. Nikitin, Seongjin Ahn, Luis Martin-Moreno, Francisco J. Garcia-Vidal, Sunmin Ryu, Hongki Min, and Zee Hwan Kim. Stacking structures of few-layer graphene revealed by phase-sensitive infrared nanoscopy. *ACS Nano*, 9(7):6965–6773, 2015.

[175] Nader Engheta, Alessandro Salandrino, and Andrea Alù. Circuit elements at optical frequencies: nanoinductors, nanocapacitors, and nanoresistors. *Phys Rev Lett*, 95(9):095504, Aug 2005.

[176] Andrea Alú and Nader Engheta. Tuning the scattering response of optical nanoantennas with nanocircuit loads. *Nature Photonics*, 2:307–310, 2008.

[177] Andrea Alù and Nader Engheta. Input impedance, nanocircuit loading, and radiation tuning of optical nanoantennas. *Phys Rev Lett*, 101(4):043901, Jul 2008.

[178] Felix Benz, Bart de Nijs, Christos Tserkezis, Rohit Chikkaraddy, Daniel O. Sigle, Laurynas Pukenas, Stephen D. Evans, Javier Aizpurua, and Jeremy J. Baumberg. Generalized circuit model for coupled plasmonic systems. *Optics Express*, 23(26):33255, Dec 2015.

[179] B. E. Cole, J. B. Williams, B. T. King, M. S. Sherwin, and C. R. Stanley. Coherent manipulation of semiconductor quantum bits with terahertz radiation. *Nature*, 410:60–63, 2001.

[180] J. R. Danielson, Yun-Shik Lee, J. P. Prineas, J. T. Steiner, M. Kira, and S. W. Koch. Interaction of strong single-cycle terahertz pulses with semiconductor quantum wells. *Physical Review Letters*, 99(23), Dec 2007.

[181] Tobias Kampfrath, Alexander Sell, Gregor Klatt, Alexej Pashkin, Sebastian Mährlein, Thomas Dekorsy, Martin Wolf, Manfred Fiebig, Alfred Leitenstorfer, and Rupert Huber. Coherent terahertz control of antiferromagnetic spin waves. *Nature Photon*, 5(1):31–34, Nov 2010.

[182] O. Schubert, M. Hohenleutner, F. Langer, B. Urbanek, C. Lange, U. Huttner, D. Golde, T. Meier, M. Kira, S. W. Koch, and R. Huber. Sub-cycle control of terahertz high-harmonic generation by dynamical Bloch oscillations. *Nature Photonics*, 8(January):2–6, January 2014.

[183] Joanna M. Atkin, Samuel Berweger, Andrew C. Jones, and Markus B. Raschke. Nano-optical imaging and spectroscopy of order, phases, and domains in complex solids. *Advances in Physics*, 61(6):745–842, 2012.

[184] Kuan-Ting Lin, Susumu Koiyama, and Yusuke Kajihara. Tip size dependence of passive near-field microscopy. *Optics Letters*, 41(3):484–487, 2016.

[185] Glenn D. Boreman. *Modulation Transfer Function in Optical and Electro-Optical Systems*. SPIE - The International Society for Optical Engineering, P.O. Box 10, Bellingham, Washington 98227-0010, USA, 1st edition, 2001.

[186] Charles S. Williams and Orville A. Becklund. *Introduction to the Optical Transfer Function*. SPIE - The International Society for Optical Engineering, 2002, 2002.

[187] Warren J. Smith. *Modern Optical Engineering*. McGraw Hill, 2000.

[188] Paul Dean, Oleg Mitrofanov, James Keeley, Iman Kundu, Lianhe Li, Edmund H. Linfield, and A. Giles Davies. Apertureless near-field terahertz imaging using the self-mixing effect in a quantum cascade laser. *Applied Physics Letters*, 108(9):091113, Feb 2016.

[189] Kiwon Moon, Hongkyu Park, Joenghoi Kim, Youngwoong Do, Soonsung Lee, Gyuseok Lee, Hyeona Kang, and Haewook Han. Subsurface nanoimaging by broadband terahertz pulse near-field microscopy. *Nano Letters*, 15:549–552, 2015.

[190] B. Hecht, H. Bielefeldt, Y. Inouye, D. W. Pohl, and L. Novotny. Facts and artifacts in near-field optical microscopy. *Journal of Applied Physics*, 81(6):2492–2498, Mar 1997.

[191] T. Kalkbrenner, M. Graf, C. Durkan, J. Mlynek, and V. Sandoghdar. High-contrast topography-free sample for near-field optical microscopy. *Applied Physics Letters*, 76(9):1206, 2000.

[192] Viktoriia E. Babicheva, Sampath Gamage, Mark I. Stockman, and Yohannes Abate. Near-field edge fringes at sharp material boundaries. *Optics Express*, 25(20):23935–23944, 2017.

[193] Personal Communicaion.

[194] Roman Krutokhvostov, Alexander A. Govyadinov, Johannes M. Stiegler, Florian Huth, Andrey Chuvilin, P. Scott Carney, and Rainer Hillenbrand. Enhanced resolution in subsurface near-field optical microscopy. *Optics Express*, 20(1):593–600, 2012.

[195] J. Bijeon, P. Adam, D. Barchiesi, and P. Royer. Definition of a simple resolution criterion in an Apertureless Scanning Near-Field Optical Microscope (A-SNOM): contribution of the tip vibration and lock-in detection. *The European Physical Journal Applied Physics*, 52:45–52, 2004.

[196] R. Esteban, Ralf Vogelgesang, and Klaus Kern. Full simulation of the apertureless scanning near field optical microscopy signal: achievable resolution and contrast. *Optics Express*, 17(4):2518–2529, 2009.

[197] Thomas Taubner, F Keilmann, and R Hillenbrand. Nanoscale-resolved subsurface imaging by scattering-type near-field optical microscopy. *Optics Express*, 13(22):8893–9, October 2005.

[198] Edward D. Palik, editor. *Handbook of optical constants of solids II.* Academic Press, 2001.

[199] John David Jackson. *Classical Electrodynamic.* John Wiley & Sons, Inc., 3rd edition, Hoboken, NJ, USA 1999.

[200] I. Rajapaksa, K. Uenal, and H. Kumar Wickramasinghe. Image force microscopy of molecular resonance: A microscope principle. *Applied Physics Letters*, 97(7):073121, Aug 2010.

[201] Markus Brehm, Thomas Taubner, Rainer Hillenbrand, and Fritz Keilmann. Infrared spectroscopic mapping of single nanoparticles and viruses at nanosclae resolution. *Nano Letters*, 6(7):1307–1310, 2006.

[202] Xiaoji G. Xu, Mathias Rang, Ian M. Craig, and Markus B. Raschke. Pushing the sample-size limit of infrared vibrational nanospectroscopy: From monolayer toward single molecule sinsitivity. *The Journal of Physical Chemistry Letters*, 3:1836–1841, 2012.

[203] Benjamin Pollard, Eric A. Muller, Karsten Hinrichs, and Markus B. Raschke. Vibrational nano-spectroscopic imaging correlating structure

with intermolecular coupling and dynamics. *Nature Communications*, 5:3587, 2014.

[204] Kerstin Mueller, Xiujuan Yang, Melissa Paulite, Zahra Fakhraai, Nikhil Gunari, and Gilbert C. Walker. Chemical imaging of the surface of self-assembled polystyrene-b-poly(methyl methacrylate) diblock copolymer films using apertureless near-field ir microscopy. *Langmuir*, 24:6946–6951, 2008.

[205] Christian Westermeier, Adrian Cernescu, Sergiu Amarie, Clemens Liewald, Fritz Keilmann, and Bert Nickel. Sub-micron phase coexistence in small-molecule organic thin films revealed by infrared nano-imaging. *Nature Communications*, 5:4101, 2014.

[206] A. Cvitkovic, N. Ocelic, J. Aizpurua, R. Guckenberger, and R. Hillenbrand. Infrared Imaging of Single Nanoparticles via Strong Field Enhancement in a Scanning Nanogap. *Physical Review Letters*, 97(6):060801, August 2006.

[207] Nicolas Behr and Markus B. Raschke. Optical antenna properties of scanning probe tips: Plasmonic light scattering, tip-sample coupling, and near-field enhancement. *Journal of Physical Chemistry C*, 112:3766–3773, 2008.

[208] Arnulf Röseler. *Infrared Spectroscopic Ellipsometry*. Akademie Verlag, Berlin, 1990.

[209] Moritz Esslinger and Ralf Vogelgesang. Reciprocity theory of apertureless scanning near-field optical microscopy with point-dipole probes. *ACS Nano*, 6(9):8173–82, September 2012.

C List of Publications

This thesis is based on the following publications:

1. Stefan Mastel, Alexander A. Govyadinov, Curdin Maissen, Andrey Chuvilin, Andreas Berger, and Rainer Hillenbrand. Understanding the image contrast of material boundaries in IR nanoscopy reaching 5 nm spatial resolution. *ACS Photonics* 5 (8), 3372-3378 (2018)

2. Stefan Mastel, Mark B. Lundeberg, Pablo Alonso-Gonzlez, Yuanda Gao, Kenji Watanabe, Takashi Taniguchi, James Hone, Frank H. L. Koppens , Alexey Y. Nikitin, and Rainer Hillenbrand. Terahertz Nanofocusing with Cantilevered Terahertz-Resonant Antenna Tips. *Nano Letters* 17(11): 6526-6533

3. Stefan Mastel, Alexander A. Govyadinov, Thales V. A. G. de Oliveira, Iban Amenabar, and Rainer Hillenbrand. Nanoscale-resolved chemical identification of thin organic films using infrared near-field spectroscopy and standard Fourier transform infrared references. *Applied Physics Letters* 106, 023113 (2015)

Other publications:

1. Maria C. Giordano, Stefan Mastel, Clemens Liewald, Lorenzo L. Columbo, Massimo Brambilla, Leonardo Viti, Antonio Politano, Kai Zhang, Lianhe Li, A Giles Davies, Edmund H. Linfield, Rainer Hillenbrand, Fritz Keilmann, Gaetano Scamarcio, and Miriam S. Vitiello. Phase-resolved terahertz self-detection near-field microscopy. *Optics Express* 21 (14), 18423-18435 (2018)

2. Peter Schmidt, Fabien Vialla, Simone Latini, Mathieu Massicotte, Klaas-Jan Tielrooij, Stefan Mastel, Gabriele Navickaite, Mark Danovich, David A. Ruiz-Tijerina, Celal Yelgel, Vladimir Falko, Kristian Thygesen, Rainer Hillenbrand, and Frank H. L. Koppens. Nano-imaging of intersubband transitions in van der Waals quantum wells. *Nature Nanotechnology* accepted (2018)

3. Patryk Kusch, Nieves Morquillas Azpiazu, Niclas Sven Mueller, Stefan Mastel, Jose Ignacio Pascual, and Rainer Hillenbrand. Combined Tip-Enhanced Raman Spectroscopy and Scattering-Type Scanning Near-Field Optical Microscopy. *The Journal of Physical Chemistry C* 122, 16274-16280 (2018)

4. Miren Etxeberria-Benavides, Oana David, Timothy Johnson, Magdalena M Lozinska, Angelica Orsi, Paul A Wright, Stefan Mastel, Rainer Hillenbrand, Freek Kapteijn, and Jorge Gascon. High performance mixed matrix membranes (MMMs) composed of ZIF-94 filler and 6FDA-DAM polymer. *Journal of Membrane Science* 550, 198-207 (2018)

5. Clemens Liewald, Stefan Mastel, Jeffrey L. Hesler, Andreas J. Huber, Rainer Hillenbrand, and Fritz Keilmann. All-electronic terahertz nanoscopy. *Optica* 5(2): 159-163

6. Francisco J. Alfaro-Mozaz, Pablo Alonso-González, Saul Vélez, Irene Dolado, Marta Autore, Stefan Mastel, Felix Casanova, Louis E. Hueso, Peining Li, Alexey Y. Nikitin, and Rainer Hillenbrand. Nanoimaging of resonating hyperbolic polaritons in linear boron nitride antennas. *Nature Communications* 8, 15624 (2017)

7. Patryk Kusch, Stefan Mastel, Niclas S. Mueller, Nieves Morquillas Azpiazu, Sebastian Heeg, Roman Gorbachev, Fredrik Schedin, Uwe Hübner, Jose I. Pascual, Stephanie Reich, and Rainer Hillenbrand. Dual-Scattering Near-Field Microscope for Correlative Nanoimaging of SERS and Electromagnetic Hotspots. *Nano Letters* 17(4), 2667-2673 (2017)

8. Lorena Ugarte, Arantzazu Santamaria-Echart, Stefan Mastel, Marta Autore, Rainer Hillenbrand, Maria Angeles Corcuera, and Arantxa Eceiza. An alternative approach for the incorporation of cellulose nanocrystals

in flexible polyurethane foams based on renewably sourced polyols. *Industrial Crops and Products* 95, 564-573 (2017)

9. Alexey Y. Nikitin, Pablo Alonso-González, Saul Vélez, Stefan Mastel, Alba Centeno, Amaia Pesquera, Amaia Zurutuza, Felix Casanova, Louis E. Hueso, Frank H. L. Koppens, and Rainer Hillenbrand, Real-space mapping of tailored sheet and edge plasmons in graphene nanoresonators, *Nature Photonics* 10, 239-243 (2016)

10. Edward Yoxall, Martin Schnell, Stefan Mastel, and Rainer Hillenbrand. Magnitude and phase-resolved infrared vibrational nanospectroscopy with a swept quantum cascade laser. *Optics Express* 23(10), 13358-13369 (2015)

11. Robin Hegenbarth, Andreas Steinmann, Stefan Mastel, Sergiu Amarie, Andreas J. Huber, Rainer Hillenbrand, S. Y. Sarkisov, and Harald Giessen. High-power femtosecond mid-IR sources for s-SNOM applications. *Journal of Optics* 16, 094003 (2014)

12. Alexander A. Govyadinov, Stefan Mastel, Federico Golmar, Andrey L. Chuvilin, P. Scott Carney, and Rainer Hillenbrand. Recovery of Permittivity and Depth from Near-Field Data as a Step Toward Infrared Nanotomography. *ACS Nano* 8, 6911 (2014)

13. Sarah E. Grefe, Daan Leiva, Stefan Mastel, Scott D. Dhuey, Stefano Cabrini, P. James Schuck, and Yohannes Abate. Near- field spatial mapping of strongly interacting multiple plasmonic infrared antennas, *Physical Chemistry Chemical Physics* 15, 18944-18950 (2013)

14. Stefan Mastel, Sarah E. Grefe, G. B. Cross, A. Taber, Scott D. Dhuey, Stefano Cabrini, P. James Schuck, and Yohannes Abate. Real-Space Mapping of Nanoplasmonic Hotspots via Optical antenna-Gap Loading. *Applied Physics Letters* 101, 131102 (2012)

D Acknowledgements

I want to express my gratitude to my supervisor Prof. Rainer Hillenbrand, group leader of the nano-optics group at CIC nanoGUNE, for giving me the opportunity to join his group, for being involved in so much detail in my conducted projects and for being a transparent person and supervisor.

I would like to gratefully acknowledge all present and past members of the nano-optics group at CIC nanoGUNE, for fruitful discussions, experimental and theoretical support, and the great atmosphere in the group. In particular I would like to thank Dr. Alexander A. Govyadinov, who was my teacher and shared with me his deep understanding of the theory of nano-optics. Further, I acknowledge Dr. Martin Schnell for help with Synthetic Optical Holography (SOH) and discussions about RF antenna theory, and Dr. Alexey Yu. Nikitin and F. Javier Alfaro for help with numerical simulations using Comsol. Further, I would like to thank Dr. Monika Goikoetxea (CIC nanoGUNE) for her continuous support and help in administering the research projects and the PhD thesis.

I would like to thank Dr. Christopher Tollan and Dr. Andrey Chuvilin (both CIC nanoGUNE) for their continuos help in the SEM and FIB lab, helping developing concepts to manufacture sharp metal tips, the preparation of the lamella cross section and recording the STEM image shown in chapter 5.

Many thanks to Itziar Otegui (CIC nanoGUNE) and Yurdana Castelruiz (CIC nanoGUNE) for providing support with the financial administration of the research projects, and the formal administration of the PhD thesis.

I thank all employees of neaspec GmbH for their continuous support throughout the time of my PhD thesis.

I would like to thank Thales V. A. G. de Oliveira (CIC nanoGUNE) for the preparation of thin film PMMA samples, and Roman Krutohvostovs (CIC nanoGUNE, Spain) for recording the far-field FTIR spectra of PMMA presented in chapter 6 (*Nanoscale chemical identification of thin films using infrared near-field spectroscopy and standard Fourier transform infrared refer-*

ences).

I am acknowledging Dr. Andreas Berger (CIC nanoGUNE) for fruitful discussions of the results presented in chapter 5, Prof. P. Scott Carney (Institute of Optics, University of Rochester, USA) for his input in interpreting the results shown in chapter 6, and Prof. Nader Engheta (University of Pennsylvania, USA) for discussions about RF antenna theory.

Thanks to Dr. Yuanda Gao (Columbia University, USA), Dr. Kenji Watanabe (National Institute for Material Science, Japan), Prof. Takashi Taniguchi (National Institute for Material Science, Japan), and Prof. James Hone (Columbia University, USA) for the fabrication of the graphene device used in chapter 4, and to Prof. Frank Koppens and Dr. Mark Lundeberg (both ICFO, Castelldefels) for experimental support using the graphene device.

My special thanks goes to my family for their encouragement, continuous support, and teaching me all the values beyond science.